UNIVERSITE   DE   LIMOGES

ECOLE   DOCTORALE n° 521-Science et Ingénierie pour l'Information
Faculté des Science et Techniques
Institut de Recherche Xlim-département Photonique

T H E S E

Pour obtenir le titre de
Docteur de l'Université de Limoges

Discipline: Electronique des Hautes Fréquences, Photonique et Systèmes

Présentée et soutenue par
Huijia Zhang
Le 20 decembre 2012

Utilization of powder method for the realization of

special optical fibers

Thèse dirigée par Jean-Louis AUGUSTE et Georges HUMBERT

Jury:

Rapporteurs:	Valério ROMANO	Professeur, Université de Berne, Berne
	Adelrafik MALKI	Maître de Conférences (HDR), Université de Rouen
Examinateurs:	Gérard MONNOM	Directeur de Recherche CNRS, Université de Nice
	Dominique CROS	Professeur, XLIM, Limoges
Directeurs:	Jean-Louis AUGUSTE	Ingénieur de recherche (HDR), XLIM, Limoges
	Georges HUMBERT	Chargé de Recherche CNRS, XLIM, Limoges

Acknowledgement

General   introduction

In the sixties, Charles K. Kao and Georges A. Hockham, in the British Standard Telephones and Cables (STC) company, proposed that by applying high purity silica glass as the material of optical fiber, the attenuation in optical fibers could be reduced below 20 decibels per kilometer (dB/km) for a practical communication application. Since that time, the technology of optical fiber makes a large progress and the optical fiber communication have been widely applicated in everyday life. Internet technology, based on optical fiber communication with high transmission speed, changes the life style of people, life of people comes into information times.

Different with the conventional silica glass fiber (fabricated by CVD Techniques or Stack and Draw) and soft glass fiber (typically Tellurite or Chalcogenide fibers), recently, one new fiber family is born, called *multimaterial optical fiber* (the composition of the core and cladding is made of different materials) attracting more and more attention of the researchers in many countries. These multimaterial special optical fibers present very high refractive index difference and nonlinear coefficient. The material concept of multimaterial fibers is not only in the case of dedicated glasses, but also can be extended to nanoparticles and metallic wires inside silica matrix. Compared with the pure silica, the used material in multimaterial special optical fiber often has larger material loss in the conventional (0.2-3 μm) wavelength region, so its attenuation are often larger than the conventional silica glass fiber obtained by CVD processes in the conventional (0.2-3 μm) wavelength region. But some materials have low transmission loss (around some hundreds of dB/km) in unconventional (beyond the region of 0.2-3 μm: ultraviolet and middle infrared region) wavelength region (in these wavelength region, silica glass has high attenuation), so these special materials could be used to realize special optical fibers with smart behavior in ultraviolet and middle infrared transmission range. Moreover, semiconductor core fiber and metal fiber also have been fabricated and studied for high nonlinear and sensing application, respectively.

The conventional method for doping a fiber is chemical vapor deposition (CVD). Recently, in order to overcome the doping volume and concentration limit of CVD method, powder doping method becomes popular to fabricate highly doped optical fiber. Among three kinds of powder doping methods (Melt-Quenching method, Repusil technique and powder-in-tube method), powder-in-tube method is the most convenient and the least contaminating. So in this thesis, we apply the powder-in-tube method to fabricate highly doped heavy metal oxide silica glass fiber and metal fiber. In chapter 1, we introduce all kinds of fabrication methods for doping optical fiber, and we also analyze their advantage and drawbacks, we justify the choice of the powder-in-tube method and focus on its great potential to fabricate multimaterial optical fibers. In chapter 2, the solid core Arrow bandgap fiber with high index difference ($\approx$0.1) was designed and analyzed. Owing to its low bend loss and better confinement - to keep single mode transmission – this fiber can be developed for high power laser transmission. We fabricated and represented one optical fiber with a highly doped heavy metal oxide (SAL fiber: 70mol%SiO_2, 20mol%Al_2O_3, and 10mol% La_2O_3). The interest of this glass is its high refractive index leading to a difference with the cladding of 0.1. The SAL fiber is fabricated by powder-in-tube method described in chapter 1. Based on the SAL fiber and one cane of silica glass photonic crystal fiber, we designed and fabricated one low loss solid core Arrow bandgap fiber (by simulation prediction, attenuation is as low as 10^{-7} dB/m in the case of 5 layers rod and a pitch of 7 μm.) In chapter 3, we first analyzed the principle of fabricating a continuous copper rod by powder-in-tube method, and during melting copper powder to fabricate copper rod, we need to select the glass tube with enough thick inner diameter to overcome region accumulation effect of liquid copper. Then we analyzed the principle of drawing the continuous copper fiber, and proposed the two improved drawing methods (increasing pressure method and slow speed drawing method) to get a continuous long copper fiber. At the same time, we also introduced our experiment progress of some copper rod fabrication and copper fiber fabrication. Finally, we designed one improved structure microsize coaxial cable for lower loss at 100GHz. We will apply the technology of our fabricating copper fiber to fabricate the

improved structure microsize coaxial cable.

Chapter I . Fabrication methods of conventional optical fiber and multi-glass fiber……………………………………1

Chapter I. Fabrication methods of conventional optical fiber and multi-glass fiber

I.1 Introduction of optical fiber and its main families

Total internal reflection theory [1] had been known since the 19th century. It is the basic theory for light guidance in the optical fiber. In 1966, Charles K. Kao and Georges A. Hockham of the British Standard Telephones and Cables (STC) company were the first to propose that the attenuation in optical fibers could be reduced below 20 decibels per kilometer (dB/km). This will make of the fibers a practical communication medium [2]. They explained that the attenuation, in optical fibers at that time, was caused by impurities that could be removed, rather than by fundamental physical effect such as scattering. They correctly and systematically theorized the light-loss properties for optical fiber, and pointed out the right materials to use for such fiber-silica glass with high purity. Charles K. Kao awarded the Nobel Prize in Physics in 2009 for these achievements. The crucial attenuation limit of 20 dB/km was first achieved in 1970 by Corning Glass Company [3]. With further progress in fiber fabrication technology [4], a low loss of only 0.2 dB/km at the wavelength 1.55 μm was realized in 1979 [5]. The loss level is limited mainly by Rayleigh scattering. The availability of low-loss silica fibers led to a revolution in the field of optical fiber communications.

I.1.1 Conventional optical fibers

The conventional optical fibers can be classified into: step-index optical fibers and graded index optical fibers. The simplest step-index optical fiber structure consists of a central glass core surrounded by cladding layer whose refractive index n_2 is slightly lower than the core one n_1. Graded index optical fiber is similar in structure to step-index optical fiber, but refractive index at different positions in the core region gradually increases when distance decreases from the center of the core. Figure 1.1

shows schematically the cross section (a) and refractive-index profile (b) and (c) of a step-index fiber and graded index fiber, respectively.
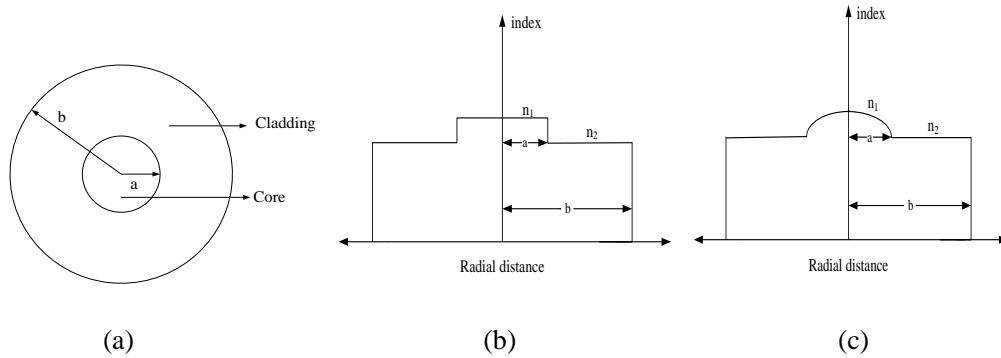
Figure 1.1: Schematic illustration of the cross section (a), the refractive-index profile of a step-index fiber (b), of graded index fiber (c).

I.1.2 Microstructured optical fibers

More recently, new kind of light guidance mechanism: photonic bandgap guidance is demonstrated in photonic crystal fibers (PCFs) [6]. The later can be simply classified into two types: (1) index-guidance photonic crystal fibers and (2) hollow core bandgap guidance photonic crystal fibers. Their cross section structures are illustrated in figure 1.2.
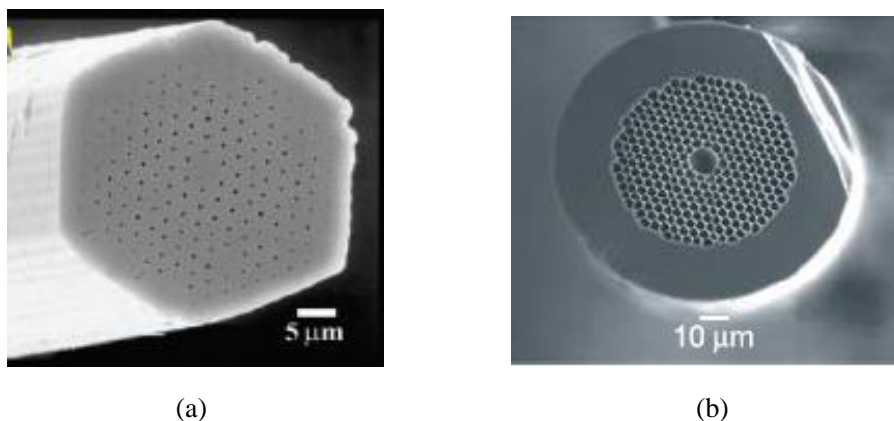
Figure 1.2: Scanning Electronic microscope images of cross section of typical (a) index-guidance and (b) hollow core bandgap guidance photonic crystal fibers. Courtesy University of Bath.

The typical fabrication method of the preform of photonic crystal fibers is the

stack-and-draw method. The later consists of stacking tightly many pieces of thin silica capillaries, and then the central capillary is replaced by a silica rod to form an index-guidance solid-core photonic crystal fiber. The hollow-core of photonic bandgap fiber is obtained by removing one or several capillaries in the center of the stack. This stack is then inserted into a large jacketing silica tube, and it is drawn into canes with an external diameter of few millimeters. Finally, the cane is inserted into a silica tube and drawn down into an optical fiber. Figure 1.3 illustrates this process for the preform fabrication of photonic crystal fibers.
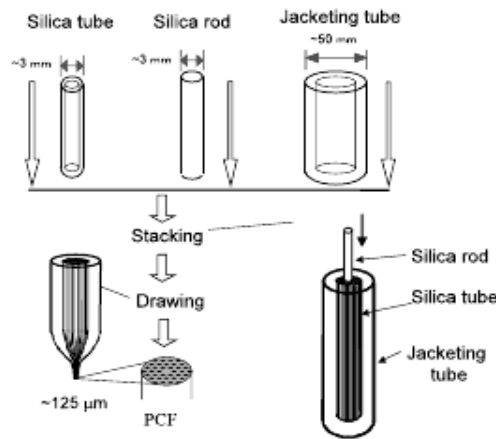
Figure 1.3: Stack-and-draw method for the preform fabrication of photonic crystal fibers [7].

I.1.3 Soft Glass Fibers

Another important family of optical fibers is the soft glass (comparing with silica glass, the softening temperature of these kinds of glass is relatively lower.) fibers. Tellurite and Chalcogenide glass optical fibers are two representatives of these fibers [8, 9]. The main advantage of these materials is their wider transmission range in the mid-infrared domain: from 0.5 μm to 10 μm for Tellurite glass and from 0.4 μm to 6 μm for chalcogenide glass [10], while the silica glass ranges from 0.2 μm to 3 μm. The stack and draw technique is also used to realize soft glass photonic crystal fiber [10-12]. In order to avoid mistakes, in this report, when we discuss about glass fiber, we mean a glass based on silica, but the glass based on silica includes other metal oxidation dopants.

I. 2 Multicomponent glass optical fiber

In this thesis, multicomponent glass means that silica (SiO_2) represents an amount of 75 mol% of the whole glass, and other components are contained in this glass. In chapter 3 we will give also some results with metallic wires included in optical fibers.

Multicomponent glasses offer various properties that are interesting to fabricate original optical fibers, such as larger refractive index and different thermo-optic properties than silica.

Another salient property is the larger nonlinear refractive index than silica one. Indeed, nonlinear effects in silica optical fiber are limited by the low nonlinear refractive index of silica ($n_2 = 2.6 \times 10^{-20}$ m^2/W). So some optical glasses which have high nonlinear refractive index coefficient are investigated to fabricate high nonlinear optical fiber. Nonlinear coefficient of optical fiber is defined as follows [13]:

$$\gamma = \frac{n_2 \omega}{c A_{eff}}$$

n_2 is the nonlinear refractive index of the material. ω is the angular frequency of light, c is the light speed in the free space. A_{eff} is effective mode area of the considered guided mode and is defined as follows:

$$A_{eff} = \frac{(\int\int_{-\infty}^{\infty} |F(x,y)|^2 \, dxdy)^2}{\int\int_{-\infty}^{\infty} |F(x,y)|^4 \, dxdy}$$

With F(x,y) the mode distribution function.

Now if we are looking for optical glasses which have high nonlinear refractive index we can propose:

- Lead silicate glasses SF6 $n_{2(SF6)} = 2.2 \times 10^{-19} m^2$/w $\approx 10 \times n_{2(SiO2)}$ [14] (glass produced by Schott);

- Lead silicate glasses SF57 $n_{2(SF57)} = 4.1 \times 10^{-19} m^2$/w $\approx 20 \times n_{2(SiO2)}$ [15] (glass produced by Schott);

- Tellurite glass $n_{2(tellurite)}=2.5\times10^{-19}m^2/w\approx10\times n_{2(SiO2)}$ [8];

- Chalcogenide glass $n_{2(chalcogenide)}=2\times10^{-18}m^2/w\approx100\times n_{2(SiO2)}$[16];

- Bismuth silicate glass $n_{2(bismuth\ silicate)}=3.2\times10^{-19}m^2/w\approx12\times n_{2(SiO2)}$[17];

- Bismuth borate glass $n_{2(bismuth\ borate)}=1.1\times10^{-18}m^2/w\approx50\times n_{2(SiO2)}$ [17,18].

Unfortunately, the application of these special glasses for high nonlinear fiber, is limited by their high optical losses [14], and to the difficulty to splice these fibers to standard silica fibers. One proposed tradeoff is to use highly doped silica fiber (≥30 mol%) with glass that exhibits a large nonlinear refractive index. Namely the fiber core materials is highly doped silica glass, and the cladding is pure silica (due the name of multicomponent glass optical fiber). One interest is to obtain a step index multicomponent fiber with nonlinear performances equivalent to pure PCF but with lower fabrication constraints.

But one challenge is the fabrication of this kind of highly doped silica, because of the strong discrepancies in material properties between core and cladding material, such as transition temperature (T_g) and expansion coefficient (α).

I.3 Introduction to fabrication methods of doped silica fibers

Silica glass synthesized by fusing SiO_2 molecules is the used material to fabricate low loss optical fibers. Through selecting different dopants during the fabrication process, one can realize the desired refractive-index difference between the core and the cladding. Dopants such as GeO_2 and P_2O_5 can increase the refractive index of pure silica and are suitable for the core. While materials such as B (boron) and F (fluorine) can decrease the refractive index of silica, so they are used for the cladding. Other dopants can also be used for specific applications. For example, to make fiber amplifiers and lasers, the core of silica fibers is codoped with rare-earth ions, such as Erbium (Er), Ytterbium (Yb) …

The fabrication of optical fibers involves two steps [13, 19]. The first step is the fabrication of the preform. The later is a large glass body (typically 20 to 125 mm in

diameter and 1 to 2 m in length), which is fabricated with appropriate core/clad geometry. In the second step, the preform is drawn into a fiber using a precision-feed mechanism that feeds it into a furnace at a proper speed [20] and temperature. During this process, the relative core-cladding ratio is preserved.

In the following sections, I will present different fabrication methods of preforms.

I. 3.1 Fabrication methods of silica preforms with low dopant concentrations

Several methods can be used to fabricate the doped preform. The four commercially used methods are Modified Chemical Vapor Deposition (MCVD) [21], Outside Vapor Deposition (OVD) [22], Vapor-phase Axial Deposition (VAD) [23], and Plasma Chemical Vapor Deposition (PCVD) [24].

These methods are based on the vapor deposition process. Highly pure silica glass is produced from liquid $SiCl_4$ and liquid halide that are boiled, then vaporized and deposited into substrate. Doping elements could be added in the silica glass by the same process. This process enables the fabrication of extremely pure glasses since it is based on pure liquids.

I.3.1.1 Modified chemical vapor deposition (MCVD) method

The MCVD process was first reported by MacChesney et al [25, 26] in 1974. This method consists in depositing inner cladding and core layer glasses in the silica cladding tube. The whole system is in highly-pure and completely close atmosphere. So the purity of preform will be very high by this fabrication method. This method can produce high quality single mode and multimode fibers. Figure 1.4 shows a schematic diagram of the MCVD process. Through mixing the vapors of $SiCl_4$ and O_2 at a temperature of 1800 $^{\circ}$C, successive layers of SiO_2 are deposited inside of silica tube. In this process, the multiburner torch is moved back and forth across the whole tube length for increasing the thickness of the deposit. The refractive index of the cladding layers is adjusted through adding fluorine to the tube. After a sufficient cladding thickness has been deposited with multiple passes of the torch, the vapors of

dopants ($GeCl_4$ or $PoCl_3$) are added to the vapor mixture to form the fiber core. When all layers have been deposited, the torch temperature is raised to collapse the tube into a solid rod which is called the preform of the fiber.
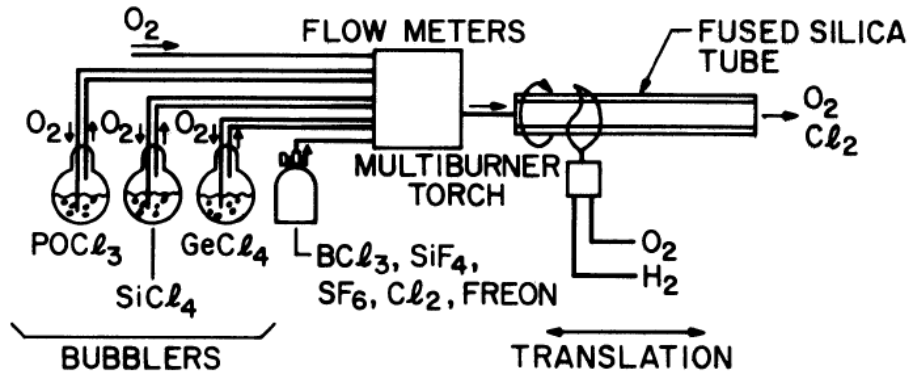
Figure.1.4: Schematic diagram of the MCVD process commonly used for fiber fabrication [21]

The advantages of MCVD method are: (1) Reaction takes place in the tube. Impurity is not easy to be interfused, so low loss fiber is easy to get. (2) The distribution of the refractive index is easy to be controlled exactly. (3) Vapor pressure of reagent is large. The disadvantages of this method are: (1) Slow deposition speed (2) If dopants is too much in the deposition process, it will result in the inconsistent expansion coefficient. During the contraction to obtain the preform, the glass becomes fragile. (3) And $GeCl_4$ is easy to sublime. This induces a depressed zone of refractive index to be formed.

I.3.1.2 Outside vapor deposition (OVD) method

The chemistry basis of the OVD process was given by the work of Hyde [27], who made vitrified silica by passing vapors of a hydrolysable silicon compound, such as silicon tetrachloride, through a gas-oxy burner flame. And then Keck and Schultz did a breakthrough progress, by applying the vapor deposition of silica [28].

The mechanism of OVD method is hydrolyzation by flame. Namely, glass component is deposited by powder ash which is produced through OH or CH_4 flame hydrolyzing halide.

The process of preform is divided into two steps: deposition and sintering.

I.3.1.2.1 Deposition

Deposition process is shown in Figure 1.5(a). In the OVD technology, hydroxyl flame is fixed, and target rod circumrotates itself and reciprocates along longitudinal direction at the same time. Then highly pure raw materials compound ($SiCl_4$, $GeCl_4$ et.al) is sprayed to the target rod, oxide glass powder ash produced by hydrolyzation is deposited on the target rod under high temperature. Target rod moves along longitudinal direction, so porous glass is deposited layer by layer on the rod. The distribution of refractive index is controlled by changing the species and amount of dopants.
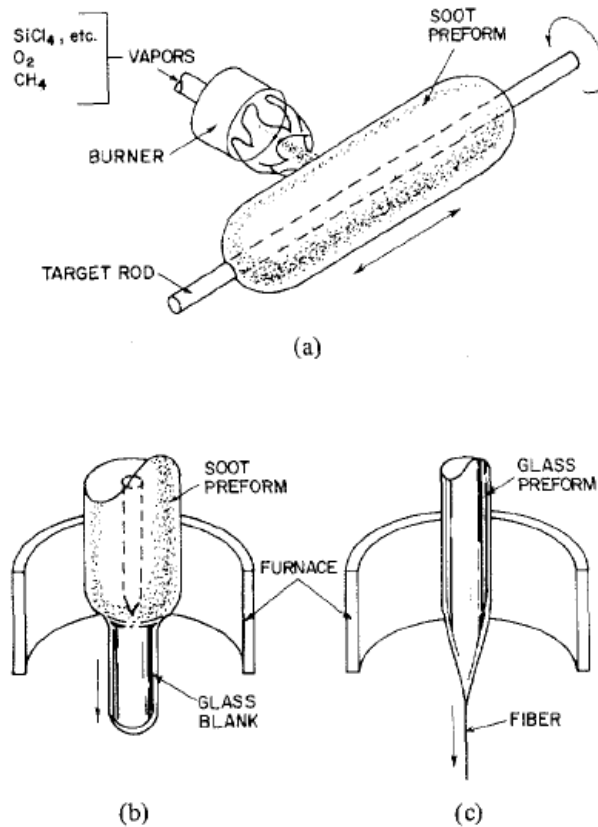
Figure 1.5 Outside vapor deposition process [22]. (a) Soot deposition. (b) Sintering. (c) Fiber drawing.

I.3.1.2.2 Sintering

Sintering of the porous soot preform to a dense glass preform [shown in Fig1.3 (b)] is done by supporting the soot preform. During sintering, dry gas (Cl_2, O_2, N_2, $SoCl_2$) is filled to blow porous preform and remove leftover water. Finally, Drawing of glass

preforms into fiber (shown in Fig1.3(c)) is done by using induction or resistance furnaces at about 2000 $^\circ$C.

The advantages of OVD method are: (1) high production efficiency: deposition speed is 10 times higher than MCVD method. (2) The size of fiber preform is not restricted by mother tube. Large size preform (weight: 2~3 kg) is possible to be fabricated. (3) All preform materials are produced by deposition technology, so OH^{-1} content may be very low (lower than 0.01 ppm). (4) Massive production is possible due to low production cost. The disadvantages of this method are: when the target rod is removed, the refractive index distribution of the middle layer of preform is affected, and this will result in debasing the transmission performance of fiber.

I.3.1.3 Introduction of vapor-phase axial deposition (VAD) method

The vapor-phase axial deposition technique (VAD) was developed at Ibaraki Electrical Communication Laboratory of NTT, and reported at the First IOOC Conference held in Tokyo in 1977 [29]. The mechanism of VAD method is also hydrolyzation by flame to make oxide glass. This is the same with OVD method.

A typical apparatus for the VAD preform fabrication is shown in figure.1.6 [23]. The fabrication process of the preform is also divided into two steps: deposition and sintering.

I.3.1.3.1 Deposition process

Firstly, the target rod is put vertically on the clamp of reaction furnace, and the target rod's end part which receives depositions is revolved. Glass halide saturated vapor is taken to burner inlet by loaded oxygen (O_2) and hydrogen (H_2), argon (Ar). By hydrolyzation at high temperature flame, glass oxide powder ashes (SiO_2-GeO_2 and SiO_2) are produced, and are deposited on inner and outer surface of targeted rod which is revolved and elevated at the same time. Deposition layers in the bottom of target rod are gradually formed. Rotary targeted rod should continuously elevate to make deposition side keep the same position. Finally, porous preform is formed by deposition

I.3.1.3.2 Sintering

After deposition, porous preform is elevated to reaction furnace. Cl_2, H_2 and $SoCl_2$ are filled to dehydrate and sintered to form transparent glass fiber preform.

Considering the mass production and economical points of view, the VAD process had the possibility of continuous fabrication of high silica fiber preforms and the deposition speed was extremely fast compared to that of the MCVD process.
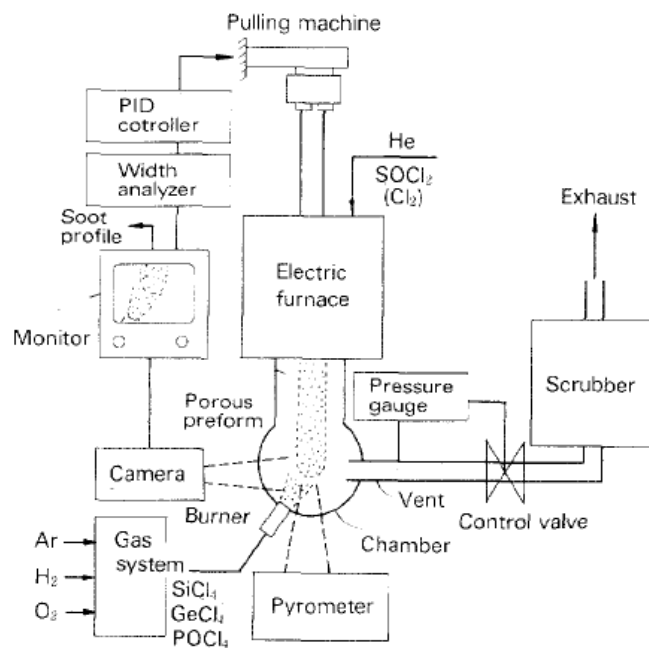
Figure1.6: Schematic diagram of VAD apparatus [23]

I.3.1.4 Introduction of plasmas chemical vapor deposition (PCVD)

Plasmas chemical vapor deposition (PCVD) was invented by Phillips Company in 1976 [30]. The technology is similar to MCVD method. They both apply vapor deposition technology and oxidation reaction. The difference lies in the reaction mechanism. In the later in PCVD method, OH flame heating source in the MCVD is replaced by microwave cavity heating source.

A microwave source of several hundreds or thousands of watts is injected into a microwave resonant cavity that stimulates low pressure gas to generate plasma. The plasma formed in the silica cladding tube is far from thermo-balance state. The released heat is enough to melt the vaporized low melting point and boiling point

reaction materials $SiCl_4$ and $GeCl_4$ to form vapor deposition layers.

The advantages of PCVD method are:

(1) Owing to microwave cavity heating, deposition temperature is lower than heat reaction temperature, silica cladding is not easy to distort.

(2) Good control performance, because gas ionization is not restricted by thermal capacity of the cladding tube, so microwave heating cavity may quickly move back and forth along silica cladding tube. The thickness of deposited layer may be thinner than 1μm, and thereby it is possible to deposit more than one thousand layers in core region that is close to ideal distribution of refractive index.

(3) The repeatability of the geometry and optical characters is adapted to mass production. High deposition efficiency: The deposition efficiency for $SiCl_4$ is close to 100%. High deposition speed is favorable to reduce production cost.

In the following table are resumed the main properties of these methods for fabricating silica doped preforms:

Method / Property	MCVD	OVD	VAD	PCVD
Mechanism	High T oxidation	Flame hydrolyzation	Flame hydrolyzation	Low T oxidation
Heat source	OH flame	CH_4 or OH flame	OH flame	plasmas
Deposition direction	Inner surface of tube	Outer radial direction of targer rod	Axial direction of targer rod	Inner surface of tube
Deposition speed	middle	high	high	low
Deposition technology	fitful	fitful	continuous	fitful
Preform size	small	large	large	small
Control of refractive index distribution	easy	easy	Single mode: Easy Multimode: hard	Very easy
Purity request	strict	Not strict	Not strict	strict

Table1.1: Comparison of several kinds of vapor deposition methods

I.3.2 Introduction of methods for fabricating highly doped silica fibers

Theses fabrication methods, based on VAP process, are not suitable for fabricating highly doped silica fibers. The dopants concentration is usually limited to few percent/mol [32-33]. Above this range of concentration, cracks appear in the prefrom when the heating source is turned off. In order to fabricate multicomponent glass optical fibers, researches have been focused on alternative methods, some of which are presented in the following sections.

I.3.2.1 The Sol-Gel method

The sol-gel method [34] was developed in the 1960s. It was predicted that after the technology of Sol-Gel method is mature, the production cost will be very low. So since that time, from economic or scientific point of view, the Sol-Gel method attracted large interest of people. But the attenuation of core layer glass produced by this method is still relative large, so the Sol-Gel method is still far to be widely used in industry.

Generally speaking, the Sol-Gel method changes the wafer material surface's characters or obtains the film of wafer material surface through colloid chemistry theory. It involves the transition from **liquid sol** to **solid gel phase**. The transition process is called gelatification. It includes two chemical reactions: hydrolyzation and polycondensation. The raw material of the Sol-Gel method is several hundred -nanometer particles (inorganic or organic salts). They gelate and become film through hydrolyzation and polycondensation reaction. Finally, products with certain structure surface or shape are obtained through dryness and sintering.

Advantages of Sol-Gel method: (1) The cost of raw materials is low. (2) The requirement of the purity is not rigorous. (3) Since the raw materials are solution state, mixture uniformity extent may arrive to molecule level. (4) A batch of raw material can process several glass rods (the typical size of rod: several mm for outer diameter and tens of centimeters for length. Doping time is several hours depending on doping different compositions and diameter). (5) The temperature of the processing (room temperature) is lower than vapor deposition method (at least 1500 $^\circ$C for sintering

perform). (6) Since the kind of raw material can be added in solution state and processing temperature is low, so the component region of the fiber materials can be enlarged. (7) The utilization efficiency of raw material is very high (close to 100%).

Disadvantages of Sol-Gel method: (1) it is based on several processing steps requiring a strong control of the environment to limit degradations. (2) The repetitious capability of the product quality is difficult to maintain. (3) The period of production is relatively long. (4) The method is not convenient to produce large size preforms.

I.3.2.2 Rod-in-tube method

Rod-in-tube method is namely that one glass rod (which defines the core of the fiber) is inserted into one glass tube (which defines the cladding of the fiber). The illustration of Rod in tube method is shown in figure 1.7.

Figure 1.7: Representation of the rod in tube method

The advantage of this method is it simplicity, and because core and cladding can be fabricated separately, their material compositions can be selected over a wide range. However, the fabrication procedure is difficult. The core rod and the tube for the cladding require special techniques for their fabrications, such as incision, finish milling, polishing. Moreover, a great care has to be taken in the surface quality of both rods and tube (inner surface) since that interface between core and cladding could increase the scattering losses. In this method, if core rod is fabricated through sintering powder, great care is also required to reduce the contamination of crucible (for vitrifying multicomponents glass powders) for low-loss fiber.

I.3.2.3 Double crucible method

The double crucible method is proposed by Midwinter et al. in 1979 [35]. It consists in inserting fiber core and cladding materials into two coaxial crucibles for melting them. The higher limit of the heating temperature for this method is around 1600 $^{\circ}$C. So fiber with high ratio of silica cannot be fabricated by this method. The double crucible method is illustrated in figure 1.8.
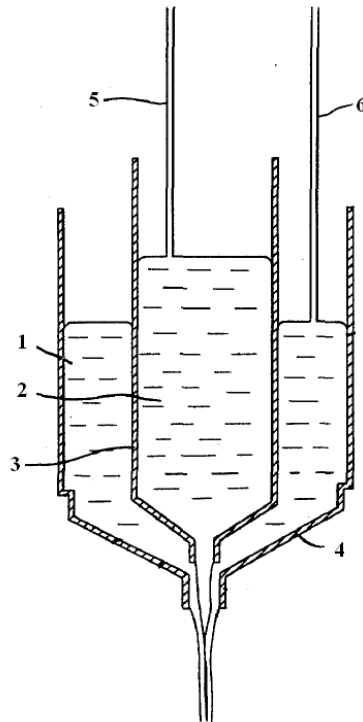
Figure 1.8: Double crucible method. 1. Fiber Cladding glass liquid; 2.Fiber core glass liquid; 3.Inner crucible 4. Outer crucible; 5. Tube for filling fiber core glass material; 6.Tube for filling fiber cladding glass material.

In 2000, James G. Anderson et.al from Corning company still applied double crucible method for drawing fiber [36]. They minimized the diffusion between the core and cladding by preselecting the distance of the tips of two crucibles. And they also can increase or decrease the diameter of the fiber core by applying positive or negative pressure to the first crucible.

The advantages of the double crucible method are: It can continuously produce very long length fiber (>2500 meters), and it also takes full advantage of raw material to keep low cost.

The drawbacks of double crucible method are: (1) the contamination of the crucible is a source of losses (the impurity contamination of Pt crucible are mainly iron and copper). (2) During the process, the materials of the core and the cladding easily diffuse one into another.

I.3.2.4 Core-suction method

The core-suction method is proposed by Nitin K. Goel et.al in 2006 [37]. It is used to fabricate the preform with the non-conventional core glass materials. The first fiber proposed by N. K. Goel composed of a non-conventional core glass material was designed to get high nonlinear coefficient.
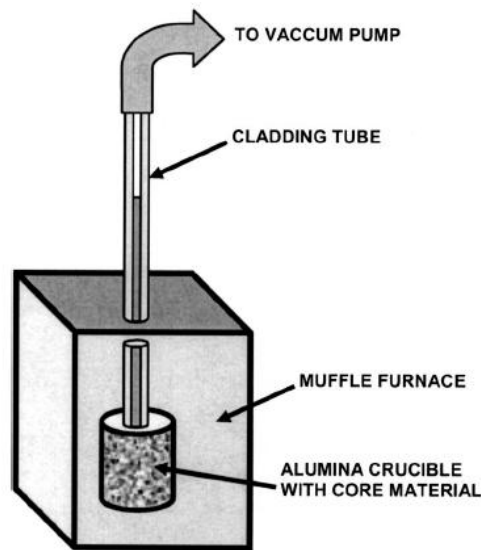
Figure 1.9: Diagram of the core-suction technique

The fabrication process is shown in figure 1.9. The core glass material is melted in an alumina crucible put in muffle furnace. After this operation, the molten core is aspirated into the cladding tube by a vacuum pump to get the preform.

The advantages of this method: (1) Only very small quantities of molten core materials are used, some high-purity and expensive material can be used. (2) Even materials which have toxic constituents can be used since the atmosphere could be controlled and very small quantities of raw material are used. (3) Avoiding some

additional processing steps of previous methods (double crucible method, rod-in-tube method). This will reduce contamination of the core glass in the final fiber. (4) The suction process also avoids bubbles from trapped air, which have occurred in earlier crucible techniques. The disadvantages of this method are: (1) It restricts the choice of core material to glasses with much lower softening temperature than the one of the tube material. This large difference of softening temperatures (often accompanied by a large difference of expansion coefficient) will make drawing low loss fiber to become one challenge. (2) The length of fabricated preform is limited by the depth of furnace (when molten liquid core material in the preform part which is out of the furnace will cool down quickly, it can't continue to flow upwards).

I.3.2.5 Pressure-assisted melt-filling method

In 1992, M. Fokine et.al proposed to melt and fill metal into fiber to fabricate a fiber with metal wire [38]. In 2007, M. A. Schmidt et.al applied similar technology to fabricate a photonic crystal fiber with metal wires [39]; and later they also applied this pressure-assisted melt-filling method to insert high index glass to photonic crystal fibers (PCFs) [40-42] or silica capillary fibers [43]. The pressure-assisted melt-filling setup is shown in Figure1.10. One silica crucible with small quantity of glass is placed inside a silica tube. The later is externally heated with a vertical tubular resistance furnace. Capillaries and PCFs are placed in the silica tube. One of their ends is immersed in the molten glass liquid. The other end is flame sealed. Molten glass liquid is pressed into the holes of a fiber by gas pressure that is inserted into the glass tube.

This method needs only a very small quantity of glass material, and can be used to fabricate many kinds of multi-materials fiber. But the length of the fabricated fiber is limited by the length of furnace. So this method is not appropriated to fabricate a continuous long length multi-materials fiber. In fact, this method is essentially similar to the core-suction method. Both methods melt core material, and by exoteric pressure, insert molten core material to a cladding tube or the hole of fiber. Because in the pressure-assisted melt-filling method, only molten core material is pressed to fiber, so

less quantities core material are needed, but the length of the fiber produced is very short (some centimeters)
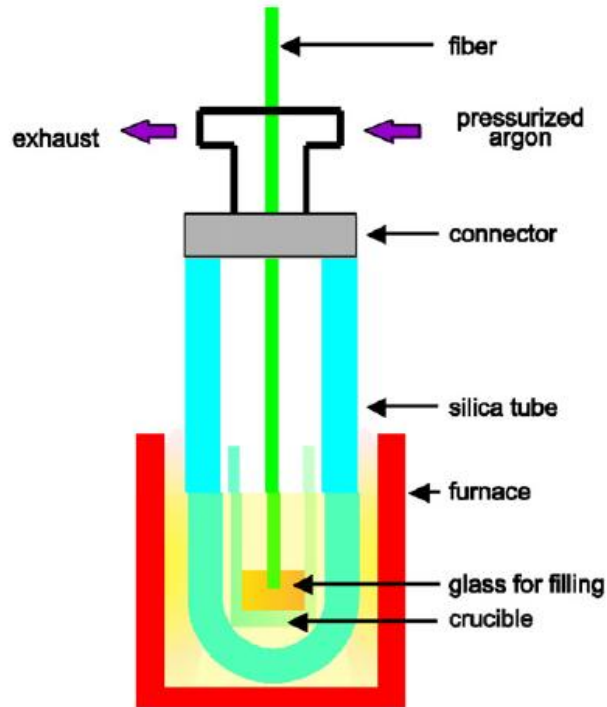
Figure 1.10: Schematic representation of pressure cell used to fill silica photonic crystal fibers and capillaries with low-melting glasses [41].

I.3.2.6 Powder doping method

In this part, we quote three kinds of powder doping methods: (1) Classical melting glass powder mixture method (2) Repusil technique (3) Powder-in-tube method. By methods (1) and (2), doped core rod can be fabricated, and then drawn by rod-in-tube method. In method (3), fiber is directly obtained through drawing glass tube inserted by the powder.

The challenges for these powder-doping technologies are to minimize the number of bubbles and the defect density and crystallization tendency of some metal oxidation components in powder through optimizing vitrification step and the sintering parameters (mechanical parameters to adjust).

I.3.2.6.1 Classical melting glass powder mixture method

The classical method of fabricating multicomponent glass is a melting procedure which includes homogenization of all kinds of glass powder, sintering and melting in metal crucible [32]. In 1973, the researcher of Bell lab [44, 45] and Daisuke Kato in Japan [46] respectively reported the fabrication of one pure silica core and borosilicate cladding optical fiber by melting SiO_2 and B_2O_3 glass powders. By reasonably adjusting the ratio of SiO_2 and B_2O_3 glass powders, they can make the refractive index of borosilicate glass slightly lower than pure silica core to form an optical waveguide based on total internal reflection mechanism. Daisuke Kato in Japan [46] reported the loss of their fiber to be 20 dB/km at 632.8 nm. At the same time, by chemical vapor doposition (CVD) method, the researcher of Bell lab reported the loss of their fiber (it was also pure silica core and borosilicate cladding optical fiber) to be about 7.5 dB/km at 630 nm [47]. After, the chemical vapor deposition (CVD) method was improved; the losses of fibers composed of a GeO_2-SiO_2 core and a SiO_2 cladding was lower again [25]. Classical melting glass powder mixture method cannot compete with modified chemical vapor doposition method (MCVD) to fabricate low loss optical fiber.

But in the last few years, for fabricating highly doped fiber, the classical melting glass powder mixture method is again applied [32, 33, 48, 49] because of the doping concentration limitation of MCVD methods.

More recently, in 2012, Vladimir V.Velmiskin et.al. also reported their work on fabricating a silica fiber with Yb/Al-doped core by classical melting glass powder mixture method [50]. They also fabricated the core rod through sintering multicomponent glass powder. Noticeably, they have adapted their process to reduce bubble formation which is a factor of optical losses. During the preform consolidation process, they have reduced the pressure in the silica tube to 10^{-2} Torr. In order to improve the homogeneity of the doped glass (when the size of inhomogeneity is comparable to the working wavelength, it will lead to significant light scattering), they also proposed to use the stack-and-draw method (to form a larger core from stacking several core rods with smaller core) for more homogenous. After sintering a

silica tube with mixed multicomponents glass powder, the silica cladding was removed by etching with 40% hydrofluoric acid (HF). Then drawn these doped glass rods to 1 mm diameter and cut it into 30 cm long length pieces. Next, stacking these small pieces into one large silica tube (see figure 1.11). Finally, the silica tube was heated to softening temperature of silica glass and sintered into a monolithic rod while pumped to a reduced pressure in silica tube. They claim that the process can improve the homogeneity by a factor of 10. After three repeated process (drawing-stack-consolidation cycle), the non-absorption related losses can be reduced to 100 dB/km.
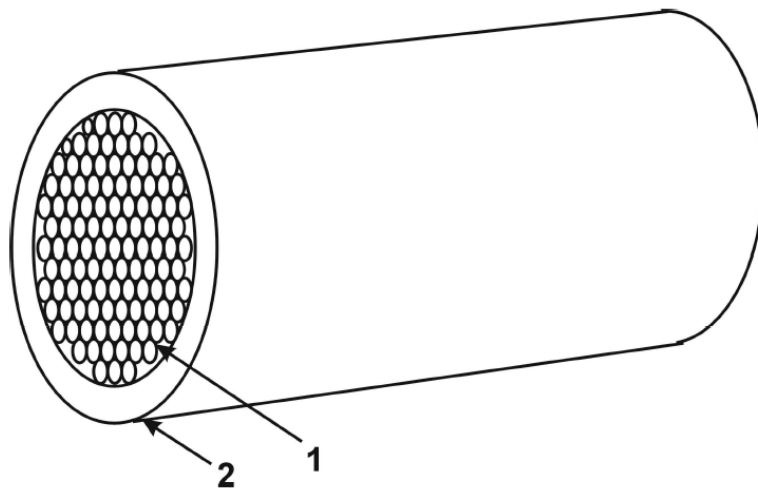
Figure 1.11: Perform assembly schematic: (1) doped silica rod (2) Silica tube [50].

I.3.2.6.2 Repusil Method

To fabricate an Yb doped optical fiber composed of a large doped area with good homogeneity, for laser application, the Insitute of Photonic Technology (IPHT) and Heraeus Quarzglas Company in Germany explored Repusil technique to overcome the drawback of MCVD method: the size limitation of doped region and non-uniformity (doping levels is gradients) [51-55].

They have executed the following steps:

(1) Porous SiO_2 nano-particles are dissolved in a liquid to form an aqueous suspension.

(2) The dopants are added by mixing a solution with dopants.

(3) The suspension is dehydrated and granulated to get doped glass powder.

(4) After further dehydration and purification, these doped glass powders are sintered in a furnace to achieve bubble-free and homogeneous doped bulk silica.

Finally, the core rod can be fabricated by mechanical process, by putting it in a pure silica tube to draw optical fiber by rod-in-tube method.

I.3.2.6.3 Powder-in-tube method

In the methods I.3.2.6.1 and I.3.2.6.2, when melting glass powder in metal crucible to get doped bulk silica, the contamination of crucible is rigorously controlled if a low loss fiber is desired. To overcome the crucible contamination problem and the drawbacks of rod-in-tube method, the Powder-in-tube method is proposed. Powder-in-tube method was proposed by John Ballato et.al in 1995 for first time [56]. This method is similar to Rod-in-tube method, except that the glass rod (as fiber core material) is replaced by glass powder and vitrification process for the glass powders progresses during fiber drawing. John Ballato et al. have developed this process to fabricate optical fibers with highly doped rare-earth (54wt.%Tb_2O_3, 27wt.% SiO_2,18 wt.%Al_2O_3 and 1wt.%Sb_2O_3). They have fabricated such a fiber, but the losses were too high, that were not able to measure its attenuation coefficient. They attribute the high losses to the low purity of the starting powder. The Powder-in-tube method is illustrated in figure 1.12.
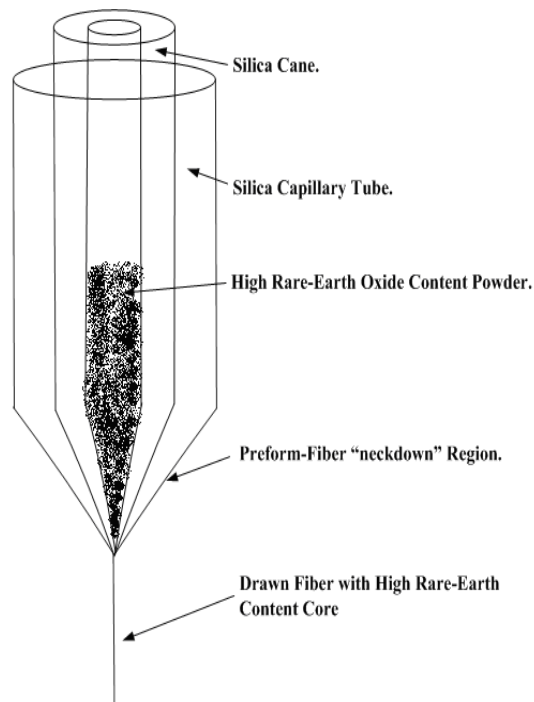
Figure 1.12:   Schematic of powder-in-tube method [56]

Later, in 2006, Ruth Renner-Erny et.al and also Silitec Fibers SA Company (C.Pedrido) have further developed the powder-in-tube method [57, 58].They have made not only the core material of the fiber preform from a glass powder, but also have made the cladding material as well. This method reduces production cost, because silica glass powder is cheaper than the same mass silica glass rod. In their preform, the core region of fiber preform is filled with a powder mixture of SiO_2, 1%Nd (as Nd_2O_3), 10%Al (Al_2O_3), this tube is mounted in the center of a larger tube which form the future cladding. The empty space between the two tubes is filled with undoped SiO_2 powder.

21
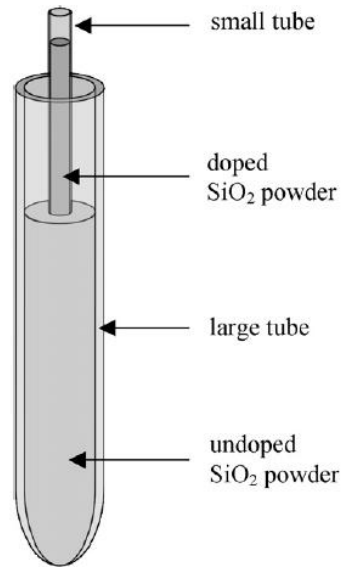
Figure 1.13: Improved powder-in-tube method

In 2009, B. Scott et.al fabricated a silicon core fiber by powder in-tube method [59, 60]. They put silicon powder into silica tube, and then directly draw the silica tube with silicon powder. A fiber sample of 7 cm length was characterized, but too high optical losses were found. They attributed the high losses to irregularities, such as micro-cracks at the boundary between the core and he cladding materials induced by thermal expansion mismatch.

The drawback of powder-in-tube method is that air bubbles among glass powder are hard to eliminate completely. Because some eliminating-bubble techniques (such whisking glass liquid for removing bubble) used in conventional crucible are hard to apply since dimensions of the glass tube are small. These air bubbles will induce high optical losses due to light scattering from the fiber core.

Our research group has improved the fabrication technology of powder-in-tube by optimizing the preheating temperature and time before drawing the fiber (the process gives air bubble enough time to escape powder). The group has also appropriately reduced pressure in the top of preform during fiber drawing (the process means that when outer pressure decreases, inner pressure in air bubble will make air bubble expand to crack) [61]. In 2010, we have realized a SAL fiber (70%SiO_2, 20%Al_2O_3, 10%La_2O_3) with an attenuation coefficient around 1.5 dB/m in the wavelength range

500 nm-1700 nm [32, 62]. The cross section of the SAL fiber is illustrated in figure 1.14(a). And at the same time, the process was also combined with the stack and draw technique to fabricate a photonic crystal fiber with a SAL core. A microscope photography of its cross section is shown in figure 1.14(b)).

(a)   (b)
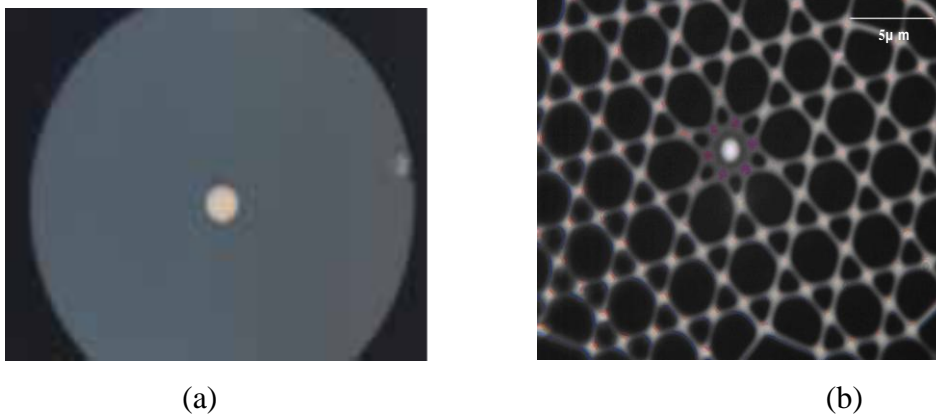
Figure 1.14: Cross section of (a) our SAL fiber (core diameter=10 μm , cladding diameter=120 μm and (b) our photonic crystal fiber with SAL core [62].

With this powder-in-tube method, our research group has also drawn a doped GeO_2 silica core and silica cladding optical fiber with loss of 15-20 dB/m at 1500 nm-1650 nm. A cross section picture of drawn fiber is shown in figure 1.15

Figure 1.15: Doped GeO_2 silica core (88%SiO_2 and 12% GeO_2) silica cladding fiber [61]

This method was also used to fabricate an optical fiber composed of a silica cladding and a core of N-SF6 glass (27%SiO_2, 71%PbO, 1%K_2O, 0.5% NaO, 0.3% As_2O_3) from Schott Company. The cross section picture of the drawn fiber is shown in

figure 1.16. The attenuation coefficient of this fiber is around 1 dB/m at 800 nm-1200 nm.
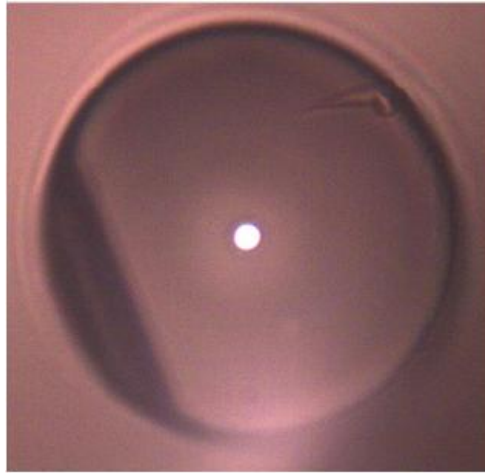
Figure 1.16: N-SF6 glass core and silica cladding fiber

In the following table, the comparison of the several kinds of fabrication methods of highly doped silica fiber is resumed:

Method	Applicable fiber type	Procedure	Equipment	Cost	Fiber loss
The sol-gel method	Glass fiber	Complex	Especially design	Low	middle
Rod-in-tube method	Glass fiber	Complex	General	high	high
Double crucible method	Glass fiber	Simple	Especially design	low	high
Core-suction method	Glass fiber	Simple	Especially design	low	low
Pressure-assisted melt-filling method	Glass fiber	Simple	Especially design	low	high
Classical melting Glass powder mixture method	Glass fiber	complex	general	low	low
Repusil technique	Glass fiber	complex	general	low	low
Powder-in-tube method	Glass fiber	Simple	General	low	high

Table 1.2: *Comparison of the several kinds of fabrication methods of highly doped silica fiber*

For highly doped fibers' fabrication, sol-gel and rod-in-tube method are relatively complexes. The double crucible, the core-suction and the pressure-assisted melt-filling methods require especially designed and fabricated equipments. However, glass powder methods are interesting because of the low cost of production. The glass powders or the powder of other materials (such as metal, semiconductor) are cheaper than bulk materials. These methods need simple procedures and do not introduce strong scattering losses at the surface between the core and the cladding, which is not in the case of the rod-in-tube method.

Because of the crucible contamination problem and the drawbacks of rod-in-tube method, classical melting glass powder mixture method and Repusil method are also abandoned. Because powder-in-tube method is simpler (vitrification process for glass powders can be done during the fiber drawing) and cheaper (raw material is in powder format), we selected powder-in-tube technique for developing our multi-material fibers. Although air bubbles among glass powder is hard to eliminate completely, and low loss fiber is not easy to get, our research group develops this method and applied some new techniques to reduce fiber losses. When the softening temperature of the core material is lower than the one of the tube material (often silica glass), the vitrification process during the fiber drawing step, of the powder (in the core) will be easier since the powder is vitrified before the tube starts to melt. However, when core material has a softening temperature close to the one of the tube material, it will be difficult to realize the vitrification process of the powder during the fiber drawing since both materials tend to mix each other. So, a pre-process is required. It consists in heating the glass tube with glass powders inside at high temperature furnace for some time to remove air bubbles and to consolidate powder granulates together to limit material mixing during the drawing.

I.4 Conclusion

In this chapter, we firstly introduced the concept and main types of optical fibers. Then, we introduced all kinds of fabrication methods of the preform of conventional

low doped silica fibers. Next, all kinds of fabrication methods of highly doped fiber (specially for three kinds of powder methods: Classical melting glass powder mixture method, Repusil method, Powder-in-tube method) were introduced detailedly. Finally, we compared the advantages and drawback of these fabrication methods and decided to select the powder-in-tube method which has the potential of the most convenience and the least contamination for the fabrication of our multi-material fibers.

Reference

[1] Max Born and Emil Wolf, "Principles of optics: electromagnetic theory of propagation, interference and diffraction of light", 7th edition. Cambridge, UK: Cambridge University Press, 1999.

[2] K. C. Kao and G. A. Hockham, "Dielectric-fibre surface waveguide for optical frequencies", Proceedings of the IEE, 1966, Vol.113,No.7, p1151-p1158.

[3] E.P.Kapon, D.B.Keck, and R.D. Maurer, "Radiation losses in glass optical waveguides", Applied Physics Letters, 1970, Vol.17, p423-p425.

[4] W. G. French, J. B. MacChesney, P. B. O'Connor, and G. W. Tasker, "Optical waveguide with very low losses", The Bell System Technical Journal, 1974, Vol.53, No.5, p951-p954.

[5] T. Miya, Y. Terunuma, T. Hosaka, and T. Miyashita, "Ultimate low-loss single-mode at 1.55 μm", Electronics Letters, 1979, Vol.15, p106-p108.

[6] Philip St.J. Russell, "Photonic-Crystal Fibers", Journal of Lightwave Technology, 2006, Vol.24, No.12, p4729-p4749.

[7] S. Kawanishi, T. Yamamoto, H. Kubota, et.al., Dispersion controlled and polarization maintaining photonic crystal fibers for high performance network systems, IEICE Transactions on Electronics, 2004, E87-C(3): p336-p342.

[8] J.S. Wang, E.M. Vogel 1, E. Snitzer, "Tellurite glass: a new candidate for fiber devices", Optical Materials, 1994, Vol. 3, Vol.3, p187-p203.

[9] D.W. Hewak, R.C. Moore, T. Schweizer, J. Wang, B. Samson, W.S. Brocklesby, D.N. Payne and E.J. Tarbox, "Gallium lanthanum sulphide optical fibre for active and passive applications", Electrons letters, 1996, Vol. 32, No. 4, p384-p385

[10] Xian Feng, Arshad K. Mairaj, Daniel W. Hewak, and Tanya M. Monro. "Nonsilica glasses for holey fibres", Journal of Lightwave Technology, 2005, Vol.23, No.6, p2046-p2054.

[11] X. Feng, T.M. Monro, V. Finazzi, R.C. Moore, K. Frampton, P. Petropoulos and D.J. Richardson, "Extruded singlemode, high-nonlinearity, tellurite glass holey fibre", Electrons letters, 2005, Vol.41, No.15, p835-p837.

[12] T. M. Monro, Y. D. West, D. W. Hewak, N. G. R. Broderick, and D.J. Richardson, "Chalcogenide holey fibers," Electron Letters, 2000, Vol. 36, p1998–p2000.

[13] Govind P.Agrawal. "Nonlinear fiber optics", the third edition, 2001, Academic Press, p3.

[14] V. Kumar, A. K. George, W. H. Reeves, J. C. Knight, P. S. Russell, F. G. Omenetto, and A. J. Taylor, "Extruded soft glass photonic crystal fiber for ultrabroad supercontinuum generation", Optics Express, 2002, Vol.10,No.25, p1520-p1525.

[15] P. Petropoulos, T. M. Monro, H. Ebendorff-Heidepriem, K. Frampton, R. C. Moore, and D. J. Richardson, "Highly nonlinear and anomalously dispersive lead silicate glass holey fibers", Optics Express, 2003, Vol.11,No.26, p3568-p3573.

[16] N. Granzow, S. P. Stark, M. A. Schmidt, A. S. Tverjanovich, L. Wondraczek, and P. St.J. Russell, "Supercontinuum generation in chalcogenidesilica step-index fibers", 2011, Vol. 19, No.21, p21003-p21010.

[17] H. Ebendorff-Heidepriem, P. Petropoulos, S. Asimakis, V. Finazzi, R.C. Moore, K. Frampton, F. Koizumi, D.J. Richardson, T.M. Monro , "Bismuth glass holey fibers with high nonlinearity", Optics Express, 2004, Vol.12, No.21, p5082-p5087.

[18]N. Sugimoto, T. Nagashima, T. Hasegawa, S. Ohara, K. Taira, and K. Kikuchi, "Bismuth based optical fiber with nonlinear coefficient of 1360 W^{-1} km^{-1}", Optical Fiber Conference(OFC) 2004, Los Angeles, California, USA, 2004, paper PDP26.

[19]T. Li (ed.), Optical Fiber Communications: Fiber Fabrication, Vol.1 (Academic Press, San Diego, 1985).

[20] Paek, "High-speed high-strength fiber drawing", Journal of Lightwave Technology, 1986, Vol. 4, No.8, p1048-p1060.

[21] S. R. Nagel, J. B. MacChesney, and K. L. Walker, "An overview of the modified chemical vapor deposition (MCVD) process and performance", IEEE Journal of Quantum Electron, 1982, Vol. QE-18, No.4, p459-p476.

[22] M. G. Blankenship and C. W. Deneka, "The outside vapor deposition method of fabricating optical waveguide fibers", IEEE Journal of Quantum Electron, 1982, Vol.QE-18, No.10, p1418-p1423.

[23] K. Inada, "Recent progress in fiber fabrication techniques by vapor-phase axial deposition", IEEE Journal of Quantum Electron, 1982, Vol.QE-18, No.10, p1424-p1431.

[24] Hans Lydtin, "PCVD: A Technique Suitable for Large-scale Fabrication of optical Fibers", IEEE Journal of Lightwave Technology, 1986, Vol.LT-4, No.8, p1034-p1038.

[25] J. B. MacChesney, P. B. O'Connor, and H. M. Presby, "A new technique for preparation of low-loss and graded index optical fibers", Proceedings of the IEEE, 1974, Vol. 62, No. 9, p1278- p1279.

[26] J. B. MacChesney, P. B. O'Connor, F. V. DiMarcello, J. R. Simpson, and P. D. Lazay, "Preparational low loss optical fibers using simultaneous vapor phase deposition and fusion", in Proc. 10th Int. Congr. Glass, 1974, p6-40-p6-44.

[27] J. F. Hyde, "Method of making a transparent article of silica," and development in optical waveguide technology processes and prod-U.S. Patent 2 272 342, February. 10, 1942.

[28] D. B. Keck and P. C. Schultz, "Method of producing optical waveguide fibers," U.S. Patent 3 711 262, January, 16, 1973.

[29] T. Izawa, S. Kobayashi, S. Sudo, and F. Hanawa, "Continuous fabrication of high silica fiber preforms," presented at the Internal Confonference on Integrated Optics and Optical Communication, Tokyo, Japan, June 1977.

[30] P.Geittner, D.Kuppers,and H.Lydtin, "Low-loss optical fibers prepared by plasma-activated chemical vapor deposition(CVD) ", Applied physics letter, Vol.28, No.11, p645-p646, June, 1976.

[31] Mathieu Devautour, Philippe Roy, Sébastien Février, Carlos Pedrido,Frédéric Sandoz, and Valerio Romano, "Nonchemical-vapor-deposition process for fabrication of highly efficient Y doped large core fibers", Applied optics, 2006, Vol.48, No.31, p2715-p2720.

[32] K. Schuster, J. Kobelke, D. Litzkendorf, A. Schwuchow, F. Lindner, J. Kirchhof, H. Bartelt, J.-L. Auguste, G. Humbert, J.-M. Blondy, "Structured material combined HMO-Silica Fibers – preparation, optical and mechanical behavior", Proceedings of SPIE, 2011, Vol.7934, p.79340O.

[33] Kay Schuster , Jens Kobelke, Stephan Grimm , Anka Schwuchow, Johannes Kirchhof , Hartmut Bartelt, Andreas Gebhardt, Philippe Leproux , Vincent Couderc ,Waclaw Urbanczyk, "Microstructured fibers with highly nonlinear materials", Optical and Quantum Electron, 2007, Vol.39, p1057-p1069.

[34] K. Kitagawa, S. Shibata, M. Horiguchi, "Fabrication of single-mode optical fiber preform by sol-gel method", Electronics and Communciations in japan, 1989, Vol.73, No.6, p22-p28, 1990.

[35] J.E Midwinter, C.R. Day, "Drawing dielectric optical waveguides", Brevet US US4101305, 1978.

[36] James G. Anderson, Ernest E. Brand, Adam J. Ellison, Jackson P. Trentelman, "Process for drawing optical fiber from a multiple crucible apparatus with a thermal gradient", US 6550279, 2000.

[37] Nitin K.Goel and Roger H.stolen, steven Morgan, Jong-Kook kim, Dan Kominsky and Gary pickrell. "Core-suction technique for the fabrication of optical fiber preforms", Optics Letters, 2006,Vol.31, No.4, p438-p440.

[38] M. Fokine, L. E. Nilsson, Å. Claesson, D. Berlemont, L. Kjellberg, L. Krummenacher, and W. Margulis. "Integrated fiber Mach–Zehnder interferometer for electro-optic switching", Optics Letters, Vol.27, No.18, p1643-p1645.

[39] M. A. Schmidt, L. N. Prill Sempere, H. K. Tyagi, C. G. Poulton, and P. St.J. Russell, "Waveguiding and Plasmon Resonances in Two-Dimensional Photonic Lattices of Gold and Silver Nanowires", Physics Review B, 2008 ,77, p033417.

[40] Markus A. Schmidt, Nicolai Granzow, Ning Da, Mingying Peng, Lothar Wondraczek, and Philip St. J. Russell. "All-solid bandgap guiding in tellurite-filled silica photonic crystal fibers", Optics Letters, 2009, Vol.34, No.13, p1946-p1948.

[41] Ning Da, Lothar Wondraczek, Markus A. Schmidt, Nicolai Granzow, Philip St. J. Russell "High index-contrast all-solid photonic crystal fibers by pressure-assisted melt". Journal of Non-Crystal Solids, 2010, Vol.356, p1829-p1836.

[42] Nicolai Granzow, Patrick Uebel, Markus A. Schmidt, Andrey S. Tverjanovich, Lothar Wondraczek, and Philip St. J. Russell. "Bandgap guidance in hybrid chalcogenide–silica photonic crystal fibers". Optics Letters, 2011, Vol. 36, No. 13, p2432-p2434.

[43] N. Granzow, S. P. Stark, M. A. Schmidt, A. S. Tverjanovich, L. Wondraczek, and P. St.J. Russell. "Supercontinuum generation in chalcogenidesilica step-index fibers", Optics Express, 2011, Vol.19, No.21, p21003-p21010.

[44] L. G. Van Uitert, D. A. Pinnow, J. C. Williams, To Co Rich, R. E. Jaeger and W. H. Grodkiewicz, "Borosilicate glasses for fiber optical waveguides ", Materials Research Bulletin, 1973, Vol.8, No.4, p469-p476.

[45] S.H.Wemple, D.A.Pinnow, T.C.Rich, R.E.jaeger, and L.G.van uitert, "Binary SiO_2-B_2O_3 glass system: Refractive index behavior and energy gap considerations", Journal of Applied physics, 1973, Vol.44, No.12, p5432-p5437.

[46] Daisuke Kato, "Fused-silica-core glass fiber as a low-loss optical waveguide", Applied Physics Letters, 1973, Vol.22, No.1, p3-p4.

[47] William G. French, A. David Pearson, G. William Tasker, and John B. MacChesney, "Low -loss fused silica optical waveguide with borosilicate cladding", Applied physics letters, 1973, Vol.23, No.6, p338-p339.

[48] J. Kobelke, K. Schuster, S. Grimm, D. Litzkendorf , J. Kirchhof, A. Schwuchow, H. Bartelt, A. Gebhardt, "Multicomponent glass microstructured fibers for nonlinear applications", Proceeding of SPIE, 2008, Vol.6990, p699005.

[49] J. Kobelke, K. Schuster, D. Litzkendorf , A. Schwuchow J. Kirchhof, H. Bartelt, V. Tombelaine, P. Leproux, V. Couderc, A. Labruyere, "Microstructured fibers with high lanthanum oxide glass core for nonlinear applications", Proceeding of SPIE, 2009, Vol.7357, p.735702.

[50]Vladimir V. Velmiskin, Olga N. Egorova, Vladimir Mishkin, Konstantin Nishchev, Sergey L.Semjonov, " Active material for fiber core made by powder- in -tube method: subsequent homogenization by means of stack-and-draw technique", Proceeding of SPIE, 2012, Vol.8426, p84260I-1.

[51] A. Langner, G. Schötz, M. Such, T. Kayser, V. Reichel, S. Grimm, J. Kirchhof, V. Krause, and G. Rehmann, "A new material for high power laser fibers", Proceeding of SPIE, 2008, Vol. 6873, p687311.

[52]Andreas Langner, Gerhard Schötz, Mario Such, Volker Reichel, Stephan Grimm, "Comparison of silica-based materials and fibers in side- and end-pumped fiber lasers", Proceedings of SPIE, 2009, Vol.7195, p71950Q.

[53] Andreas Langnera, Mario Sucha, Gerhard Schötza, Volker Reichelb, Stephan Grimmb, Florian Justb, Martin Leichb, Johannes Kirchhofb, Björn Wedelc, Gunnar Köhlerc, Olaf Strauchc, Oliver Mehlc, Volker Kraused, Georg Rehmannd, "Development, manufacturing and lasing behavior of Yb-doped ultra large mode area fibers based on Yb-doped fused bulk silica", Proceedings of SPIE, 2010, Vol.7580, p75802X.

[54] Andreas Langner, Mario Such, Gerhard Schötz, Stephan Grimm, Florian Just, Martin Leich,Christian Mühlig, Jens Kobelke, Anka Schwuchow, Oliver Mehl, Olaf Strauch, Roman Niedrig, Björn Wedel, Georg Rehmann, Volker Krause, "New developments in high power fiber lasers based on alternative materials", Proceedings of SPIE, 2011, Vol.7914, p79141U.

[55] Martin Leich, Florian Just, Andreas Langner, Mario Such, Gerhard Schötz, Tina Eschrich, and Stephan Grimm, "Highly efficient Yb-doped silica fibers prepared by powder sinter technology", Optics Letters, 2011, Vol.36, No.9, P1557-p1559.

[56] J. Ballato, E. Snitzer, "Fabrication of fibres with high rare-earth concentrations for Faraday isolator applications", Applied Optics, 1995, Vol.34, No.30, p6848-p6854.

[57] Ruth Renner-Erny , Loredana Di Labio, Willy Luthy, "A novel technique for active fibre production", Optical Materials, 2007, Vol.29, p919-p922.

[58] C. Pedrido, "Optical fiber and its preform as well as method and apparatus for fabricating them", Brevet WO-102947 (2005).

[59] B. Scott, K. Wang, G. Pickrell, "Fabrication of n-type silicon optical fibers", IEEE Photonic Technology Letter, 2009, Vol.21, p1798–p1800.

[60] B. Scott, K. Wang, V. Caluori, G. Pickrell, "Fabrication of silicon optical fiber", Optical Engineering, 2009, Vol.48, p100501.

[61] Stephanie Leparmentier, "Développement et caractérisation de fibres optiques multimatériaux verre/silice ou verre/air/silice réalisées par un procédé basé sur l'utilisation de poudre de verres", Phd thesis, XLIM, university de Limoges, 2010.

[62] Jean-Louis Auguste, Georges Humbert, Stéphanie Leparmentier, Jean-Marc Blondy, Pierre-Olivier, Martin, Gaëlle Delaizir, Doris Litzkendor, Stephan Grimm, Kay Schuster, "Process developments and applications around the powder in tuber technique", 12th advanced laser technologies conference, 2012, Switzerland, p58-p59.

Chapter II. Application of the powder in Tube method for developing solid core photonic bandgap fibers

II.1. Introduction of solid core photonic bandgap fibers

Photonic crystal fiber (PCF) is proposed and realized by P. St. J. Russell and his colleagues in 1990s [1, 2]. The PCF is a kind of optical fiber whose cladding comprises a two dimensional (2D) periodic array of air holes that run down the length of the fiber [3, 4]. This kind of fiber has many novel properties. For example, it can support single mode propagation in the very wide wavelength region [2], it can also realize easily extremely high birefringence [3], ultrahigh nonlinearity [4], and ultra-flattened dispersion [5]. Figure 2.1 illustrates the cross section pictures of different kinds of photonic crystal fibers.

(a)	(b)	(c)

(d)	(e)	(f)
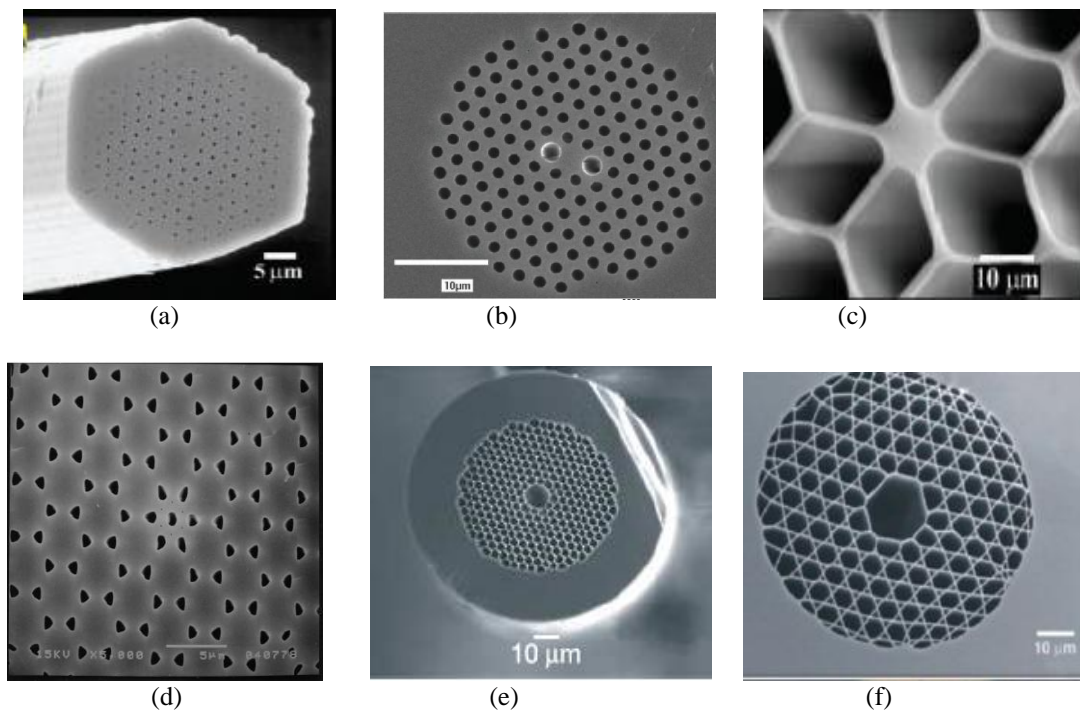
Figure 2.1:The cross section pictures of different kinds of photonic crystal fiber (PCF). (a) Endlessly single mode solid core PCF (b) High birefringence PCF (c) High Nonlinear PCF (d)Honeycomb photonic bandgap PCF (e) Hollow core photonic bandgap fiber (f) Hollow-core Kagomé PCF

There are two kinds of light guiding mechanisms for photonic crystal fiber: total internal reflection and Photonic BandGap (PBG). Total internal reflection guiding mechanism in PCF is similar to step-index fiber; the refractive index of the core region is higher than the average refractive index of the cladding. However, the array of air holes in the cladding offers greater flexibilities in guiding properties.

Photonic bandgap guidance originates from one of the tight-binding models in solid-state physics [6, 7]. In the photonic bandgap wavelength region, light can be guided by high transmission; out of photonic bandgap wavelength region, light can't be guided. Photonic bandgaps are often discrete, so guidance wavelength regions are often also discrete. In the case of photonic bandgap guidance, the PCF's core region may be one large airhole or a material of which refractive index is lower than the surrounding material.

Different kinds of hollow core waveguides have been developed during the last recent years, some are presented in figure 2.2 [7].
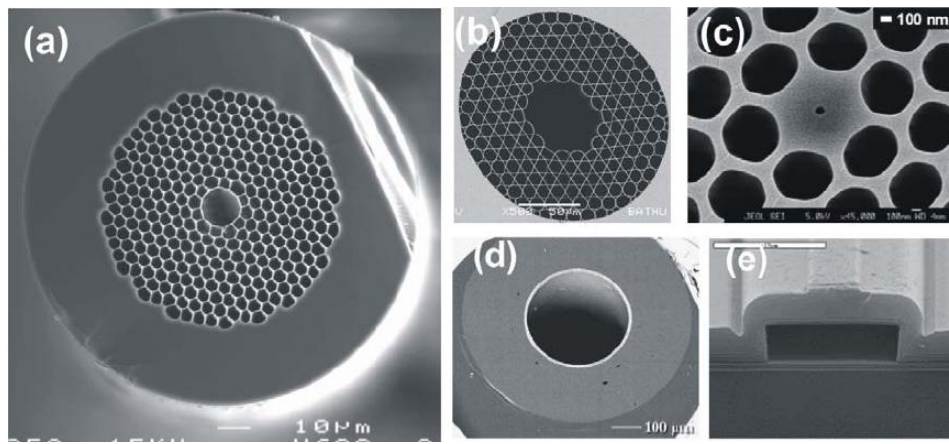
Figure 2.2:   Hollow-core (HC) waveguides: (a) Triangular HC-PCF, (b) Kagome HC-PCF, (c) nano-void fiber, (d) Bragg fiber, (e) Chip integrated waveguide.

In figure 2.2, fiber (a) whose cladding comprises a triangular arrangement of air holes, guides by photonic bandgap (PBG) mechanism. Fiber (b) whose cladding comprises a Kagome lattice arrangement, guides light by virtue of an inhibited coupling between core and cladding modes [7, 8]. Although the loss of the Kagome HC-PCF is much higher than in the triangular HC-PCF, it can guide over a bandwidth 20 times larger than the triangular HC-PCF. Fiber (c) has the distinctive feature of guiding predominantly within a central nano-scaled hollow-core. The light is confined in the hollow region because of the discontinuity of the electric field at the interface between the surrounding silica and the hole [9]. Fiber (d) shows a hollow-core fiber made of two chalcogenide glasses and arranged in concentric layers to form what is called a Bragg optical fiber [10, 11]. With a judicious choice of the layers' indices and spacing, this fiber guides via a PBG over all the possible incident angles (omniguidance) [12]. Fiber (e) guides by virtue of antiresonant reflection optical waveguide (ARROW) mechanism. This structure can be applied to the integration in silicon chip [13].

Although most novel properties of photonic bandgap fibers are found in the hollow core photonic bandgap fibers, photonic bandgap guidance phenomenon is also found in solid core photonic crystal fibers (SC-PCFs) [14-22]. In solid core photonic bandgap fiber, the array of high refractive index inclusions replaces the air-holes array in the cladding of solid core index guidance PCF. The properties of that kind of photonic bandgap fiber are presented and studied in the following sections. A part of the study is focused on the effect of increasing the refractive index of the inclusions (rods) on the properties of the guided modes.

II.1.1.   Guidance mechanism in solid-core photonic bandgap fibers

This kind of fiber can confine the fundamental mode in the fiber core region delimited by rods with an higher refractive index than the one of the core region. An example of a cross section of SC-PBGF is shown in figure 2.3. The white areas correspond to rods composed of Ge-doped silica with higher refractive index than the one of silica ground (gray region).   .
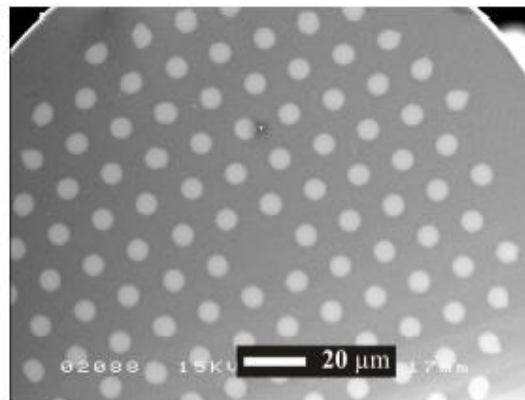
Figure 2.3: Cross section of all-solid photonic bandgap fiber (index contrast is 2.03 %) [23]

A typical transmission spectrum of the SC-PBGF is composed of bands of high transmissions, which is one of the typical signatures of photonic bandgap guidance mechanism. As an illustration, the transmitted spectrum of the SC-PBGF shown in figure 2.3 is depicted by the black curve in figure 2.4.
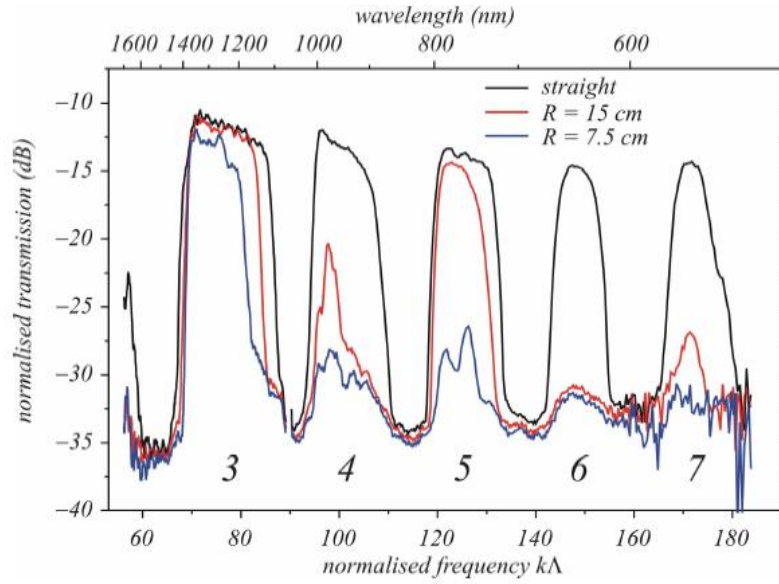
Figure 2.4: Transmission spectra of an all-solid photonic bandgap fiber under different bent radius [23]

This spectrum is composed of fives transmission bands corresponding to bandgap order 3 to 7. The definition of the order of the bandgap will be explained below. When the fiber is bent, its transmission spectra are also shown on the figure by red and blue curves for a bend radius of 15 cm and 7.5 cm, respectively. These spectra highlight a strong sensitivity to bends.

The dispersion diagram of the density of states corresponding to the SC-PBGF of figure 2.3 is shown in figure 2.5. This diagram is obtained by using the plane-wave method that consists in computing all the modes (states) allowed or not on an infinite periodic photonic crystal cladding. This diagram is composed of five bandgaps (red regions) corresponding to the transmission spectra (Cf. figure 2.4). The yellow curves are fundamental core mode index curves. Gray regions are bands of cladding modes corresponding to low transmission bands. These bands are composed by the superposition of modes in every high index rods. These bands are broader as the effective index value decrease. The labeled LP modes are the modes in the high index rod, i.e. cladding mode bands when the effective index is high.
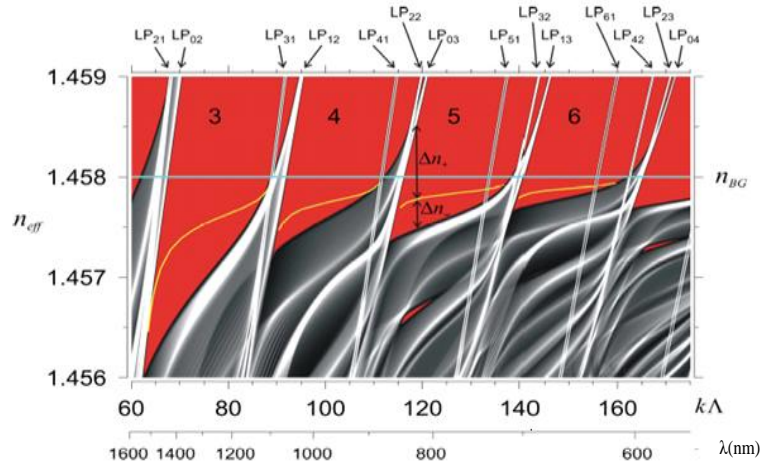
Figure 2.5: Bandgap graph of all-solid photonic bandgap fiber in figure 2.3. Yellow curves are fundamental core mode index curves. Red regions are the passband regions (also called bandgap) which are corresponding to the transmission passband in figure 2.4. Gray regions are prohibited transmission bands, they are composed by the superposition of modes in the every high index rods. n_{BG} is the refractive index of silica background [23].

These bands of cladding modes delimit the bandgaps and therefore the bangap positions could be well approximated by the cutoff positions of LP mode in the rods, i.e. when their effective index reach the refractive index of the fiber ground (silica), as shown in figure 2.5.

This simple approach for determining the bandgap positions could be also explained by the antiresonant reflecting optical waveguide (ARROW) model [16, 22]. The principle of the ARROW model can be understood thanks to figure 2.6 from [16]. It shows two different wavelengths propagating in the center core of a waveguide formed by a low-index core surrounded by two high- and low-index cladding layers. The wavelengths corresponding to the minima of the transmission coefficient are referred to as resonant wavelengths, and the wavelengths corresponding to high transmission parts of the spectrum are called antiresonance wavelengths. This terminology is motivated by the fact that high transmission originates from the antiresonant nature of the individual cladding layers with respect to the transverse propagation constant. Each layer can be considered as a Fabry–Perot (FP) resonator. Narrowband resonances of this FP resonator correspond to transmission minima for the light propagating in the core, or resonant wavelengths of the low-index core waveguide. Wide antiresonances of the FP resonator (wavelengths experiencing low leakage as a result of destructive interference in the FP resonator) correspond to a high transmission coefficient for the low-index core waveguide. The plot below in figure 2.6 shows the transmission spectrum

of this waveguide. Note that in the antiresonance regime, the transmission coefficient is high but not exactly 100%. This coefficient is due to imperfect reflections of the low-high index interfaces. Usually, low-order modes propagate with glancing angles with respect to the interface, and therefore the reflection is quite high and the loss is low, whereas higher-order modes are more lossy because they have larger incident angles.
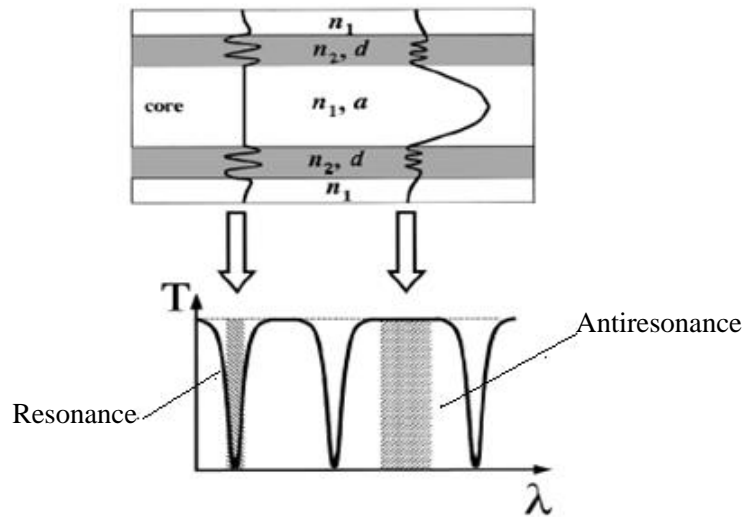
Figure 2.6: Schematic of (top) the ARROW structure and (bottom) its transmission spectrum

According to the ARROW model, the high-index inclusion in the cladding allows resonant light to leak out from the core, i.e. a mode confined in the high-index inclusion is at its cutoff frequency, but reflects light back into the core if they are antiresonant, i.e. the modes are confined in the high-index inclusion. So the confinement of the light depends mainly on the properties of the high-index inclusions. This is indeed demonstrated by the results shown in figure 2.7. It shows the effective index and attenuation coefficient of the fundamental core mode confined by high-index inclusions with the same diameters but along different topologies. These results show that whatever the arrangement of the rods (high-index inclusions) the positions of the transmission bands (bandgaps) are constants, only the attenuation coefficient depends on the arrangement topology of the rods.
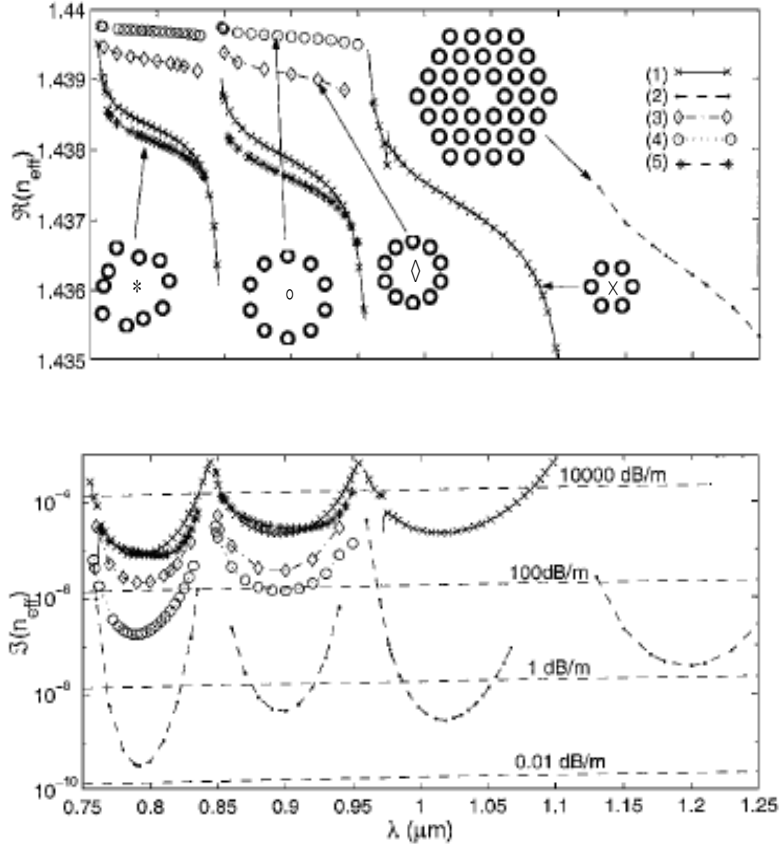
Figure 2.7: (a) and (b) are the real part curves and the imaginary part curves of the effective index of the solid PCF with the high index inclusion with different arrangement of rods.[14]

Therefore, the limits of the bandgaps could easily be approximated by calculating the cutoff frequency of the modes confined in an individual high-index inclusion (rod), it could be obtained with the following relation of the normalized frequency:

$$V_c = \frac{\pi d_{rod}}{\lambda_c} \sqrt{n_{rod}^2 - n_{ground}^2}$$

With V_c corresponding to the values (X) of the Bessel function $J_m(X)$ equal to zero.

Solid-core photonic bandgap fibers (SC-PBGF) provide a promising solution to fabricate unusual optical fibers with the usual process used in conventional fiber drawing. Compared with the air-core bandgap fiber, SC-PBGF enables the realization of original rare-earth-doped amplifiers and lasers [24, 25] or the inscription of Bragg gratings [26-28] that are widely used in optical fiber laser or optical fiber sensors.

II.1.2. Solid-core photonic bandgap fibres with high-index rods

The first reported SC-PBGF was fabricated in 2004 [29] with two kinds of compatible glasses: SF6 glass (as the high index rod, $T_{melting} = 423$ ˚C) and LLF1 glass (as the substrate $T_{melting} = 431$ ˚C) by the stack and draw method. The refractive index of SF6 and LLF1 glass are respectively 1.79 and 1.54 at visible and near-IR wavelength, the refractive index difference is as high as 16%, and loss is high until 18 dB/m.

Following this demonstration, SC-PBGF with a step-index of only 1% was reported [30]. In this structure the ground is silica and the high-index rods are composed of Ge-doped silica. Then, other low loss SC-PBGFs with low index difference (3%) have been reported [31, 32]. As far as we know, until now, the lowest attenuation coefficient reported for an SC-PBGF is 2 dB/km at the wavelength 1310 nm. This result was reported in 2007 by Guobin Ren *et al.* [33, 34]. To get these results they have introduced an index depressed layer around the high-index rod in the cladding of the SC-PBGF. They have also demonstrated a broad transmission band of 700 nm and a low bend loss sensitivity with a critical radius of 8 mm. These results were obtained with a low step index difference between the rods and the silica ground. Recently, high index difference multi-materials SC-PBGFs attracts researchers' large interest [35-37].

In our following discussion, we focus on high index difference (≥ 0.1) SC-PBGFs. In 2009, a tellurite-filled SC-PBGF was fabricated by pressure–assisted filling method [35, 36]. Tellurite glass (its index is $2.08-0.094\lambda$, the unit of λ is micrometer.) is composed by 75 mol.% TeO_2, 10mol.%ZnO, 15 mol.% Na_2O, and its glass transition temperature is 296 ˚C. Light from a PCF-based supercontinuum source (400-1700nm) was launched into the bandgap fiber. The result of measurement indicates that three distinct bands with low optical loss are found between 400 and 1100 nm, with a minimum loss of 1.6 dB/cm at 700 nm, and core mode guidance is prevented in the region of from 1100 nm to 1700 nm. They attribute the high attenuation to optical scattering at microheterogeneity inside the glass.

The same research group (from Erlangen in Germany) have also fabricated a SC-PBGF composed of chalcogenide glass ($Ga_4Ge_{21}Sb_{10}S_{65}$, glass transition temperature: 315 ˚C) and silica by the same pressure–assisted filling method [36, 37]. The transmission spectrum measured is as follows:
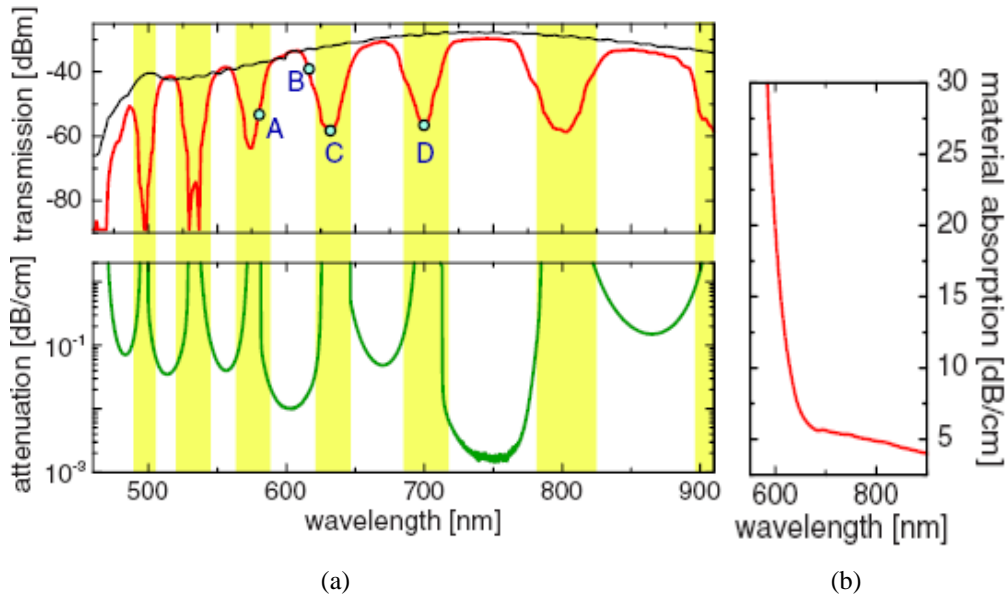
Figure 2.8:(a) Upper diagram: measured transmission spectrum of the core mode of the filled PCF (red curve) and an identical unfilled PCF (black). The filled section started 1mm from the input endface of the PCF and was 5 mm long. Lower diagram: attenuation spectrum of the core mode calculated using a multipole approach. The yellow shaded strips indicate regions of increased attenuation (peaks), coinciding with dips in the transmission spectrum. (b) Material absorption of bulk $Ga_4Ge_{21}Sb_{10}S_{65}$ [37]

From Figure 2.8(a), we can see that the loss in seven distinct transmission windows of filled bandgap fiber is almost as low as the unfilled fiber. The wavelength positions with the lowest attenuation of filled and unfilled fibers are both near 750 nm. Combining with figure 2.6(b) Material absorption curve of bulk $Ga_4Ge_{21}Sb_{10}S_{65}$, we can conclude that the absorption of chalcogenide has only weak effect on the loss of the bandgap region for λ <1000 nm, the transmission loss is almost equal to that of unfilled photonic crystal fiber. When λ >1000 nm, transmission is obviously reduced by chalcogenide absorption due to increasing field penetration into the chalcogenide.

By selecting special high index materials to be filled, these SC-PBGFs open numerous potential applications such as: supercontinuum generation (high nonlinear materials as high index rod), magneto-optics device (magneto-optics material as high index rod), wavelength selective filtering devices (utilizing resonant filtering wave property of SC-PBGF) and rare-earth-doped amplifiers with high gain per unit length (high gain material as high index rod).However, the main limitation of the pressure –assisted filling method is that it only can fabricate continuous several centimeter long length fibers.

Some papers have reported the effects of the variation of the index difference on the properties of bandgap fiber. In the hollow core photonic bandgap fiber, T. A. Birks et.al have reported that increasing index contrast initially makes bandgap to become narrower [38]. A.

Argyros et.al reported that in SC-PBGF, the fiber with low index contrast, has a larger bend sensitivity [39]. N. M. Litchinitser et.al also reported that in the liquid-filled SC-PBGF (liquid is used as high index rods), the refractive index change of liquid will make that the lower order resonant wavelength have larger wavelength shift than higher order resonant wavelength [40]. In the reference [41], Vincent Pureur et al. proposed that in the case of larger index difference, the bandgap will be deeper. They have also calculated [42] that when the d/pitch is fixed to 0.4 and the spectral position of the first bandgap is kept constant (the diameter of high index rod will be adapted to the index difference) when the index difference is increased from 0.01 to 0.1:

(1) The fundamental mode index decreases

(2) The group index increases (and in the long wavelength region, they increase quicker).

(3) The minimum group index related to the zero dispersion wavelength shifts toward the short wavelength side.

(4) The nonlinear coefficient increases.

(5) The confinement loss over all the bandgap increases

Recently Vincent Pureur et.al [43] studied also the effect of increasing the step-index on the mode index difference ($\Delta n_{\text{mod}e}$) between the two first guided modes LP$_{01}$ and LP$_{11}$ and their confinement loss ratio R$_{loss}$= loss$_{(LP11)}$/ loss$_{(LP01)}$, when keeping d/pitch constant, with index contrast increasing from 0.01 to 0.1. They demonstrate that the $\Delta n_{\text{mod}e}$ increases and the R$_{loss}$ decreases.

One important interest of increasing the step-index is shifting the chromatic dispersion curve of the fundamental core mode (shifting zero dispersion wavelength (ZDW)). The fiber with the appropriate ZDW can be applied to fiber laser for keeping the pulse shape at this ZDW [44].it can be also applied to laser delivery for keeping the pulse shape at this ZDW [45]. In Chunshu zhang et.al paper [46], they simulated the dispersion curves of a filled liquid SC-PBGF for different liquid indexes. It is shown in figure 2.9 that the dispersion curve depends on the index of the liquid and ZDW could be obtained at very short wavelengths (depending on the pitch used).
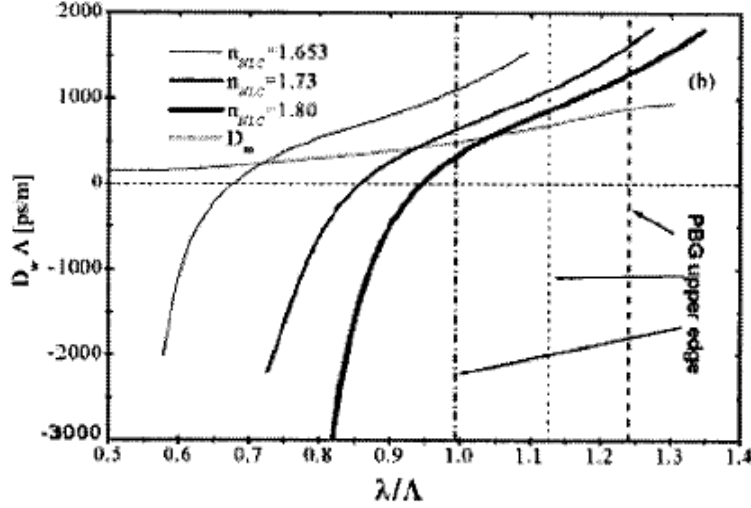
*Figure 2.9 Normalized GVD of the fundamental core mode of an SC-PBGF,
versus normalized wavelength with different refractive index of nematic liquid crytal (NLC)
when the refractive index of NLC is 1.635, 1.73,1.80 [46].*

However, it is important to notice that in their simulations, the diameter and pitch are kept constant leading to a shift of the bandgap position and therefore limiting a quantitative analysis of the ZDW shift versus the step-index variation.

In the following part, we will focus our study on the effects of increasing the index difference on the properties of the fundamental core mode of a SC-PBGF.

II.2. Investigation of high-index rods on the properties of solid-core photonic bandgap fibers

II.2.1. Bandwidths and positions of the photonic bandgaps

Since the edges of the photonic bandgap are delimited by the cut-off wavelengths of the modes guided in an individual rod, we can easily study the influence of the refractive index difference between rods and the fiber background on the photonic bandgap bandwidth by using the following equation that approximates the cut-off wavelengths [47]:

$$\lambda_m \approx \frac{4d}{2m+1}\sqrt{n_2^2 - n_1^2}$$ (2-1)

with n_1 is the background refractive index of fiber, n_2 is the rods refractive index, d is the rod diameter and m is the cut-off wavelength order. From this equation, we can deduce the equation of wavelength interval $\Delta\lambda_m$ of two adjacent resonant wavelengths of m order and m+1 order, which gives an approximation of the bandgap width:

$$\Delta\lambda_m = \lambda_m - \lambda_{m+1} \approx \frac{4d}{2m+1}\sqrt{n_2^2 - n_1^2} - \frac{4d}{2(m+1)+1}\sqrt{n_2^2 - n_1^2}$$

$$\Delta\lambda_m \approx \frac{8d}{4m^2 + 8m + 3}\sqrt{n_2^2 - n_1^2} \qquad (2\text{-}2)$$

For a given rod diameter and ground refractive indexes (n_1), increasing the refractive index of the rods leads to shift the resonance wavelengths to longer wavelengths (Cf. Figure. 2. 10 (a)) and to broad bandwidths (Cf. figure.2.10 (b)).
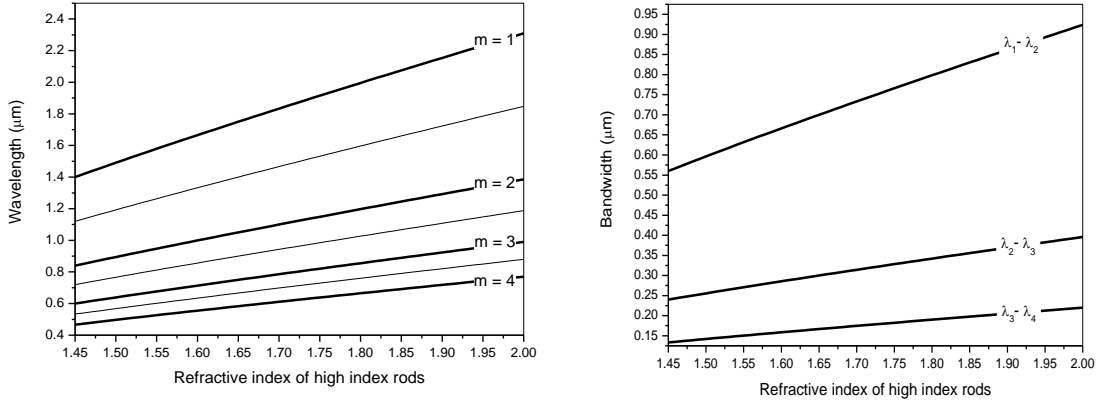
(a)	(b)

Figure 2.10: (a) Evolution of the resonant wavelengths (λ_m) (bold lines) versus the refractive index of high index rods. Thin black lines indicate the centre between two resonant wavelengths. (b) Evolution of interval of two adjacent resonant wavelengths ($\lambda_m - \lambda_{m+1}$) versus the refractive index of the rods. The rod diameter is 1 μm and the refractive index of the background is 1.45.

However, in these cases the central wavelength of each bandgap shifts also to longer wavelength. To study correctly the effect of increasing the refractive index of the rods on the bandgap width, we have to normalize the bandwidth variation versus the central wavelength. As shown in figures 2.11(a-c), the normalized bandwidths are constants. They do not depend on the refractive index of the rods. It is also interesting to notice that the bandwidths are still constant when the refractive index of the ground is modified (n = 1; 1.3; 1.45).
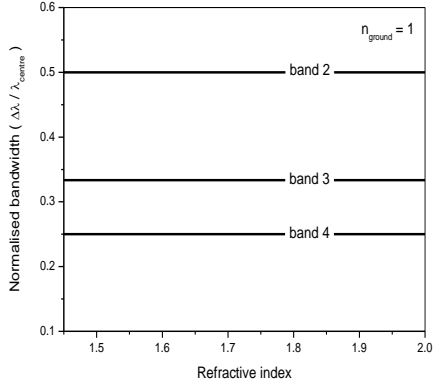
(a)
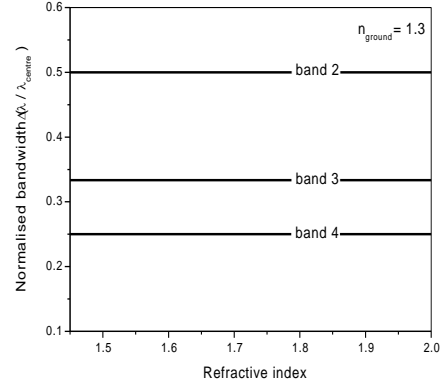
(b)
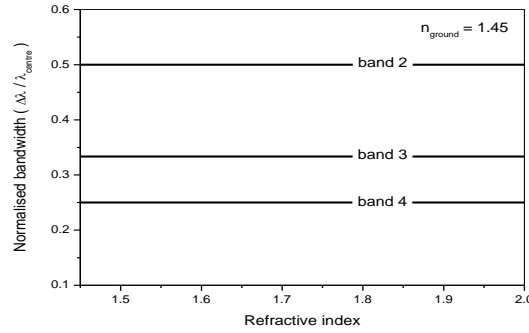
(c)

Figure 2.11: Evolution of the normalized bandwidths ($(\lambda_m - \lambda_{m+1})/\lambda_{center}$) versus the refractive index of the rods. Band 2, band 3 and band 4 correspond to the interval λ_1-λ_2, λ_2-λ_3, λ_3-λ_4, respectively. The refractive index of the ground is set equal to 1 (a), to 1.3 (b) and 1.45 (c). The diameter of the rods is 1 μm.

These results indicate that the bandgap bandwidth is constant and does not depend on the photonic crystal parameters. This can be demonstrated by the following development:

The central wavelength is defined with equation (2-1) as follows:

$$\lambda_c = \frac{\lambda_m + \lambda_{m+1}}{2} \approx \frac{1}{2}(\frac{4d}{2m+1}\sqrt{n_2^2 - n_1^2} + \frac{4d}{2(m+1)+1}\sqrt{n_2^2 - n_1^2})$$

$$\lambda_c = 8d\sqrt{n_2^2 - n_1^2}(\frac{m+1}{4m^2 + 8m + 3}) \qquad (2\text{-}3)$$

Leading to the definition of the normalized bandwidth:

$$\frac{\Delta\lambda_m}{\lambda_c} \approx \frac{\dfrac{8d}{4m^2+8m+3}\sqrt{n_2^2-n_1^2}}{8d\sqrt{n_2^2-n_1^2}\left(\dfrac{m+1}{4m^2+8m+3}\right)}$$

$$\frac{\Delta\lambda_m}{\lambda_c} \approx \frac{1}{m+1} \tag{2-4}$$

This development confirms that the bandwidths of the bandgap depend only on the order of the bandgap (m). The bandgap order is higher, The bandgap bandwidth is narrower. By analogy with the quantification of the bandwidth of a resonator, we can define the Q-factor of the bandgap from the previous relation:

$$Q = \frac{\lambda_c}{\Delta\lambda_m} \approx m+1 \tag{2-5}$$

It is important to emphasis: that these relations cannot calculate the bandwidth of the first band (fundamental band) that is delimited by the first resonant wavelength (m=1) at the short wavelength side and by the vanishing guiding condition at the long wavelength side. Indeed, there is no cut-off wavelength at the long wavelength side since the first resonant wavelength (m=1) corresponds to the first cut-off wavelength.

From this demonstration, we can conclude that the evolution of the bandgap properties can be expressed versus the normalized frequency of a single rod as follows:

$$V = \frac{\pi d}{\lambda}\sqrt{n_2^2-n_1^2} \tag{2-6}$$

Furthermore, since the refractive index of the ground does not change the normalized bandwidth of the bandgaps, studying the bandgap properties versus the refractive index of the rods can be defined versus the step index $(n_2 - n_1)$ that could be expressed in percent by the ratio $((n_2 - n_1)/n_2)\times100$.

These notations are used in different studies on the SC-PBGFs. For example, Masahiro *et. al.* have studied the effect of increasing the refractive index of the rods on the attenuation coefficient of the fundamental mode [48], see figure below:

<div align="center">(a)   (b)</div>
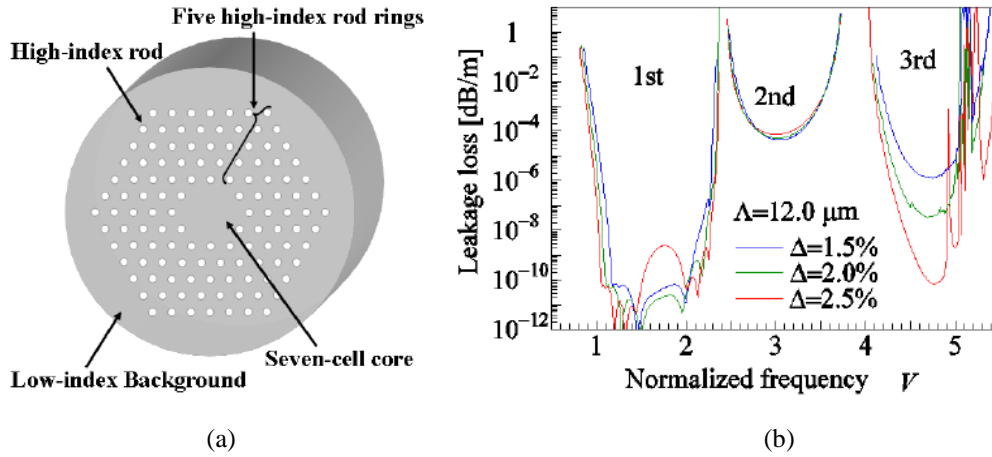
Figure 2.12: (a) cross section view of solid-core photonic bandgap fiber studied. (b) Spectrum in normalized frequency of the attenuation coefficient of the fundamental mode for different step index between the core and the rods. [48]

Therefore, when we conceive an SC-PBGF with a bandgap centered at a specific wavelength, the diameter of the rods must be reduced when the step index is increased. The rod diameter is simply obtained from the definition of the normalized frequency (2-6) for the chosen operating wavelength. From the results shown in figure 2.12(b), we can also conclude that the wider band is the first bandgap, situated between V= 0.7 to 2.405 and centered around V = 1.6. Furthermore, the attenuation coefficient of the fundamental core mode is much lower in this band than in the higher order ones. It is noticeable that for a given pitch, the ratio "core diameter over wavelength" increases for higher V. In other words, in higher order bandgaps the wavelengths of the propagated fields "see" a larger core than in the first bandgap. But, in common waveguides a larger core leads to lower attenuation. This particularity emphasizes a stronger field confinement in the first bandgap.

In the following, we have, therefore, chosen to focus our study only on the field properties guided in the first bandgap. Only few works have been reported with a good normalization as the work of Masahiro *et. al.* [48], but the studies are limited to moderate step index, up to 2.5 %. In the following study, we consider a higher refractive index variation (up to 6.89 %) and also study for the first time (to the best of our knowledge) the influence of material absorption on the SC-PBGF properties.

In order to make this study easily exploitable for fiber conceptions, we have chosen to plot the results versus the wavelength. We have thus adapted the rod diameter to the step index variation in order to keep the central wavelength of the bandgap constant. The rod diameter used versus the step index is written in the following table:

Δn	0.02	0.04	0.06	0.08	0.10	0.12	0.14	0.16	0.18	0.20
d (µm)	2.044	1.440	1.172	1.012	0.902	0.820	0.757	0.706	0.663	0.627

Table 2.1: Values of rod diameters depending on the step index for keeping the central wavelength of the first bandgap around 1 µm.

These diameters are calculated for a bandgap (first one) centered around 1 µm (V = 1.552). The SC-PBGF studied is composed of 5 rings of rods embedded in a silica ground and the ratio d/pitch is kept equal to 0.128. We have used the CUDOS MOF utilities software based on the multipole method [49, 50] to calculate the properties of the fundamental core mode of SC-PBGFs with different step-index ranging from 0.02 to 0.1 for a silica ground (from 1.38 % to 6.89 %).

II.2.2. Attenuation coefficient of the fundamental core mode

The evolutions of the spectrum of the attenuation coefficient of the fundamental mode are plotted in figure 2.13, below.

(a)   (b)
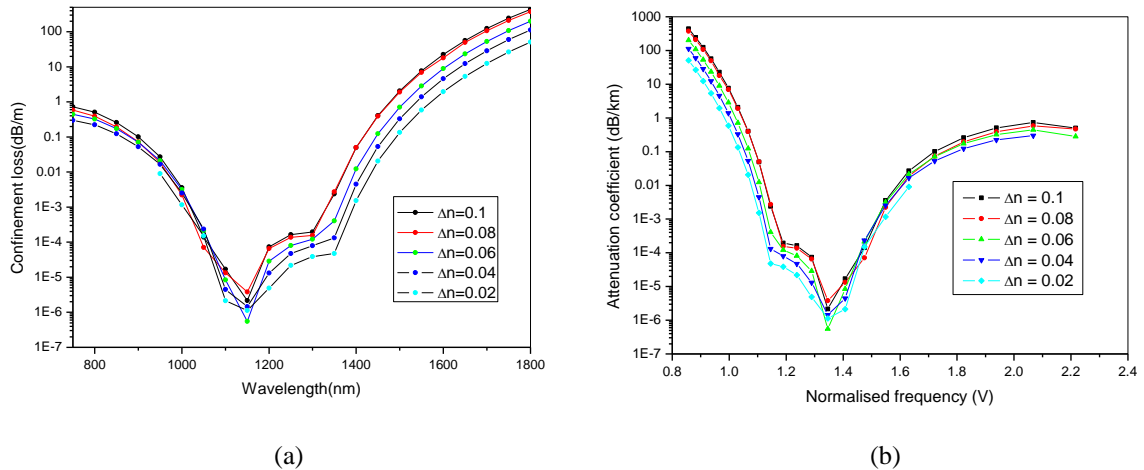
Figure 2.13: Attenuation coefficient of the fundamental core mode for different step-index versus the wavelength (a), versus the normalized frequency (b)

From these results we can conclude that adapting the rod diameter to the index difference keeps the central wavelength and the edges of the bandgap at constant wavelengths. The validity of this normalization is confirmed by plotting these results versus the normalized frequency (Cf. figure 2.13(b)).

It is interesting to notice that increasing the step-index do not decrease the attenuation coefficient but increases it in the longer wavelength region. This behavior is not fully understood but it has been partially explained by the apparition of Fano resonance effect [51] generated by field diffraction around each rod. This effect induces the particular shape of these curves in the bandgap center.

II.2.3. Chromatic Dispersion of the fundamental core mode

In this part, we study of effect of the step-index on the chromatic dispersion of the fundamental core mode within the fundamental bandgap. The chromatic dispersion of a mode is defined by the following relation:

$$D_c = -\frac{\lambda}{c}\frac{\partial^2 n_{eff}}{\partial \lambda^2}$$

with n_{eff} is the effective index of guided mode.

To obtain the chromatic dispersion we have calculated the effective index of five SC-PBGFs with different index difference and then have used a polynomial function with five orders to fit each effective index curves. This polynomial function is then two times derivated and finally the chromatic dispersion curves are obtained and plotted in the following figure 2.14.

From these results we can conclude that the variation of the step-index has a strong effect on the chromatic dispersion, since higher step-index induces a shift of the zero dispersion wavelength to shorter wavelengths. A variation of the step-index from 0.02 to 0.1 shifts the zero dispersion wavelength from 1230 nm (zero dispersion of the silica) down to 1100 nm, as shown in figure 2.15. Therefore, increasing the step-index enables to compensate the chromatic dispersion of the background material, here the silica. These results highlight the great interest of studying SC-PBGF with large index difference.
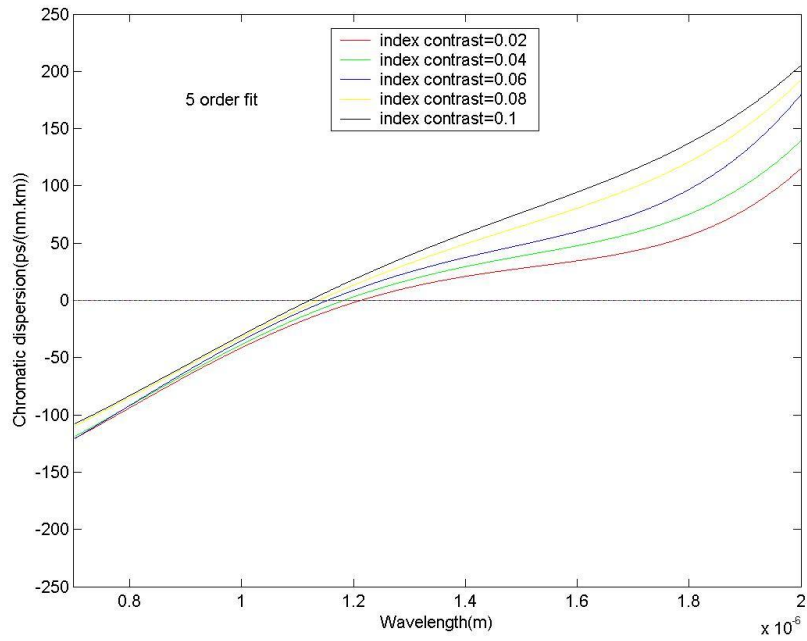
Figure 2.14: Chromatic dispersion curve of the fundamental core mode of a SC-PBGF
with different step-index from 0.02 to 0.1.
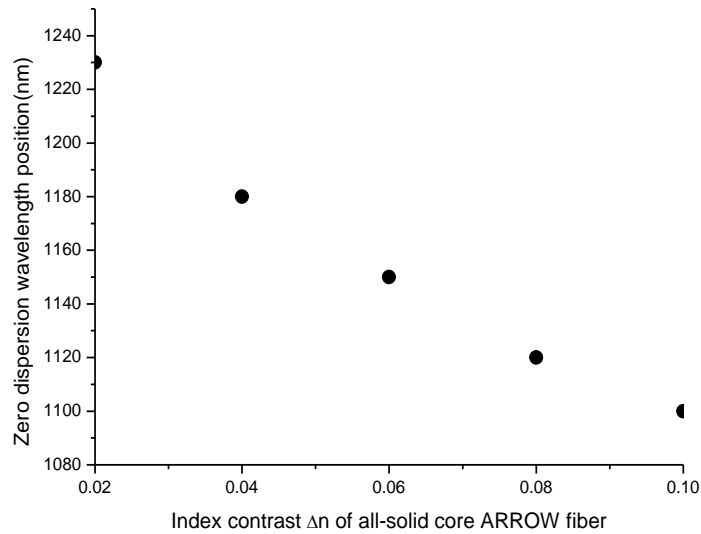
Figure 2.15:   Evolution of the zero dispersion wavelength (of the fundamental core mode)
versus the step-index of a SC-PBGF.

II.2.4.   Effective area of the fundamental core mode

In this section, we study the evolution of the effective area of the fundamental core mode for different step-index. The effective area of a mode is defined as follow:

$$A_{eff} = \frac{\left(\iint |F(x,y)|^2 \right)\ dx\ dy}{\iint |F(x,y)|^4\ dx\ dy}$$

(2-10)

With F(x,y) the distribution function of the mode. A_{eff} depends on the diameter of fiber core and index difference of fiber core and cladding.

The evolution of the effective area of the fundamental core mode versus the refractive index of the rods is computed, at the wavelength of 1000 nm (bandgap center) for SC-PBGF with different core size: 1 cell, 7 cells and 19 cells. The core size is defined by the number of removed rods during the fiber stacking, i.e, the number of rod defects in the center. In this study, we have considered a SC-PBGF with 1 defect, 7 defects and 19 defects. The intensity maps of the fundamental core mode confined in these cores are illustrated in figure 2.16.

| (a) | (b) | (c) |
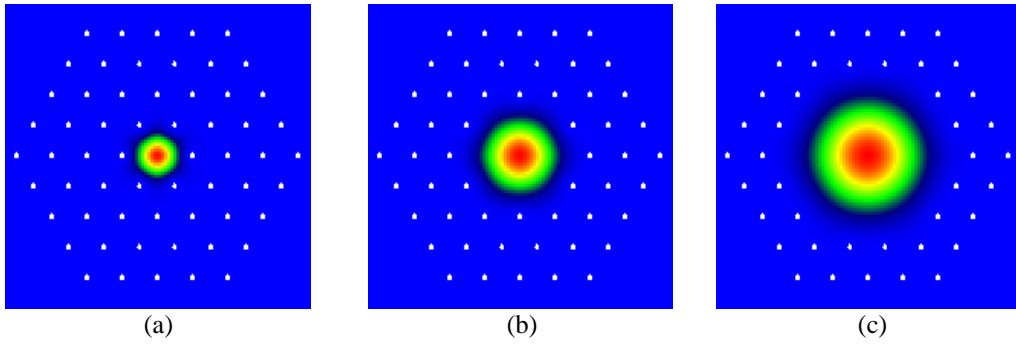
Figure 2.16:   The structure of SC-PBGF with different number of core size (a) 1 defect, (b) 7 defects, (c) 19 defects, and the intensity map of the fundamental core mode.

The evolution of the effective area versus the refractive index of the rods is plotted in figure 2.17 for different core size. As expected, larger core size leads to larger effective area. Furthermore, in all cases, increasing the step-index induces smaller effective area emphasizing a stronger field confinement within the fiber core. This behavior might influence the bend sensitivity of the fundamental core mode of the SC-PBGF. This is studied in the following section.
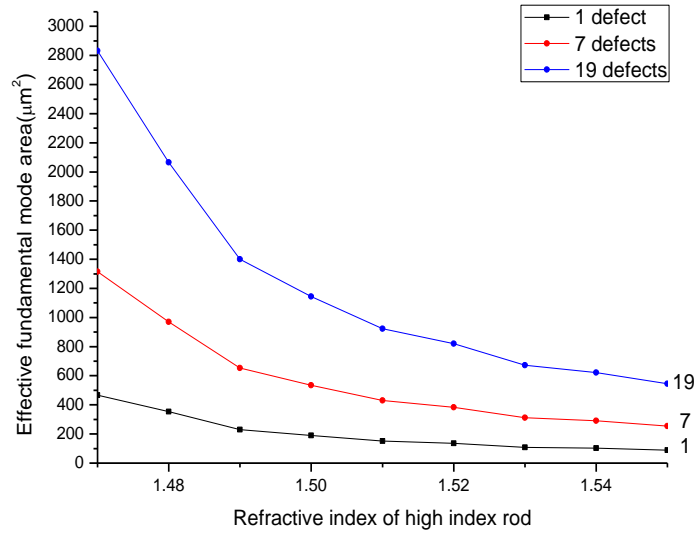
Figure 2.17: Effective mode area of the fundament core mode of a SC-PBGF with different core size, versus the refractive index of the rods.

II.2.5. Sensitivity of the fundamental core mode to bends

The loss sensitivity of guided mode to bends is a critical parameter for numerous applications of optical fiber. In the case of SC-PBGF, T. A. Birk has developed an approximate relation of the critical bend radius [23]:

$$R_c \approx \frac{4\pi\lambda n_{BG}^2}{\left|n_{fm}^2 - n_{edge}^2\right|^{\frac{3}{2}}}$$

with n_{BG} the refractive index of background (here silica), n_{fm} the effective index of fundamental mode and n_{edge} the effective index of the nearest band edge (cladding mode) to the core line. By this critical bend radius, we have calculated the critical bend radius of a SC-PBGF for different step-index, over the spectrum of the fundamental bandgap. These results are presented in figure 2.18:
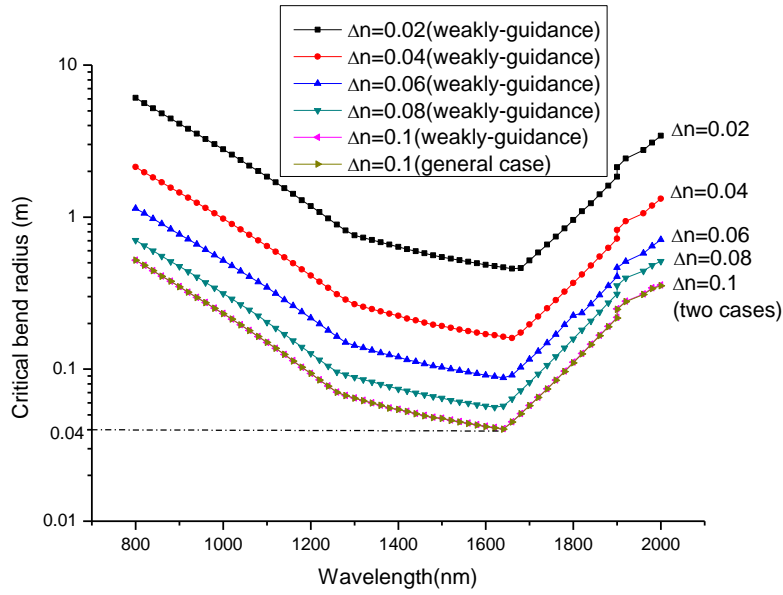
*Figure 2.18:   Evolution of the critical bend radius versus the wavelength for a SC-PBGF
with different step-index.*

From these results we can conclude that higher step-index leads to lower critical bend radius. A critical radius as low as 5 cm is obtained for the larger step-index.

However, the relation developed by T. A. Birks is limited to small step-index SC-PBGF. In order to check it validity to our study, we can develop a relation of the critical bend radius from J. D. Love's paper on a standard step-index fiber [52]:

The beating length between the fundamental field and radiated field in the cladding is defined:

$$z_c = 2\pi / (\beta - kn_{cl})$$

With $\beta = k\, n_{fm}$ the propagation constant of the fundamental mode, and n_{cl} the refractive index of the cladding, then the propagation constant of the radiation is kn_{cl}. When loss are not too large, the critical radius is defined by:

$$R_b \geq \frac{W}{\rho} \frac{z_c^2}{2}$$

with $W = \rho(k^2 n_{cl}^2 - \beta^2)^{1/2}$ and ρ the core radius.

By substituting the previous equations we get:
$$R_b \geq \frac{2\pi^2 W}{\rho(\beta - kn_{cl})^2}$$

In his development, T. A. Birk proposed to replace n_{cl} by the effective index (n_{edge}) of the nearest band edge to the fundamental core mode. So if we follow the same idea the above equation becomes:

$$R_b \geq \frac{2\pi^2 W}{\rho(\beta - kn_{edge})^2}$$

By substituting W in the above equation, we finally get:

$$R_b \geq \frac{2\pi^2 \rho k (n_{edge}^2 - n_{fm}^2)^{\frac{1}{2}}}{\rho k^2 (n_{fm} - n_{edge})^2} = \frac{2\pi^2 (n_{edge}^2 - n_{fm}^2)^{\frac{1}{2}}}{k(n_{fm} - n_{edge})^2} = \frac{\pi\lambda (n_{edge}^2 - n_{fm}^2)^{\frac{1}{2}}}{(n_{fm} - n_{edge})^2} = \frac{\pi\lambda \left| n_{edge}^2 - n_{fm}^2 \right|^{\frac{1}{2}}}{(n_{fm} - n_{edge})^2}$$

We have calculated the critical bend radius with this equation for the index difference of 0.1 and plot the results in figure 2.18, curve in olive. This curve fits the one obtained from T. A. Birk's relation indicating that our previous calculation were correct within this range of step-index.

II.2.6.   Higher order core modes

In this section, we study the effect of larger step-index on the higher-order core modes. We compare the effective index of the first 6 modes of a SC-PBGF: two degenerate HE_{11} modes (fundamental modes), TE_{01} mode, TM_{01} mode and two degenerate HE_{21} modes, with different step-index. The simulation is realized at the wavelength of 1000 nm and SC-PBGF with different core sizes are considered. The results are plotted in figure 2.19 for SC-PBGF with a core size of 1 defect, 7 defects and 19 defects. In all cases, larger step-index lead to larger difference between the effective index of the fundamental mode and the first fourth higher order modes (TE_{01}, TM_{01} and Two degenerate HE_{21} modes). These results indicate that it might be easier to obtain single mode transmission even if the fiber is multimode, since large index difference makes fundamental mode power difficult to couple to high order modes.
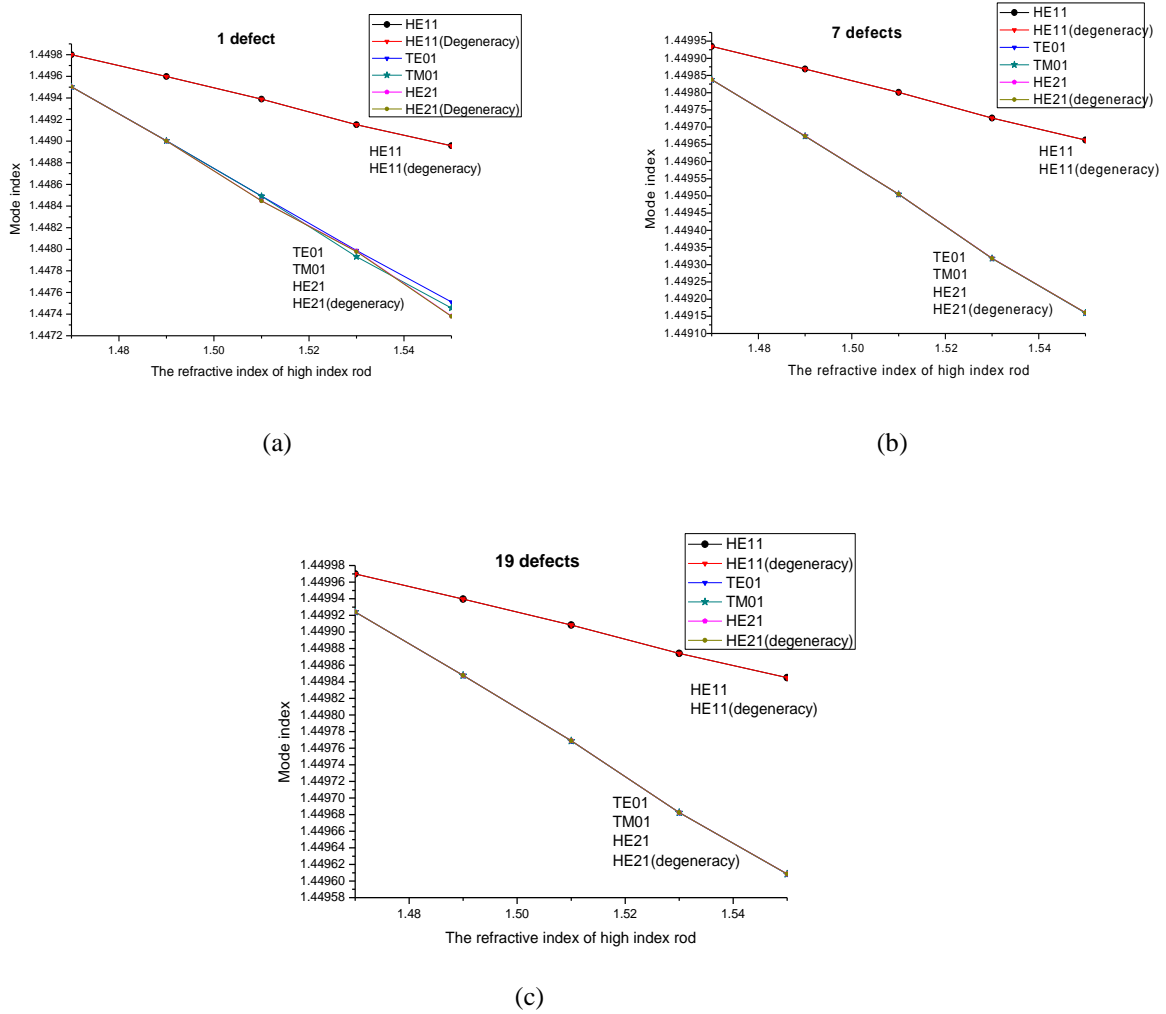
Figure 2.19: Evolution of the effective index of the first six core modes versus the step-index of a SC-PBGF with a core size of 1 defect (a), 7 defects (b) and 19 defects (c).

II.3. Conception and fabrication of solid-core photonic bandgap fiber with high-index rods

In this section, we detail the conception of an SC-PBGF based on realistic materials by taking into account the effect of the material absorption coefficient on the fiber properties. Indeed, materials with higher refractive index than silica's one have much larger absorption coefficient. This study seems original to the best of our knowledge. This study is motivated by the fact that the powder-in-tube method developed at XLIM enables us to potentially fabricate SC-PBGF with a larger step-index than most of the SC-PBGF studied. Indeed, this method is well adapted for fabricating multi-glass fiber with quite different properties. Among the different composition of multi-glass fiber fabricated, the Lanthano Alumino Silicate glass (in French: Silice Alumine Lanthane (SAL)) is particularly interesting since it is

relatively "easy" to use as core material in silica fiber and it can present a high refractive index (compared to silica one) depending on its composition. In the following study, we focus our efforts on optimizing the conception of an SC-PBGF based on that glass, and then present the preliminary fabrication results of a SC-PBGF composed of SAL and silica.

II.3.1. Presentation of the properties of Lanthano Alumino Silicate glass

To overcome the large loss problem in visible or near infrared wavelength region of the above high index glass, a kind of glass which has relative larger index difference than silica and relative low loss in visible and near infrared wavelength region at the same time is one aim which researchers pursue. The SAL material (highly doped Al_2O_3 and La_2O_3 in the SiO_2 glass) is a good material to satisfy above the two requirements. For example, when SAL material composition is 70 mol% of SiO_2, 20 mol% of Al_2O_3 and 10 mol% of La_2O_3, the refractive index of SAL material is 0.1 higher than silica glass. Furthermore, the mixture of SiO_2, Al_2O_3 and La_2O_3 has not strong absorption in the visible and near infrared wavelength regions.

The institute of photonic technology in Jena (Germany) and our research group have done some foundational and application works on SAL fibers [53-56]. Some challenges are met during drawing SAL fibers, because the transition temperature (T_g) and expansion coefficient of SAL material do not match with that of silica. The T_g of silica glass is 300 $^{\circ}$C higher than the one of SAL glass [56], and the expansion coefficient of silica is almost 10 times smaller than the SAL one; 0.5×10^{-6} K^{-1} for silica glass and 4.3-7.0×10^{-6} K^{-1} for SAL glass [56]. These mismatches will increase fiber losses. For partly overcoming the influence of these mismatches, some improved methods are proposed: For example, the silica glass cladding with high cladding-core-ratio is used to reduce the influence of expansion coefficient mismatch [53] and low speed drawing (7 m/min) can significantly reduce fiber loss. The influence of the drawing speed on the attenuation coefficient is illustrated in figure 2.20 from [56].
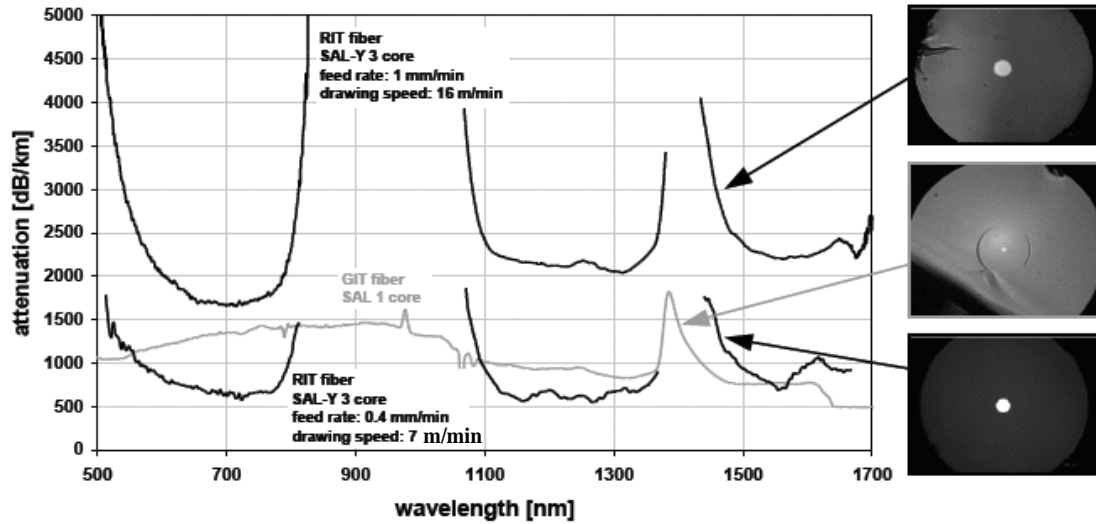
Figure 2.20: Attenuation spectrum of fibers composed of a silica cladding and a core of SAL doped with Ytterbium, drawn at different drawing speeds and preform feed rates by the rod-in-tube method (black curves). Attenuation spectrum of a fiber composed of SAL (only) core and silica cladding fabricated with the powder-in-tube method (gray curve). Photograph of the cross section of each fiber is shown on the right.

This slow speed drawing method can partly overcome the mismatch of glass transition temperature (T_g), because slow speed drawing can reduce the breaking possibility of core material. In the chapter 3, we will give the more details explanation about slow speed drawing method for the drawing of fiber whose core and cladding materials have different glass transition temperatures (Tg).

Nevertheless, even if the attenuation coefficient could be reduced by decreasing the drawing speed, the SAL glass has an attenuation coefficient around 1 dB/m (Cf. curve gray in Figure. 2.20) that has to be considered during the conception stage of the SC-PBGFs.

II.3.2. Conception of a solid-core photonic bandgap fiber based on Lanthano Alumino Silicate and silica glasses

In this section, we optimize the conception of a SC-PBGF composed of ground of a silica and high-index inclusions of SAL glass. The fiber is optimized for an operating wavelength at 1064 nm. This wavelength is interesting because this is the emitting wavelength of common and widely used Nd:YAG lasers. Nevertheless, main optimization results of the SC-PBGF properties could be easily applied to other wavelength ranges by simply changing the

diameter of the rods (with a constant d/pitch) because the bandgap properties depend on that parameter. Experimentally, the shift of the bandgap is simply realized by changing the outer diameter of the fiber during its fabrication.

In the following, we consider a SAL glass with a refractive index 0.1 higher than the silica one and with a constant attenuation coefficient of 1 dB/m.

Position of the fundamental bandgap

From the previous study, we get the rod diameters equal to 0.9 µm for a step-index of 0.1 and the fundamental bandgap centered around 1 µm. We have computed, with a program working with COMSOL software (based on Finite Element Method [57, 58]), the modes of a SC-PBGF composed of three rings of these rods spaced by $\Lambda = 7$ µm. The dispersion diagram of these modes is plotted in figure 2.21. As expected, the fundamental bandgap is centered around 1 µm and it is delimited by bands of cladding modes corresponding to a combination of coupled LP_{01} modes and LP_{11} modes for the band at long wavelengths and short wavelengths, respectively.
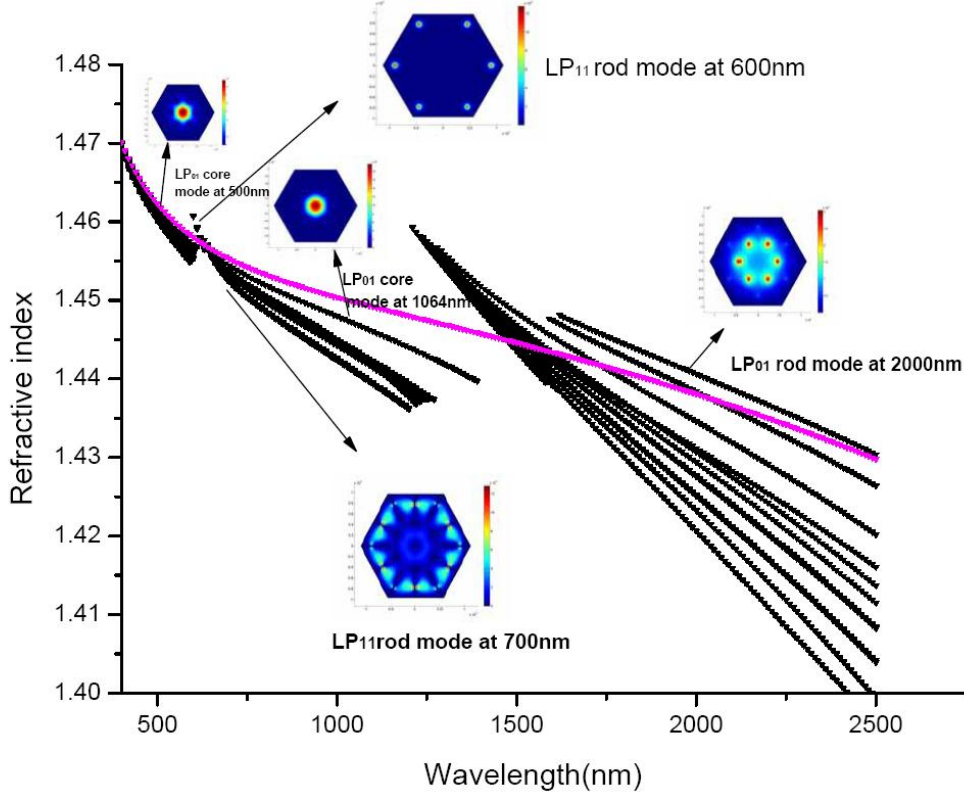
Figure 2.21: Dispersion diagram of the effective indexes of modes supported by a SC-PBGF composed of three rings of SAL rods (d = 0.9 µm, Δn = 0.1) embedded in silica with a pitch of 7 µm. The pink curve indicates the refractive index curve of silica.

Topology optimization with material considered:

In this section, we study the effect of the material absorption of the rods on the properties of the fundamental mode confined within the fundamental bandgap of a SC-PBGF. As noticed previously, we consider a SAL material absorption coefficient of 1dB/m, by the relation equation that links the imaginary part of refractive index and absorption coefficient [46], we can calculate the imaginary part of refractive index of SAL material at 1064 nm:

$$\text{Im}(n_{\text{SAL}}) = \frac{1 \times \ln(10) \times 1.064}{20 \times 2\pi \times 10^6} = 1.95e - 8 \,,$$

Then, we have computed the attenuation coefficient, versus the pitch of the photonic crystal, for a SC-PBGF composed of rod diameter of 0.9 µm with different number of rod layers. These results are plotted on the following figure:
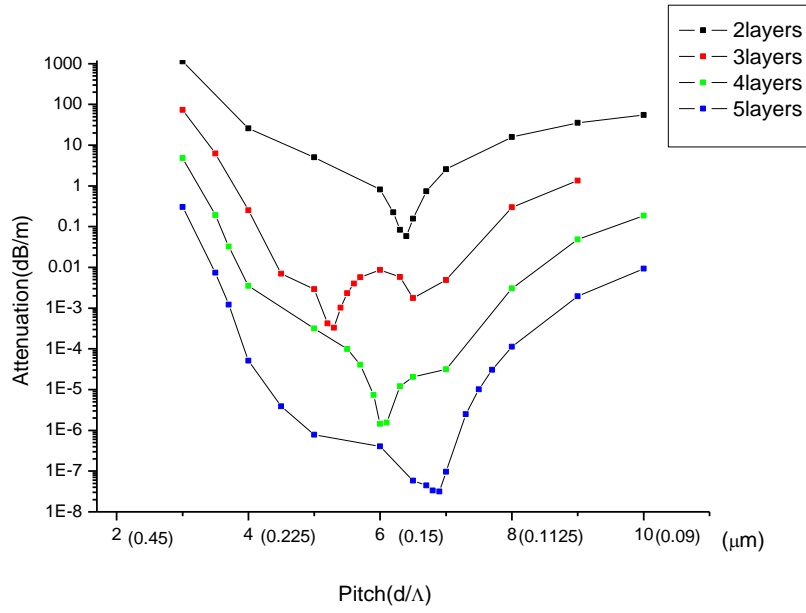
Figure. 2.22: Attenuation coefficient, at 1064 nm, versus the pitch for a SC-PGF composed of rods with a material absorption of 1 dB/m (d = 0.9 µm, Δn = 0.1) for different number of rod layers.

As expected, the attenuation coefficient decreases with the number of rod layers. It is noticeable that all curves tend to a minima for a pitch around 5−7 µm. These could be explained by an optimized compromise between attenuation from material absorption of the rods and attenuation from weak confinement. It is also important to emphasis that even with two layers of rods, it is possible to confine the field with an attenuation coefficient 10 times lower than the material absorption of the rods. Furthermore, an attenuation coefficient as low as 10^{-7} dB/m is obtained with five layer of rods and a pitch of 7 µm. **This result demonstrates the possibility to use rod material with moderate absorption (around 1dB/m) coefficient for fabricating SC-PBGF**.

To investigate further this demonstration, we have computed the attenuation coefficient for five layers of rods without material absorption, with a material absorption of 1 dB/m and 5 dB/m. These results are shown in figure 2.23. All curves are confused, demonstrating that moderate material absorption (until 5 dB/m) in the rods has no obvious effect on the attenuation coefficient of the fundamental core mode.
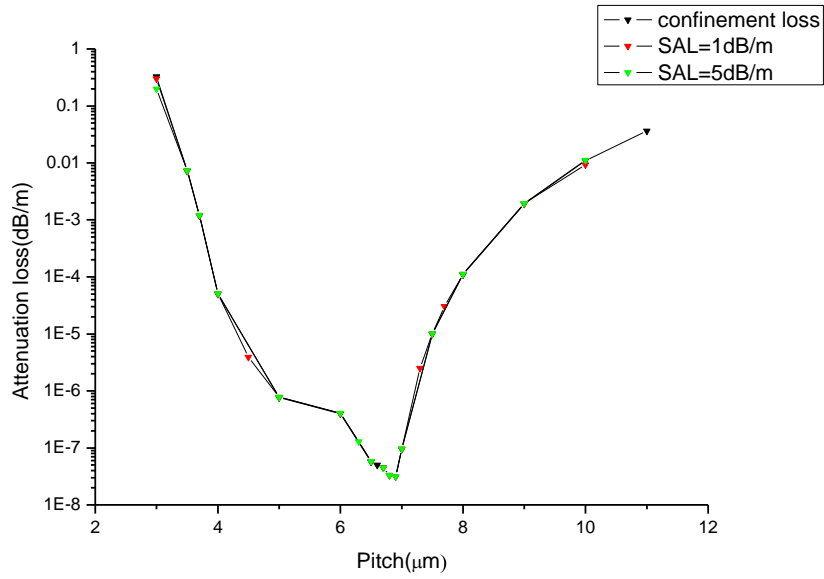
Figure 2.23:   Attenuation coefficent, at 1064 nm, versus the pitch of a SC-PBGF composed of 5 layers of rods without or with a material absorption of 1 dB/m or 5 dB/m (d = 0.9 μm, Δn = 0.1).

Attenuation spectrum of the optimized SAL/silica SC-PBGF

From the results obtained in the previous section, we have calculated the attenuation spectrum of the optimized SAL/silica SC-PBGF.
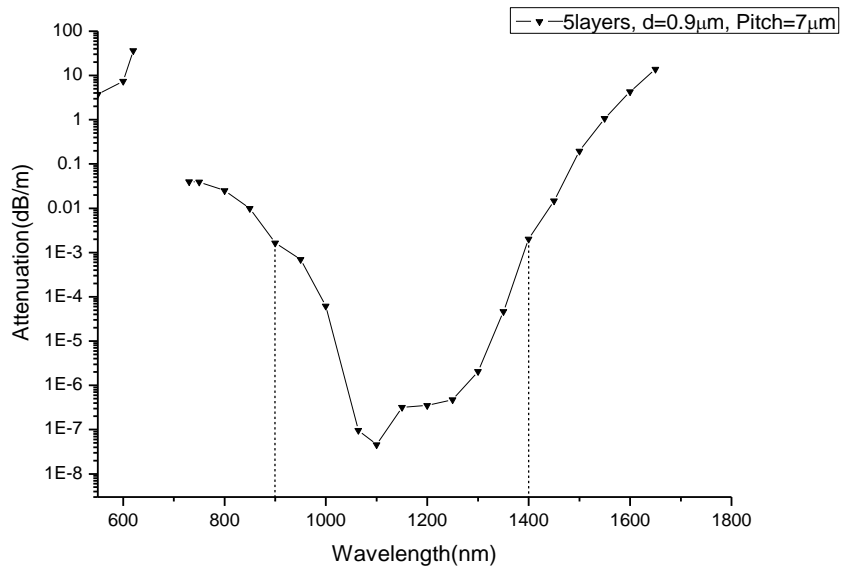
Figure 2.24: Attenuation coefficient versus the wavelength of a SC-PBGF composed of SAL rods with a material absorption of 1 dB/m, a step-index of 0.1 and a diameter of 0.9 μm. The numbers of rod layer is five and the pitch is 7 μm.

From the results shown in figure 2.24, we can conclude that this SC-PBGF has in theory a broad transmission band ranging from 900 nm to 1400 nm with an attenuation coefficient lower than 1 dB/km, with a lowest value around 10^{-7} dB/m at 1100 nm.

In recent publications about the attenuation of SC-PBGFs; Guobin Ren et al proposed a low loss SC-PBGF with low index difference and a lowest confinement loss of 2×10^{-3} dB/m in the region of near infrared wavelength region [33]. Nicolai Granzow et al realized a chalcogenide-silica SC-PBGF with a large index difference and a lowest attenuation of 10^{-1} dB/m in the region of near infrared wavelength region [36]. Our designed SAL/silica SC-PBGF can potentially realize the lowest loss in the region of near infrared wavelength region.

Chromatic dispersion of the fundamental core mode

We also plot the chromatic dispersion curve of fundamental core mode of our designed SAL/silica SC-PBGF (Cf. Figure. 2.25). Within the bandgap range, the chromatic dispersion is normal from 800 nm to 1100 nm and anormal from 1100 nm to 1700 nm, with a zero dispersion wavelength around 1100 nm.
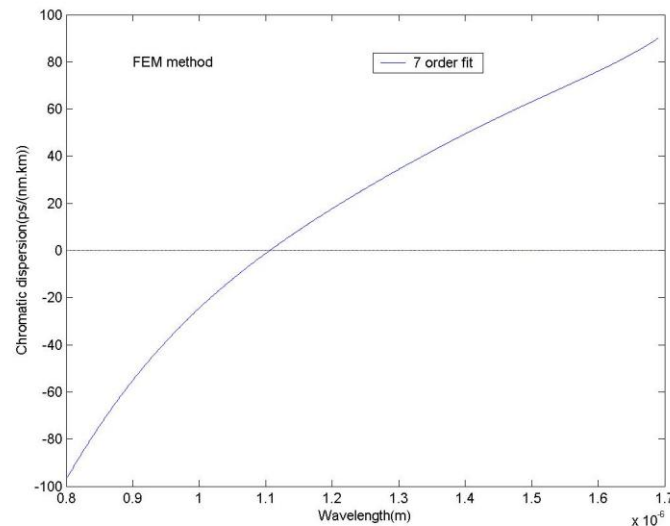
Figure 2.25:   Chromatic dispersion curve of the fundamental core mode of our designed SAL/silica SC-PBGF.

II.3.3 Fabrication of Silica/SAL solid-core photonic bandgap fiber

In this section, we present the preliminary fabrication results of a SAL/silica SC-PBGF. The first objective of this fabrication is to demonstrate the possibility to fabricate an optical

fiber with a 2D arrangement of SAL rods. We did not work on the fabrication process, but we have just used it that served to fabricate the first low-contrast SC-PBGF. This process consists in filling the air-holes of a silica preform of a solid-core PCF with doped fibers to form the high-index inclusions. The fabrication process could be decomposed in three steps: (1) the fabrication of a fiber with high refractive index, (2) the fabrication of a silica preform with a silica core, and (3) the fabrication of the SC-PBGF.

(1) Fabrication of a fiber with high refractive index

To fabricate the fiber that will make the high-index inclusion, we have fabricated a fiber composed of a SAL core and silica cladding. We have first fabricated the SAL composed of 70 mol% of SiO_2, 20 mol% of Al_2O_3, and 10 mol% of La_2O_3. The pieces of bulk glass were then transformed to powder. Finally, we have fabricate the SAL core fiber by the powder-in-tube method: we put the SAL powder into silica glass tube, and then put them in furnace to heat them in 1100˚C for 1 hour (sintering of SAL powder for removing air bubble). After this treatment, we draw the silica glass tube with SAL powder to get SAL core fiber with an outside diameter of 150 µm and a core diameter of 24 µm.

(2) Fabrication of a silica preform with a silica core

The conception of the silica preform with a silica core is very important since it will determine the pitch of the SC-PBGF. Indeed, the topology of the photonic crystal corresponds to the one of the preform before the homothetic (almost) reduction during the fiber drawing stage. To obtain the targeted parameters (d = 0.9 µm, pitch = 7 µm and outer diameter around 120 µm) we have fabricated with the stack-and-draw process a preform with the following parameters:

- pitch = 245 µm
- diameter of air-hole = 187 µm leading to d/pitch = 0.76
- outer diameter = 3 mm

A photograph of a cross section of a fabricated preform is shown on the figure below:
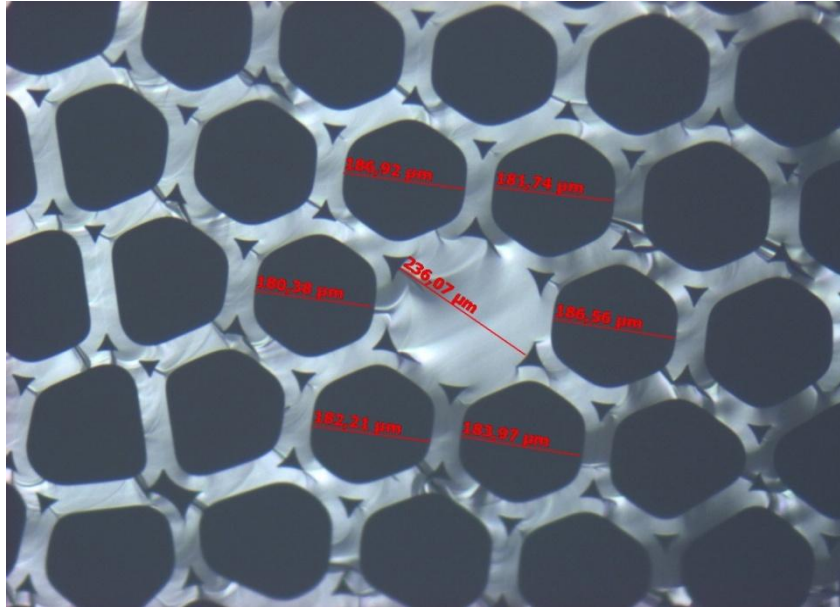
Figure 2.26: Photographs of the cross section of a fabricated preform
to be filled with SAL core fiber for making a SC-PBGF.

(3) Fabrication of the SC-PBGF

To fabricate the SC-PBGF, we have filled three rings of air-hole of the fabricated preform with the fabricated SAL core fiber. The preform was filled along 1 m. Sample of SAL core fiber of 1 m long length have been cut and the polymer coating was removed with chemical product. Then, the preform was filled within a jacket tube with 3 mm inner diameter and 4 mm outside diameter. The structure was drawn down to a fiber with an external diameter of 120 µm. A photograph of the fiber cross section is shown in figure 2.27. The fiber exhibits a 2D pattern of three layers of high-index rods. The rod diameter is around 2 µm and the pitch around 7.5 µm. This preliminary demonstrates the potential of the powder-in-tube method for fabricating special fiber, such as SC-PBGF based on multi-material glasses. Comparing with our designed fiber size (d=0.9 µm, pitch=7 µm), we can see that the size of fiber has still a little difference with designed structure size. These differences could be improved by reducing the gap between the diameter of the SAL core fiber and the air-hole diameter of the preform. Indeed, we conceive a large gap of 30 µm in order to fill easily the preform with the SAL core fiber. This gap could be reduced or suppressed with an improved fabrication process.
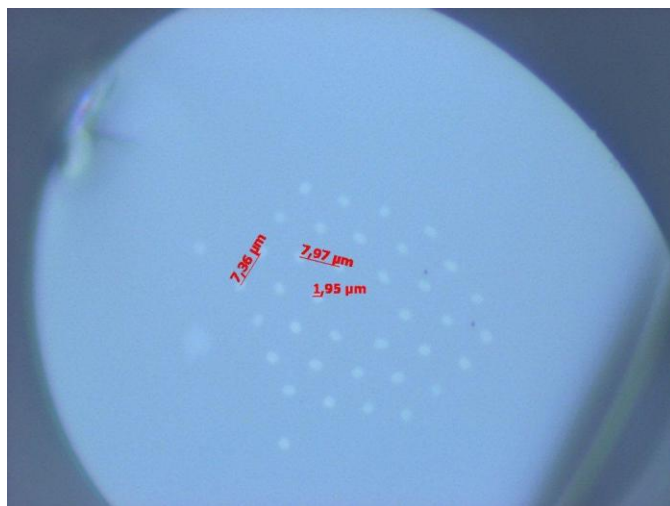
Figure 2.27: Photograph of the cross section of first fabricated SAL/silica SC-PBGF.

We are going to measure the optical properties of that fiber, such as the position of the bandgap and the attenuation coefficient.

In future, we will continue to improve the drawing process to get the required SAL\silica SC-PBGF, and then we will realize deeper optical characterization as the measure of the chromatic dispersion of the fundamental core mode and its bend loss sensitivity.

II.4. Conclusion

In this chapter, we firstly study the effect of increased index different on the properties of solid core photonic bandgap fiber. When the center position of the first bandgap is fixed to 1064nm, and ratio d/pitch is fixed 0.9/7. Comparing to the low index difference solid core ARROW bandgap fiber, the higher index difference solid core ARROW bandgap fiber has: (1) bandgap width and frequency width are invariable. (2) the larger index difference between the first order mode (Two degenerate HE_{11} modes) and the second order mode (TE_{01}, TM_{01} and Two degenerate HE_{21} modes) in the case of 1 defect, 7 defects and 19 defects, namely easier to keep single mode transmission since large index difference makes fundamental mode power difficult to couple to high order mode.(3) smaller effective fundamental mode area(and this also means that the higher index contrast all-solid ARROW bandgap fiber has higher nonlinear coefficient). (4) The higher confinement loss. (5) The smaller critical bend radius (this means that higher index contrast SC-PBGF has lower sensitivity of fiber's bend loss). And then we fabricated one kind of highly doped heavy metal oxide silica glass fiber (we call it SAL fiber: 70mol%SiO_2, 20mol%Al_2O_3, and 10mol% La_2O). Farther, we designed and fabricated one low loss SC-PBGF based on SAL fiber (SAL material is the material of high

index rod in such SC-PBGF). By the structure design of SC-PBGF, the center position of its first bandgap is fixed at 1064 nm. And we also theoretically calculated the critical bend radius (for bend loss) curve and the dispersion curve of fundamental mode of such SC-PBGF. Finally, we fabricated the preform of such solid core bandgap fiber through inserting SAL core fiber without coating into the cane of one photonic crystal fiber fabricated by stack-and-draw method, and drew it to solid core bandgap fiber.

Reference

[1] J.C. Knight, T.A. Birks, P.St.J. Russell, et al. "All-silica single-mode optical fiber with photonic crystal cladding", Optics Letters, 1996, Vol.21, No.19, p1547-p1549.

[2] T.A. Birks, J.C. Knight and P.St.J. Russell. "Endlessly Single-Mode Photonic Crystal Fiber. Optics Letters", 1997, Vol. 22, No.13, p961-p963.

[3] T. P. Hansen, J. Broeng, S. E. B. Libori, et al, "Highly Birefringent Index-Guiding Photonic Crystal Fibers", IEEE Photonics Technology Letters, 2001, Vol.13, No.6, p588-p590

[4] N.G.R. Broderick, T.M. Monro, P.J. Bennett, et. al, "Nonlinearity in holeyoptical fibers: measurement and future opportunities", Optics Letters, 1999, Vol.24, No.20, p1395-p1397.

[5] W.H. Reeves, J.C. Knight, P.St.J.Russell, et.al, "Demonstration of ultra-flattened dispersion in photonic crystal fibers", Optics Express, 2002, Vol.10, No.14, p609-p613.

[6] F.Couny, F. Benabid, P.J. Roberts, M.T. Burnett and S.A. Maier. "Identification of Bloch-modes in hollow-core photonic crystal fiber cladding", Optics Express, 2007, Vol.15, No.2, p325-p338.

[7]F. Benabida, P. J. Robertsa. "Linear and nonlinear optical properties of hollow core photoniccrystal fiber", Journal of Modern Optics, 2011, Vol.58, No.2, p87-p124.

[8] Philip S. Light, François Couny, Ying Ying Wang, Natalie V. Wheeler, P. John Roberts and Fetah Benabid, "Double photonic bandgap hollow-core photonic crystal fiber", Optics Express, 2009, Vol. 17, No. 18, p16238-p16243.

[9] G.S.Wiederhecker, C.M.B. Cordeiro, F. Couny, F.Benabid, S.A.Maier, J.C. Knight, C.H.B. Cruz, H.L.Fragnito, "Field enhancement within an optical fibre with a subwavelength air core", NaturePhotonics, 2007, Vol.1, p115-p118.

[10] Yeh. P, Yariv. A. "Bragg reflection waveguides", Optics Communciation, 1976, Vol.19, Issue.3, p427–p430.

[11] Yeh. P, Yariv. A, Marom. E. "Theory of Bragg fiber", Journal of the Optics Society of American. 1978, Vol.68, No.9, p1196-p1201.

[12] Fink. Y, Winn. J.N, Fan. S, Chen. C, Michel. J, Joannopoulos J.D, Thomas E.L.A, "Dielectric Omnidirectional Reflector ", Science, 1998, Vol.282, p1679–p1682.

[13] Yang, W, Conkey, D.B, Wu, B,Yin, D, Hawkins, A.R, Schmidt, H. Atomic, "spectroscopy on a chip", Nature Photonics, 2007, Vol.1, p331–p335.

[14] T.P. White, R.C. McPhedran, et al. "Resonance and Scattering in Microstructured Optical Fibers", Optics Letters, 2002, Vol.27, No.22, p1977-p1979.

[15] N.M. Litchinitser, S.C. Dunn, B. Usner, B.J. Eggleton, et al. "Resonances in Microstructured optical Waveguides", Optics Express, 2002, Vol.11, No.10, p1243-1251.

[16] N. M. Litchinitser, A.K. Abeeluck, et al. "Antiresonant Reflecting Photonic Crystal Optical Waveguides", Optics Letters, 2002, Vol.27, No.18, p.1592-p1594.

[17] N. M. Litchinitser, S.C. Dunn, P.E. Steinvurzel, B.J. Eggleton, T.P. White, et al. "Application of an ARROW Model for Designing Tunable Photonic Devices", Optics Express, 2004, Vol.12, No.8, p1540-p1550.

[18] P. Steinvurzel, B.T. Kuhlmey, T.P. White, M.J. Steel, C.M. de Sterke, and B.J. Eggleton. "Long Wavelength Anti-Resonant Guidance in High Index Inclusion Microstructured Fibers", Optics Express, 2004, Vol. 12, No.22, p5424-p5433.

[19] P. Steinvurzel, C.M. de Sterke, B.J. Eggleton, B.T. Kuhlmey, et al. "Mode Field Distributions in Solid Core Photonic Bandgap Fibers", Optics Communications, 2006, Vol.263, No.2, p207-p213

[20] P.Steinvurzel, C. Martijn de Sterke, M.J. Steel, B.T. Kuhlmey, and B.J. Eggleton. "Single Scatterer Fano Resonances in Solid Core Photonic Band Gap Fibers", Optics Express, 2006, Vol.14, No.19, p8797-p8811.

[21] G. Renversez, P. Boyer, and A. Sagrini. "Antiresonant Reflecting Optical Waveguide microstructured fibers revisited: a new analysis based on leaky mode coupling", Optics Express, 2006, Vol.14, No.12, p5682-p5687.

[22] M.A. Duguay, Y. Kukubun, T.L. Koch, and L. Pfeiffer. "Antiresonant reflecting optical waveguides in SiO_2-Si multiplayer structures", Applied Physics Letters, 1986, Vol.49, No.1, p13-p15.

[23] T. A. Birks, F. Luan, G. J. Pearce, A. Wang, J. C. Knight, and D. M. Bird, " Bend loss in all-solid bandgap fibres", Optics Express, 2006, Vol.14, No.12, p5688-p5698.

[24] L. Lavoute, P. Roy, A. Desfarges-Berthelemot, V. Kermène, and S. Février, "Design of microstructured single-mode fiber combining large mode area and high rare earth ion concentration", Optics Express, 2006, Vol. 14, No. 7, p2994-p2999.

[25] Sébastien Février, Dmitry D. Gaponov, Philippe Roy, Mikhail E. Likhachev, Sergei L. Semjonov, Mikhail M. Bubnov, Evgeny M. Dianov, Mikhail Yu. Yashkov,Vladimir F. Khopin, Mikhail Yu. Salganskii, and Aleksei N. Guryanov, "High-power photonic-bandgap fiber laser", Optics Letters, 2008, Vol. 33, No. 9,p 989-p991.

[26] L. Jin, Z. Wang, Q. Fang, B. Liu, Y. Liu, G. Kai, X. Dong, and B. O. Guan, "Bragg grating resonances in all-solid bandgap fibers" , Optics Letters.2007, Vol.32, No.18, p2717-p2719.

[27]Long Jin, Zhi Wang, Qiang Fang, Yange Liu, Bo Liu, Guiyun Kai, and Xiaoyi Dong, "Spectral characteristics and bend response of Bragg gratings inscribed in all-solid bandgap", Optics Express 2007, Vol.15 , No.23, p5555-p15565.

[28] Yuhua Li, D.N.Wang, and Long Jin. "Single-mode grating reflection in all-solid photonic bandgap fibers inscribed by use of femtosecond laser pulse irradiation through a phase mask", Optics Letters, 2009, Vol.34, No.8, p1264-p1266.

[29] F. Luan, A. K. George, T. D. Hedley, G. J. Pearce, D. M. Bird, J. C. Knight, and P. St. J. Russell, "All-solid photonic bandgap fiber", Optics Letters, 2004, Vol.29, No.20, p2369-p2371.

[30] A. Argyros, T. A. Birks, S. G. Leon-Saval, C. M. B. Cordeiro, F. Luan, P. St.J. Russell, "Photonic bandgap with an index step of one percent", Optics Express, 2005, Vol.13, No.1, p309-p314.

[31] G. Bouwmans, L. Bigot, Y. Quiquempois, F. Lopez, L. Provino, M. Douay, "Fabrication and characterization of an all-solid 2D photonic bandgap fiber with a low-loss region (< 20 dB/km) around 1550 nm", Optics Express, 2005, Vol.13, No.21, p8452-8459.

[32] A. Bétourné, V. Pureur, G. Bouwmans, Y. Quiquempois, L. Bigot, M. Perrin, M. Douay, "Solid photonic bandgap fiber assisted by an extra air-clad structure for low-loss operation around 1.5 μm", Optics Express, 2007, Vol.15, No.2, p316-p324.

[33] G. Ren, P. Shum, L. Zhang, M. Yan, X. Yu, W. Tong, and J. Luo, "Design of All-Solid Bandgap Fiber With Improved Confinement and Bend Losses", IEEE Photonic Technology Letter, 2006, Vol. 18, No.24, p2560-p2562.

[34] Guobin Ren, Ping Shum, Liren Zhang, and Xia Yu, "Low-loss all-solid photonic bandgap fiber", Optics Letter, 2007, Vol.32, No.9, p1023-p1025.

[35] M. A. Schmidt. N. Granzow, N. Da, M. Peng, L. Wondraczek, and P. St. J. Russell, "All-solid bandgap guiding in tellurite-filled silica photonic crystal fibers", Optics Letters, 2009, Vol.34, No.13, p1946- p1948.

[36] N. Da, L. Wondraczek, M. A. Schmidt, N. Granzow, and P. S. J. Russell, "High index-contrast all-solid photonic crystal fibers by pressure-assisted melt infiltrate on of silica matrices", Journal of Non-Crystal Solids, 2010, Vol.356, p1829-p1836.

[37] Nicolai Granzow, Patrick Uebel, Markus A. Schmidt, Andrey S. Tverjanovich, "Bandgap guidance in hybrid chalcogenide–silica photonic crystal fibers", Optics Letters, 2011, Vol.36, No.13, p2432- p2434.

[38] T. A. Birks, D. M. Bird, T. D. Hedley, J. M. Pottage and P. St.J. Russell, "Scaling laws and vector effects in bandgapguiding fibres", Optics Express, 2004,Vol.12, No.1, P69-p74.

[39] A. Argyros, T. A. Birks, S. G. Leon-Saval, C. M. B. Cordeiro, P. St.J. Russell, "Guidance properties of low-contrast photonic bandgap fibres", Optics Express, 2005, Vol.13, No.7, p2503-p2511.

[40] N.M. Litchinitser, E. Poliakov, "Antiresonant guiding microstructured optical fibers for sensing applications", Applied physics B, 2005,Vol.81, p347-p351.

[41] V. Pureur, A. Bétourné, G. Bouwmans, L. Bigot, A. Kudlinski, K. Delplace, A. LeRouge, Y. Quiquempois, M. Douay, Fiber and Integrated Optics, 2009, Vol. 28, p27-p50.

[42] V. Pureur and J. M. Dudley, "Design of solid core photonic bandgap fibers for visible supercontinuum generation", Optics Communciation, 2011, Vol. 284, p1661–p1668.

[43] Vincent Pureur and Boris T. Kuhlmey, "Higher-order core-guided modes in two-dimensional Photonic bandgap fibers", Journal of Optics. Society of America B, 2002, Vol. 29, No. 7, p1750 -p1765.

[44] A. Isomäki and O. G. Okhotnikov, "All-fiber ytterbium soliton mode-locked laser with dispersion control by solid-core photonic bandgap fiber", Optics Express, 2006 ,Vol. 14, No. 10, p4368 -p4373.

[45] Jesper Riishede, Jesper Lægsgaard, Jes Broeng and Anders Bjarklev,"All-silica photonic bandgap fibre with zero dispersion and a large mode area at 730 nm", Journal of Optics A: Pure and Applied Optics, 2004, Vol. 6, p667–p670.

[46] Chunshu Zhang, Guiyun Kai, Zhi Wang, Tingting Sun, Chao Wang, Yange Liu, Jianfei Liu, Weigang Zhang, Shuzhong Yuan, and Xiaoyi Dong, "Design of tunable bandgap guidance in high-index filled microstructure fibers", Journal of Optical Society of America B, 2006, Vol. 23, No. 4.

[47] N. Litchinitser, S. Dunn, P. Steinvurzel, B. Eggleton, T. White, R. McPhedran, and C. de Sterke, "Application of an ARROW model for designing tunable photonic devices," Optics Express, vol. 12, No. 8, pp. 1540–1550, 2004.

[48] Masahiro Kashiwagi, Kunimasa Saitoh, Katsuhiro Takenaga, Shoji Tanigawa, Shoichiro Matsuo, and Munehisa Fujimaki, "Effectively single-mode all-solid photonic bandgap fiber with large effective area and low bending loss for compact high-power all-fiber lasers", Optics Express, 2012, Vol.20, No.14, p15061-p15070.

[49]T.P.White, B.T. Kuhlmey, et al. "Multipole Method for Microstructured Optical Fibers. I.Formulation", Journal of the Optical Society of America B, 2002, Vol.19, No.10, p2322-p2330.

[50]B.T.Kuhlmey, T.P. White, et al. "Multipole Method for Microstructured Optical Fibers. II.Implementation and Results", Journal of the Optical Society of America B. 2002, Vol.19, No.10, p2331-2340.

[51] P. Steinvurzel, C. Martijn de Sterke, M.J. Steel, B.T. Kuhlmey, B.J. Eggleton, "Single scatterer Fano resonances in solid core photonic band gap fibers", Optics Express, 2006, Vol.14, p8797–p8811.

[52]J.D. Love, "Application of a low-loss criterion to optical waveguide and devices." IEE Preceedings, 1989, Vol.136, No.4, p225-p228.

[53] J.kobelke, Kschuster, S.Grimm, D.Litzkendorf, J.Kirchhof, A.Schwuchow, H.Bartelt, A.Gebhardt. "Multicompent glass microstructured fibers for nonlinear applications", Proceeding of SPIE, 2008, Vol.6990, p699005.

[54] J.kobelke, K.Schuster, D.Litzkendorf, A.Schwuchow, H.Bartelt, V.Tombelaine, P.Leproux, V.couderc, A.Labruyere. "Microstructure fibers with high lanthanum oxide glass core for nonlinear application", Proceeding of SPIE, 2009, Vol.7357, p735702.

[55] Vincent Tombelaine, Alexis Labruyère, Jens Kobelke, Kay Schuster, Volker Reichel, Leproux, Vincent Couderc, Raphaël Jamier, Hartmut Bartelt. "Nonlinear photonic crystal fiber with a structured multi-component glass core for fourwave mixing and supercontinuum generation", Optics Express, 2009, Vol.17, No.18, p15392-p15401.

[56] K.Schuster, J.kobelke, D.Litzkendorf, A.Schwuchow, F.lindner, J.kirchhof, and H.Bartelt, J.-L.Auguste, G.Humbert, and J.-M.Blondy. "Structured material combined HMO-silica fibers: preparation, optical and mechanical behavior", Proceeding of SPIE, 2011, Vol.7934, p793400.

[57] M. Koshiba. "Full-Vector Analysis of Photonic Crystal Fibers Using the Finite Element Method", IEICE Transactions on Electronics, 2002, E85C: p881-p888.

[58] A. Cucinotta, S. Selleri, et al. "Holey Fiber Analysis through the Finite-Element Method", IEEE Photonics Technology Letters, 2002, Vol.14, No.11, p1530-p1532.

Chapter III. Extension of the powder-in-tube method for metal glass fiber fabrication and its application for microsize coaxial cable

In this chapter, we will extend the powder-in-tube method, which has been used to fabricate multi-glass material fiber in chapter 2, to the fabrication of metal-glass optical fiber. The challenge will be the fabrication of the multi-materials fiber with strongly different materials. We will focus on two applications of such fiber: microsize coaxial cable and photonic crystal fiber with metal wires (fabricated by the mix of "stack and draw" method and "power in tube" technique). The two applications will be discussed in this chapter.

III.1 The fabrication of metal-glass fiber

III.1.1 The first metal-glass fiber fabricated by Taylor-wire Process

The earliest work about metal-glass fiber was reported by G. F. Taylor in 1924 [1]. He co-drew melted metallic filaments and a glass tube to get fine micrometer metal wires. Further details of the basic technique are illustrated schematically on figure 3.1.

The process is often called "Taylor-wire process". The metal was contained in a glass tube with 2 mm internal diameter, which was closed at the bottom end. This part of the tube was heated with a gas flame until the metal was melted and the glass softened, then the tube was drawn down by hand, to produce the glass rods (~ 0.5 to 1.0 mm diameter) of 300 mm long length samples. Subsequently, these glass rods filled with metal were re-drawn down to the required diameter by passing them through a heated metal cylinder. The metal cylinder provides a uniform temperature zone which helps to produce a continuous filament of high quality [2].

Afterwards tens of years, many improved drawing setups have been invented, and many kinds of metallic wires and glasses have been drawn [2, 3].
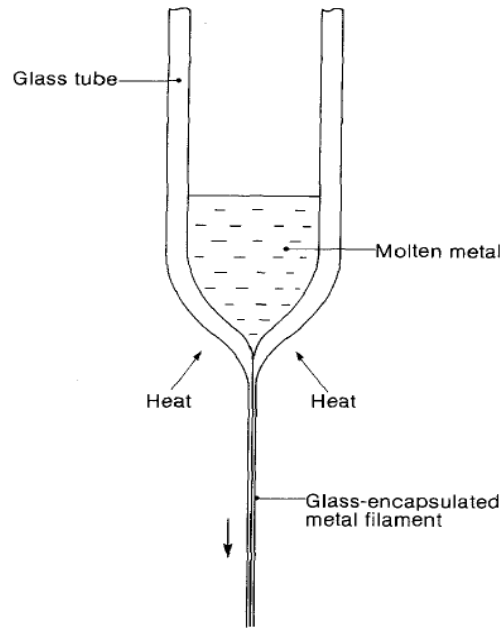
Figure 3.1: Taylor-wire process [1]

III.1.2 Glass-metal fibers fabricated by melt-filling method

When glass-metal fibers are drawn there are many incompatible properties between metal and glass materials that are exacerbated, such as melting and flow behaviors, thermal expansion coefficient mismatch, surface tension effects, wetting and interface reactions. These incompatible properties bring the large technological challenge to directly drawing glass-metal fibers. Some researchers have therefore exploited an alternative method, the melting-filling method.

The method consists of namely melting metal to become liquid and then press it into the air hole of glass fiber to form fiber with metal wire. This process is analog to the "pressure-assisted melt-filling" method. For example, in 2002, M. Fokine et.al melted the Au-Sn alloy and pressed it into a twin-hole fiber to form internal electrodes to fabricate an electro-optic switch [4]. Other researchers have also realized such metal-glass fiber with internal electrodes for developing all fiber polarimetric modulator [5], nanosecond switch associated with a fiber Bragg gratings [6], and a temperature sensor [7]. Researchers in German Max-Planck institute for the science of light have used this process to insert noble metals (gold, silver) into nano-size air-holes of photonic crystal fiber to realize a device based on plasmonic effect [8-10].

III.1.3 Glass-metal fiber fabricated by directly drawing method

Although the melting-filling method can avoid some fabrication difficulties, filling the tiny air-holes (with diameters about a micron) with melt metal over long fiber length is nevertheless extremely challenging. The nature of directly drawing method is more appropriate to produce longer fiber length.

Because drawing operation is easier if the melting point of metal matches with the flow point of the used glass [11], in the early Taylor-wire process, people often drew borosilicate glass (flow point of borosilicate glass: 820 °C) with copper (melting point of copper: 1084 °C) to get micro-size copper wire. Unfortunately borosilicate glass has large optical losses in the telecommunication wavelength region and it is more complicate to draw than silica glass, which is why researchers try to use silica instead of borosilicate. However, the large melting temperature difference between silica and most metals makes it challenging to fabricate such fibers. Nevertheless, some research groups still develop processes for drawing this kind of fibers. For example, in 2008, Jing Hou et al. realized a 0.5 m continuous long length copper photonic crystal fiber with a pitch of 6 μm [12]. In 2010, H. K. Tyagi et al realized step-index fiber with gold wire whose diameter is reduced from several micrometers to 260 nm [13].

III.1.3.1 Glass-Metal fiber fabricated by the Powder-In-Tube method

Our research group proposes to use the powder-in-tube method for fabricating metal glass optical fibers. The process is similar to the one presented in section I.6.3. The process consist in filling a silica tube with metallic powder (sealed at the bottom), the tube is fixed vertically in a furnace and heated at a temperature higher than the melting point of the metal. The heating time is about tenths of minutes in order to obtain liquid metal that becomes a solid metal rod directly inside the silica tube. The tube and the metal rod are then drawn to get a thin fiber.

III.1.3.1.1 Process of melting powder

When a copper powder in glass tube is melt, if the inner diameter of silica glass tube is small (in our initial experiments, a glass tube with inner diameter of 2 mm is used), the region accumulation effect (illustrated in figure 3.5) will occur. This effect is induced by surface tension effect of liquid copper on silica glass tube. To overcome this effect, we firstly study the definition and effect of surface tension.

(a) <u>Introduction of surface tension effect</u>

For describing the values of surface tension, the definition of surface tension coefficient is introduced firstly. Surface tension coefficient **γ** (N/m): is the surface shrink force per unit length of borderline of the surface. Its direction is vertical to surface and point to inward of surface. γ value is determined by the two kinds of materials on the two sides of surface.
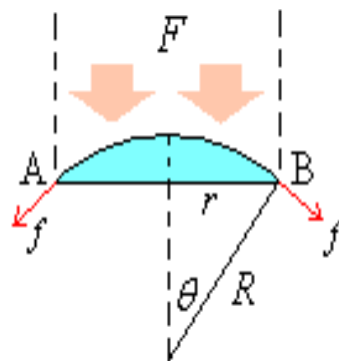
Figure 3.2: Force analyzing illustration about pressure induced by surface tension

From an analysis of the forces applied to the bottom surface delimited by the arc of circle AB (see figure 3.2, radius r), and with the definition of surface tension coefficient, we can get the equation of force (noted F on figure3.2) induced by surface tension：

$$F = \gamma \cdot 2\pi r \cdot \sin\theta = \frac{2\gamma \cdot \pi r^2}{R} \tag{3-1}$$

The area of the bottom surface circle AB is:

$$A = \pi r^2$$

So we can get the equation of the intensity of force ($P_{surface}$) induced by surface tension:

$$P_{surface} = \frac{F}{A} = \frac{2\gamma}{R}. \qquad (3\text{-}2)$$

From equation (3-2) we can deduce that smaller R leads to larger P. So the effect of surface tension is often obvious in liquid filled capillary.

Let us consider the case illustrated in figure 3.3. In this figure, P_o is the pressure of atmosphere, Δh is the height difference of liquid at the inner and outer of glass tube. The liquid surface is curved by cumulative effects of liquid gravity, atmospheric pressure and tension surface. Assuming that the curved liquid surface is a part of sphere, the angle θ is the contact angle of liquid and capillary with a vertical axis, the radius of the sphere is R / cos(θ), with the equation (3-2), the equation of capillary pressure can be defined as follows:

$$P_{capillary} = \frac{2\gamma}{-\dfrac{R}{\cos\theta}} = -\frac{2\gamma\cos\theta}{R} \qquad (3\text{-}3)$$
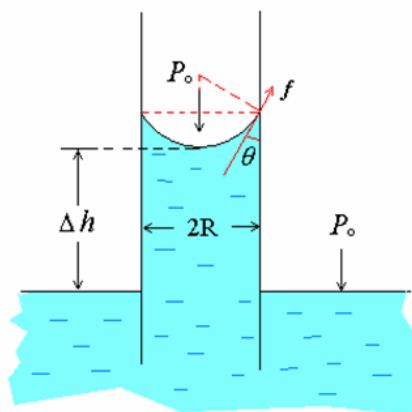

Figure 3.3: Illustration about proving capillary pressure equation

It is also important to consider the wetting and non-wetting ability of a liquid.

The wetting is defined as the ability of a liquid to maintain contact with a solid surface. It is the result of intermolecular interaction of two objects, which are brought together. The force balance between adhesive and cohesive force determines wettability. This property impacts the shape of droplets on a surface, as illustrated in figure 3.4.
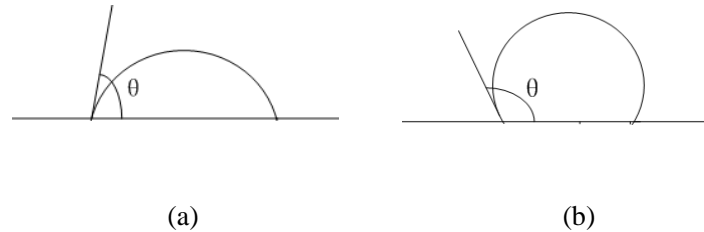

(a)   (b)

Figure 3.4: Droplet of water on an ideal surface (a) θ < 90°, wetting (b) θ > 90°, non-wetting.

The shape of a droplet can be defined by the contact angle (θ), as shown in figure 3.4. It is the angle at which the liquid interface meets the solid interface. The contact angle is determined by the resultant of adhesive and cohesive forces. As the tendency of a droplet to spread out over a flat, solid surface increases, the contact angle decreases. Thus, the contact angle provides an inverse measure of wettability [14]. When the contact angle is θ < 90° (called wetting case) the wetting of the surface is very favorable, and the fluid will spread over a large area of the surface. When contact angle is θ > 90° (called non-wetting case), the wetting of the surface is unfavorable, so the fluid will minimize the contact with the surface and form a compact liquid droplet. Now we have to exploit this definition in our experiments of liquid copper inside silica tubes.

(b) Region accumulation effect during melting copper powder in silica tube

In our experiment, we use copper powder that is melted into liquid copper. Liquid copper has a low wetting capability with SiO_2, the contact angle between copper and silica is around $112.5°$ [14]. Furthermore, the volume of liquid copper is lower than the initial volume of copper powder. In general, it is assumed that the air-ratio is between 20% - 40% of the whole powder volume [15]. Together with the capillary tension effect, the liquid copper tends to form sphere shape, and brings region

accumulation effects; the copper accumulates in different tube regions. A basic experiment to illustrate this effect consists in filling a silica tube with copper powder, heating it up to melting temperature of copper and then cold it down to room temperature. The result, shown in figure 3.5, is a succession of small copper "bullets" separated with air gaps.

Figure 3.5: Photography of a silica tube filled with copper powder that is heated to obtain liquid copper and then cold down to room temperature. This experiment has been done at Xlim.

It means that during the experimentation stage, this effect has to be taken into account to obtain a continuous rod (around one tenth of centimeters at least). One way to avoid this effect can be to study the critical inner diameter of the glass tube.

(c) <u>The critical inner diameter of silica tube in the case of copper</u>

We need to select a silica tube with inner diameter large enough to counteract the effect of that capillary pressure, which is induced by surface tension of liquid copper and defined from equation (3-3) as follow:

$$P_{capillary} = \frac{-2\gamma_{surface}\cos\theta}{R_{tube}}$$

This capillary pressure prevents the separated liquid copper to drop. Figure 3.6 is

an illustration used to define the critical inner diameter of a tube to avoid copper discontinuity.
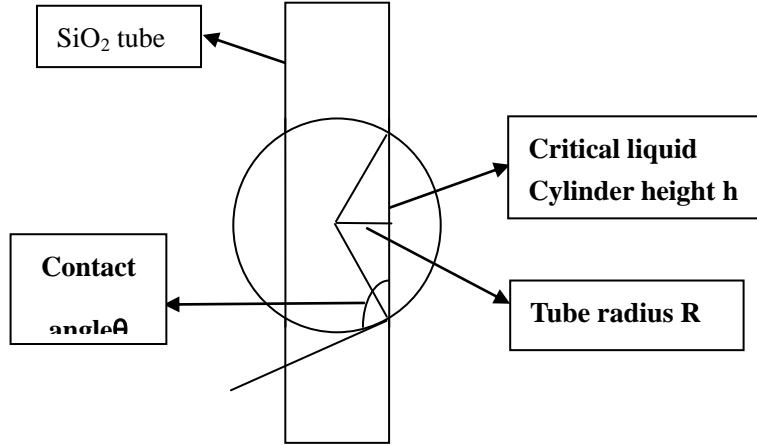
Figure 3.6:   Critical state picture of liquid copper cylinder

In the following equations, we define: h is the critical liquid cylinder height, g is the gravitational acceleration (g = 9.8 N/kg), $R_{critical}$ is the critical radius of silica glass tube. The contact angle is $\theta = 112.5^{\circ}$ and the surface tension coefficient of liquid copper is $\gamma = 1.0\text{-}1.3$ N/m (it is illustrated in figure 3.7, it lists some measure values by different measure methods at different years), the density of liquid copper $\rho_{Cu}(liquid) = 8.02 \times 10^3$ kg/m^3 [16].). In the critical state, the capillary pressure should equal the pressure of liquid copper, leading to:

$$P_{capillary} = P_{Cu}$$

$$\frac{-2\gamma \cos\theta}{R_{critical}} = \rho_{Cu}gh = \rho_{Cu}g2R\tan(180° - \theta)$$

$$R_{critical} = \sqrt{\frac{\gamma\cos\theta}{\rho_{Cu}g\,tg(180° - \theta)}}$$

$$\sqrt{\frac{1\times\cos(112.5°)}{8.02\times10^3\times9.8\times tg(180° - 112.5°)}} < R_{critical} < \sqrt{\frac{1.3\times\cos(112.5°)}{8.02\times10^3\times9.8\times tg(180° - 112.5°)}}$$

$$1.41 \text{ mm} < R_{critical} < 1.61 \text{ mm}$$

$$2.82 \text{ mm} < D_{critical} = 2R_{critical} < 3.22 \text{ mm}$$

For this development, we can get the tube's critical radius range, $R_{critical}$ is about 1.42-1.61 mm, corresponding to the critical inner diameter D about 2.82 - 3.22 mm.
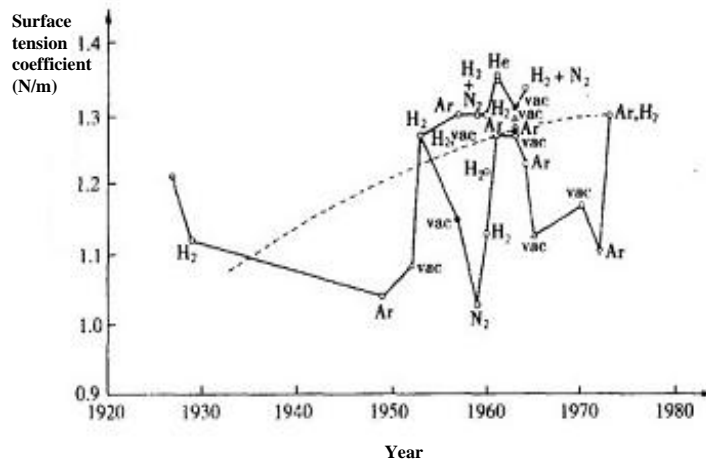
Figure 3.7: Surface tension value of liquid Copper measured
by different methods at different years [16].

From the geometrical relation shown in figure 3.6, we can also get the critical liquid cylinder height (h):

$$h = 2R \tan(180^{°} - \theta) = D \tan(180^{°} - 112.5^{°}) = D \tan(67.5^{°}) = 2.41 \text{ D}$$

So the behavior of the fabrication of a long continuous copper rod by the powder-in-tube method versus the inner diameter of a silica glass tube is illustrated on the figure 3.8. From this figure, we can see that when the inner diameter of glass tube is smaller than critical inner diameter, the fabricated longest copper rod length is proportional to inner diameter of glass tube. When inner diameter of glass tube is beyond critical inner diameter, we should be able to obtain very long continuous rods.
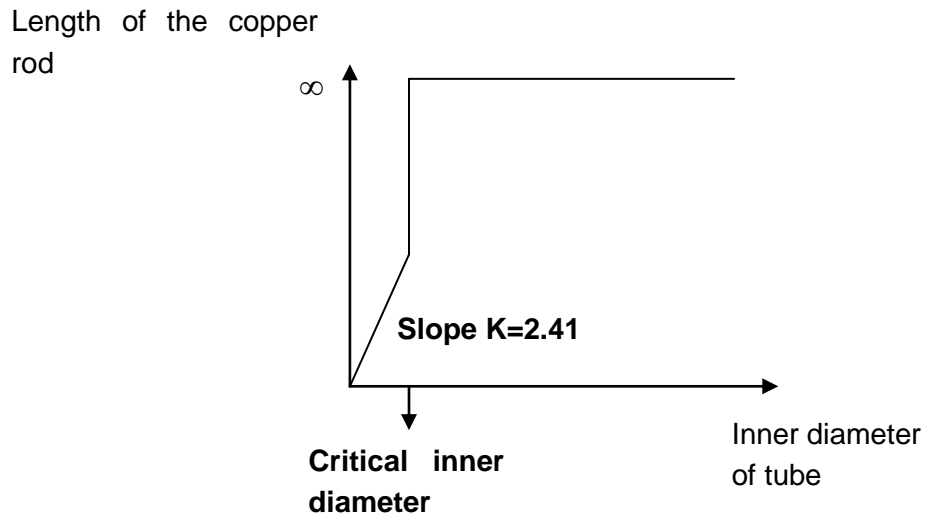
Figure 3.8: Length of copper rod achievable versus the inner diameter of tube.

(d) Melting metallic powder time

Because there are many interstitial air gaps among the powder grains, melting powder material needs much more time than melting the same mass of solid material. One experiment indicates that thermal conductivity of metal powder is only 1/1662 of thermal conductivity of solid metal [17].

III.1.3.1.2. Drawing theory of silica fiber with copper wire

Copper is one kind of crystal, it has a fixed melting temperature. When solid copper becomes liquid copper, the viscosity of copper will change abruptly. The viscosity of liquid copper is around $4 .10^{-2}$ Pa·s at the melting temperature (1084 ˚C). This viscosity value of liquid copper is not in the viscosity region which can be drawn into fiber, typically in the range $10^{4.5}$-$10^{6.5}$ Pa·s. So the process for drawing SiO_2 fiber with copper wire is essentially different than conventional fiber.

(a) Drawing theory:

Due to its surface tension, liquid copper cannot flow at the inner of fiber. By calculation, we can get that the surface tension of liquid copper within a silica tube of 20 μm diameter can support a height of liquid copper of 1.27 m. The numerical application is developed below:

$$P_{surface} = \frac{-2\gamma\cos\theta}{R} = P_{liquid} = \rho gh$$

$$h = \frac{-2\gamma\cos\theta}{\rho gR} = \frac{-2\times1.3\times\cos112.5°}{8.02\times10^3\times9.8R} = \frac{1.27\times10^{-5}}{R} = \frac{1.27\times10^{-5}}{10\times10^{-6}} = 1.27(m)$$

Moreover, the cooling rate of the fiber during the drawing stage is estimated to be about $10^5\,K\,sec^{-1}$ for a 100 to 200 μm diameter fiber [2, 18]. So for the general case, liquid copper height is shorter than 1.27 m, and liquid copper cannot flow at the inner of fiber.

In the classical drawing method, one main faced problem, is that continuous long metal wire fiber is not easy to get, due to some strong discrepancy in mechanical properties between metal and glass materials. In the following, we are going to study the breaking reasons of metal wire, and propose some improved drawing methods.

(b) Study of the breaking reasons of copper wire

The figure 3.9 is a photography, taken with a microscope, of longitudinal section of a fiber composed of a silica cladding and a copper core. This picture illustrates the breaking of the copper wire.
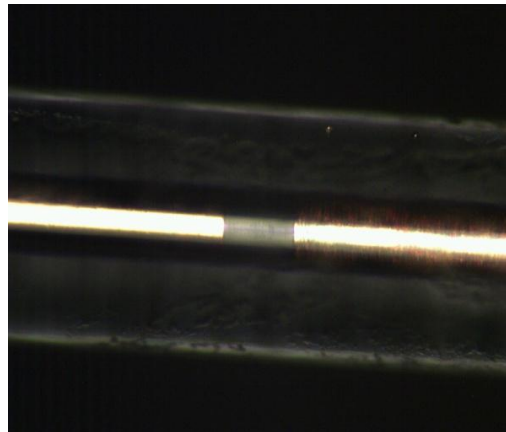

Figure 3.9: Microscope picture of a longitudinal section showing the breaking of a copper wire inside a fiber with a silica cladding.

As mentioned above, the drawing operation is easier when the melting temperature of the metal is close to the flow temperature of the used glass for the tube.That is why people often used borosilicate glass tubes. The flow temperature of

borosilicate glass is around 820 ˚C, and the melting temperature of copper is around 1084 ˚C [11]. In the following, **I am presenting my personal interpretation** of the difference between drawing borosilicate glass together with copper and drawing silica glass together with copper, both processes are schematically represented in figure 3.10.
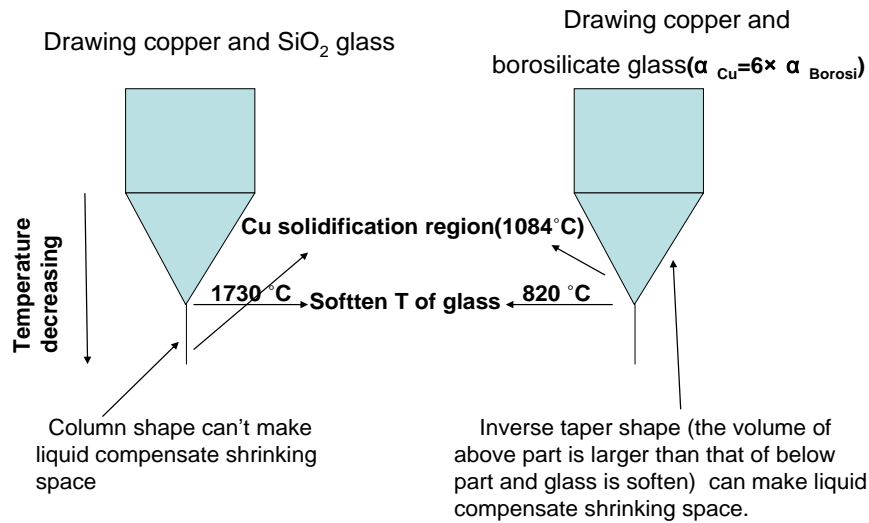
Figure 3.10: Schematic representation of the drawing processes for silica glass with copper and borosilicate glass with copper.

The blue square parts and the inverse taper parts represent the fiber preform during the fiber drawing process. Blue square part represents the part of preform which is not softened and deformed. Blue inverse taper part represents the part of preform which becomes soft and thin. Below the bottom of inverse taper part is the column shape fiber where glass still soft and becomes thin. In the vertical direction of inverse taper part and column shape fiber, temperature will decrease along vertical axis. So the temperature in the bottom of inverse taper part should be the soften temperature of glass.

The density of solid copper is 8.94 g/cm^3 and the density of liquid copper is 8.02 g/cm^3. So when copper solidifies, copper's volume decreases. When liquid copper drops change from liquid to solid state, copper's volume decreases, if there is

no more copper to compensate the contraction of copper's volume, copper contracts leading to break. It means also that if there is more copper to compensate the contraction of copper's volume, we will be able to get continuous long copper fiber.

There is one well known example which has the similar phenomena to the breaking case of our copper wire. It is the thermometer working theory. When temperature falls, the volume of mercury (Hg) contracts, at the same time, the surface tension of liquid mercury in narrow region avoids drops of mercury. All these factors make liquid mercury break and mercury column keep at that position for pointing the temperature, as illustrated on the figures below:

(a)   (b)

Figure 3.11:   (a) Clinical thermometer (b) Break in narrow region

The left picture of figure 3.10 depicts the process of drawing copper and silica glass. The temperature in the end of inverse taper part should be silica glass softening temperature (around 1730 ˚C). The solidification temperature of copper is 1084 ˚C, moreover, the temperature decreases along the vertical direction from top to bottom. So the solidification position of liquid copper is in the column shape fiber. Copper's volume in the column shape fiber will decrease due to solidification contraction. But there are the same volumes copper in above position and below position in the column shape fiber that is not soft. So in the column shape fiber, liquid copper cannot compensate the contraction at the copper solidification position. So the breaking of copper fiber occurs. The process is similar to the breaking of mercury.

The right picture of figure 3.10 depicts the process of drawing copper and

borosilicate glass. In the reference [11], the drawing temperature is about 1300 ˚C for copper and borosilicate glass. The temperature in the end of inverse taper part should be the softening temperature around 820 ˚C of the borosilicate glass. The melting temperature of copper is 1084 ˚C, moreover, the temperature decreases along the vertical direction from top to bottom. So the solidification position of liquid copper is in the region of inverse taper part. The contraction of copper solidification occurs in the region of inverse taper part. Please notice that in the case of above drawing copper and silica glass process, the solidification position of liquid copper is in the column shape fiber. This is the key reason for the difference of their drawing results. But in the region of the inverse taper shape, due to the geometry character of the inverse taper shape, the volume of top part is larger than that of bottom part (larger volume can compensate the contraction of copper) and glass is soft (the glass which is drawn to prolong will drag liquid copper drop). These factors can make liquid copper in top part of inverse taper shape region compensate the contraction of the copper solidification position in the bottom part of inverse taper shape region. So it can get continuous long copper fiber.

(c) Improved drawing method for getting continuous long silica-copper fiber

1.Increased pressure method

As explained above, due to the surface tension of liquid copper, it cannot flow into the fiber and so cannot compensate the contraction of copper solidification. If we apply an external pressure to overcome the surface tension of liquid copper for making liquid copper flow in the fiber, liquid copper can compensate the contraction of copper solidification. So we can get continuous long silica-copper fiber. For example, for a fiber with 10 μm diameter copper wire, the surface tension pressure is around 200 kPa (see relation below). However, the difficulty of this method is that too large pressure is easy to break softened glass cladding. So in our drawing experiments, this solution is not used for drawing these fibers.

$$P_{capillary} = \frac{2\gamma_{surface}\cos\theta}{R_{tube}} = \frac{2\times1.3\times\cos112.5°}{5\times10^{-6}} = 200kpa = 2atm$$

2. Slow speed drawing method

In the first paper on the Taylor wire process [1], it has been mentioned that "when heated in a flame and drawn in air, those metals which contract on solidifying will form breaks at short intervals, while those which expand will break the glass capillary. When drawn slowly from a heated cylinder, however, a perfect cast is formed, because solidification takes place at a point adjacent to the liquid metal." It points that slow speed drawing is easier to get continuous long metal fiber.

In this part, I explain the detailed reason, as follows:
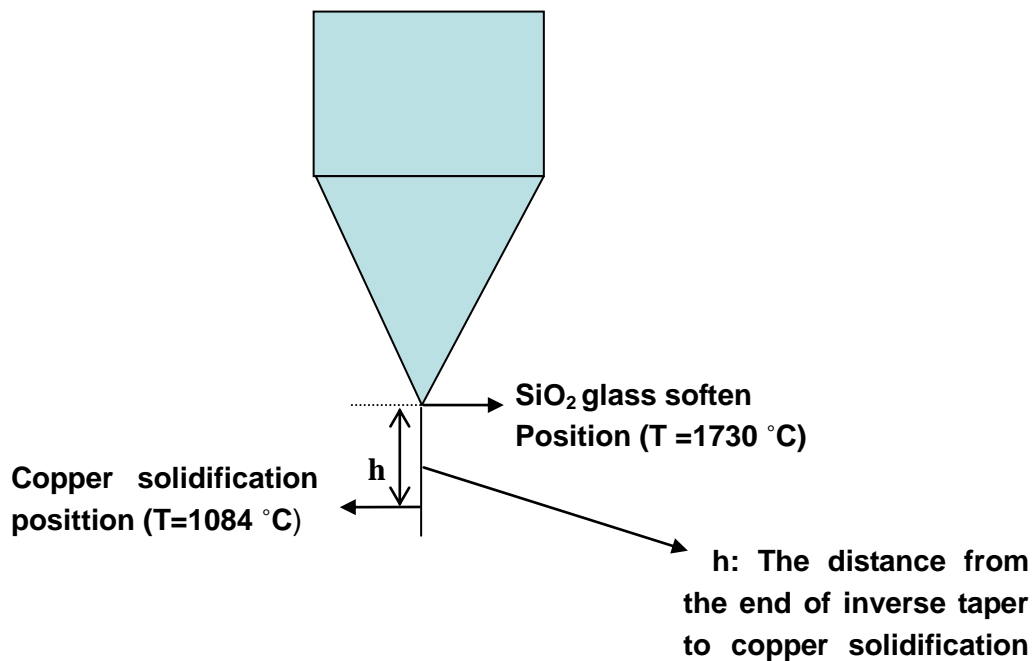
Figure 3.12: Illustration of the slow speed drawing method

In figure 3.12, we assume that the drawing velocity is around 3 m/min (5 cm/s). The above part (p81:**lll.1.3.1.2. (a)Drawing theory)** mentions that cooling speed order of a 100 to 200 μm diameter fiber is in the order of 10^5 ˚C/s. Assuming that the copper temperature decreasing speed is constant during the process. The time *t* for copper's temperature to change from 1730 ˚C to 1084 ˚C should be t= (1730-1084) $/10^5$ = 6.5×10^{-3} s. So the distance (h) from the end of inverse taper to copper solidification position is: h=vt =5 cm/s $\times 6.5 \times 10^{-3}$ s =325 μm. When h and the diameter

of the hole are the same or close, the solidification position can contact liquid copper to compensate the contraction of copper solidification. So it is easier to get continuous long fiber.
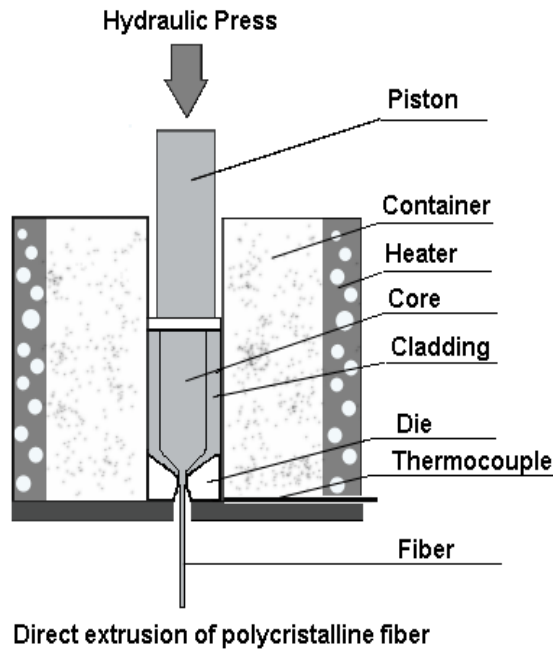
Figure 3.13: Extrusion method for fabricating crystal fiber [19]
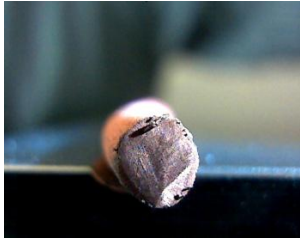
I have presented two ways for improving the drawing methods. One proposed way consists in applying a pressure. The method is similar with the extrusion method for fabricating crystal fiber [19] (see figure 3.13). The second one, more realistic with our drawing conditions and equipments is to draw with a slow speed, this method can be compared with the Micro-Pulling Down method (drawing speed: several millimeter per minute) for fabricating crystal fiber [20].

III.1.4 The fabrication results of preforms and fibers including copper parts

During my thesis, a lot of works on the fabrication of preforms with copper rod and fibers with copper wire were done. Several fabrication stages were established, depending on the available equipments and feedback on experiments. These experiments were correlated with the theoretical part, leading us to adapt or modify the processes.

III.1.4.1 First stage - Preform fabrication using a vertical tubular furnace through powder-in-tube method or core suction technique.

First, I have used a vertical tubular furnace that has a highest heating temperature of 1300 $^{\circ}$C, with a length of 300 mm. Since the fusion temperature of copper is 1084 $^{\circ}$C, this furnace is well adapted to melt copper. In the following tables, I have listed some experimental results and comments on the fabrication of preforms done with this vertical tubular furnace.

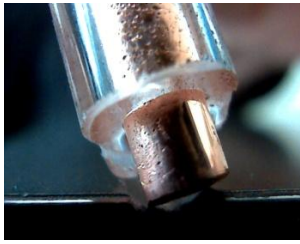|	Experimental conditions	Results	Pictures and comments
Preliminary test	Melting Copper powder in quartz crucible. Heating T=1100 $^{\circ}$C	Goal: to determine working temperature of copper / tubular furnace	Copper shrinking, Good homogeneity of the piece, Surface oxidation
Experiment A	Melting Copper powder in silica tube 3/12 mm (ID/OD mm), T = 1100 $^{\circ}$C. ID: Inner diameter OD:Outer diameter	Goal: Preform realisation. Some metal pieces are not connected together, Pink color, Rough surface.	Copper shrinking, if polishing Surface oxidation, Shining

Experiment B	Melting Copper powder in silica tube 4/8 mm T = 1100 °C	Goal: Preform realisation. Some metal pieces are not connected together, Pink colour – One piece shining.	 Length is sufficient to be drawn to a fiber.

Table 3.1: Resume of some experiment results done with this vertical tubular furnace.

This first set of experiments were useful and demonstrates that it is possible to fabricate preforms with copper rod inside, by using the powder-in-tube method with optimized heating temperature and time in the furnace. The goal of the second step of these experiments was to realize fiber with copper wire inside. Process and results are summarized in the following table:
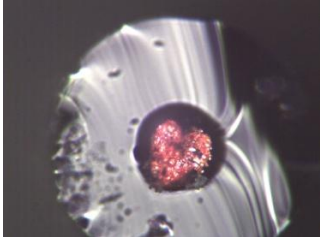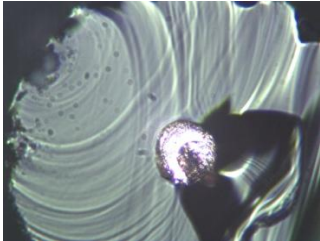
Experiment C	Same experimental conditions of experiment B The goal is to produce a fibre with copper wire inside	Goal: fibre fabrication. Some metal pieces are not connected together, Pink colour – One piece shining.	 Fibre realisation from diameter 200 microns up to 400 microns, Copper shrinking inside the fiber, Shining copper – no visible oxidation
Experiment D	Same experimental conditions of experiment B T = 1000 °C The goal is to produce a fibre with copper wire inside	Mechanical behaviour improved, continuity of the copper rod over some tens of cm Pink aspect	 Fiber realisation Continuity of the copper wire, Fibre diameter from 40 to 600 microns.

Table 3.2: Some experiment results done to produce optical fiber.

The following pictures detail the results obtained by experiment D. The figure 3.14(a) is photography of the drum (where the fiber is rolled) after the experiment D. The fiber in pink or orange corresponds to long length of silica fiber with an inner copper wire. This realization is confirmed by the picture in figure 3.14(b), of a piece of that fiber after a tight bend shows the good quality of the copper wire (the copper wire is not broken when bending it).

<div align="center">(a)   (b)</div>
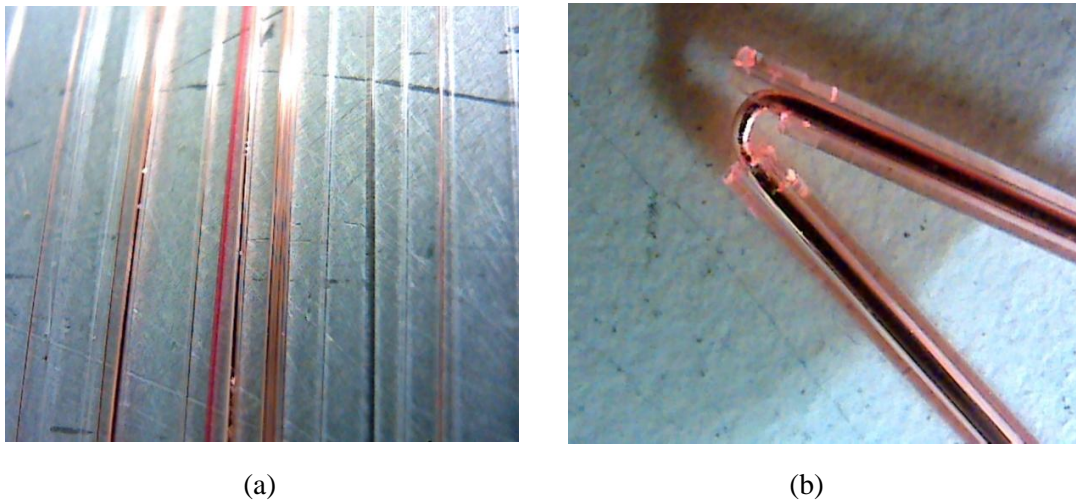
Figure 3.14: Realization of a fiber with copper wire, (a) fiber coiled on the drum, (b) Robustness evaluation of the copper wire by bending the fabricated fiber.

Several results and conclusions can be extracted from these pictures:

- It is possible to produce long length of fiber with copper wire inside, some hundred of meters have been obtained for this drawing.

- The copper wire produced, is a real wire – and not a densified powder – figure 3.14(b) demonstrates its robustness. To complete these observations, the electrical resistivity of the wire was measured and give a value comparable with the well know value(1.68×10^{-8} Ω·m) for copper resistivity .

Unfortunately, the length of fiber with continuous copper wire is limited to some meters. Between each samples, there is a small air-gap of around 100 µm long length. This is why, it is important to improve the process of preform and fibre fabrications.

During this time, we have also tested another way by using the core suction method that is described in chapter 1.

The process is the following: copper powder is melted in a quartz crucible staying in a vertical resistive furnace heated at 1300 $^{\circ}$C. A thinner silica glass tube is inserted in the furnace by the top and put inside the melted copper powder. Then the top of the thin silica glass tube is connected to a vacuum pump for pumping liquid copper into this thin silica glass tube. By our experiment results, only 10 cm is fully filled by copper (but also with some defects). These results are shown in figure 3.15.
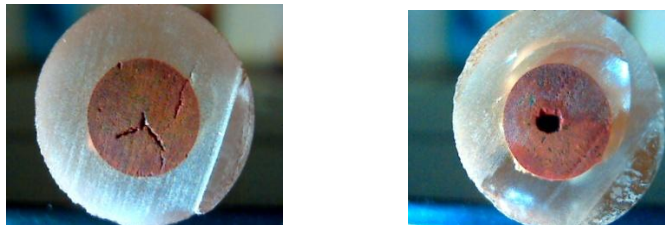
Figure 3.15: the section cross of copper core preform fabricated by the core suction method

To improve the quality of the preform – in terms of length without cracks but also in terms of homogeneity (Figure 3.15) - we decided to take advantage of the furnace of the drawing tower, and to develop a 'dynamic' process by moving the preform during heating.

III.1.4.2 Second stage – Preform fabrication using an inductive furnace

In order to increase the length of preform 'treated' we have made some experiments using the inductive furnace of the drawing tower. The induction furnace used deliver temperatures from 1000 $^{\circ}$C to at least 2000 $^{\circ}$C. Silica glass tubes with inner/outer diameters of 2/8 mm were filled with fine copper powder. Such preforms were installed into the induction furnace and the temperature around 1085 $^{\circ}$C was reached (fusion temperature of pure copper under atmospheric conditions). Long length of tubes (max 50 cm) could have been treated thanks to a mechanical system

which makes the preform going down into the furnace with a controlled speed. In our tests, a speed around 6 mm/min has first been chosen.

Figure 3.16 shows the bad results of such tests. Copper powder has melted but many copper packets have been formed into the silica tubes, leading to the formation of air gaps. The phenomenon should be the result of region accumulation effect. The reason is that the inner diameter of 2 mm of the silica glass tube is smaller than the calculated critical inner diameter (2.82-3.22 mm) of region accumulation effect during melting copper powder in silica tube, so region accumulation effect occurs.
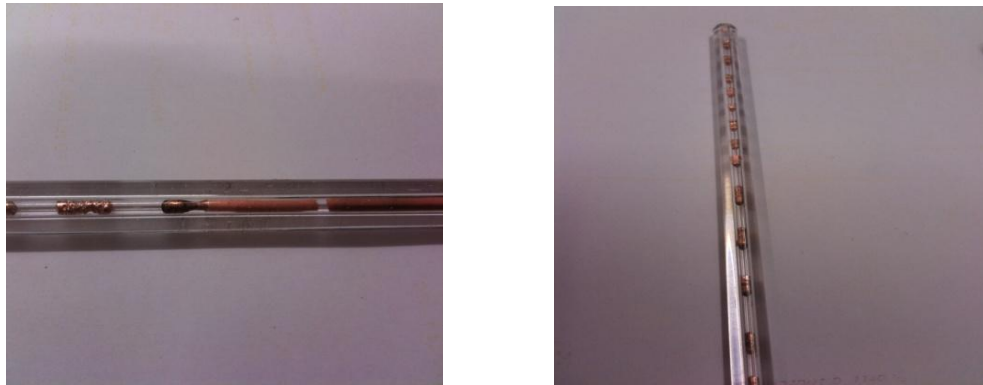
Figure 3.16: Photographies of a silica tube filled with copper power treated with our process based on an inductive furnace and tube translation.

On one hand, the induction furnace we use for the preform drawing allows to heat a small zone of the preform (7 cm) to temperatures as high as 1800 $^{\circ}$C (drawing temperature of silica) very quickly (a few minutes) with low power consumption (~5 kW). In the other hand, the measured temperature from the power of the furnace which we control is detected out of the heating zone. The heating element is composed of pure carbon which is consumed all along the heating and cooling cycles. As a matter of fact, for the same power delivering by the furnace, the temperature would not be exactly the same from one test to another. To develop the suitable copper preform, we have to make our tests with an appropriate furnace. That is why we decided to use the resistive furnace of the industrial drawing tower we have at XLIM.

At this time, several kinds of parameters have to be improved in order to increase

the quality of the preform:

- Stability of the process in terms of temperature / feed speed (shift to the resistive furnace of the drawing tower)
- Quality and Compaction of the copper powder
- Duration of heat treatment
- The temperature of heat treatment

We will explore these five points of improvements in the next paragraph.

III.1.4.3. Improvement of the process

The nature of drawing furnace

Resistive furnace gives us the capability to adjust precisely the temperature, with a nice repeatability and stability. A control loop ensures a stability of +/-1 $^\circ$C during all the treatments. The furnace we have is able to deliver temperatures from 400 $^\circ$C to 2200 $^\circ$C very quickly (~10 min). Power consumption is nevertheless higher than that of the induction furnace. The feed speed of the preform is also adjustable from 0.1 mm/min to 20 mm/min. During our tests, we can change heating temperature and feeding preform speed to get suitable parameters to realize a high quality copper rod in glass tube.

The nature of the copper powder

We have used two copper powders from two different suppliers. The one from ALFA AESAR, which present small and regular grains, gave good results, see the picture in figure 3.17(a)). Another powder with bigger and coarser grains leads to results totally different from the first powder (Cf. figure 3.17(b)), for the same experiments conditions (temperature, speed and compaction of the powder). This last powder seems also very sensible to ambient humidity. For each test, the color of the copper core of the preform changed when we have put the preform over the furnace (figure 3.17(b)) and after 5 minutes (figure 3.17(c)). The copper has bleached because of the oxidation of copper has occurred on the surface of the copper bulk. This result

has shown also that the bulk copper does not stick to the inner surface of silica tube, so that water and oxygen molecules are able to enter the preform and contaminate the bulk copper.

(a) (b) (c)
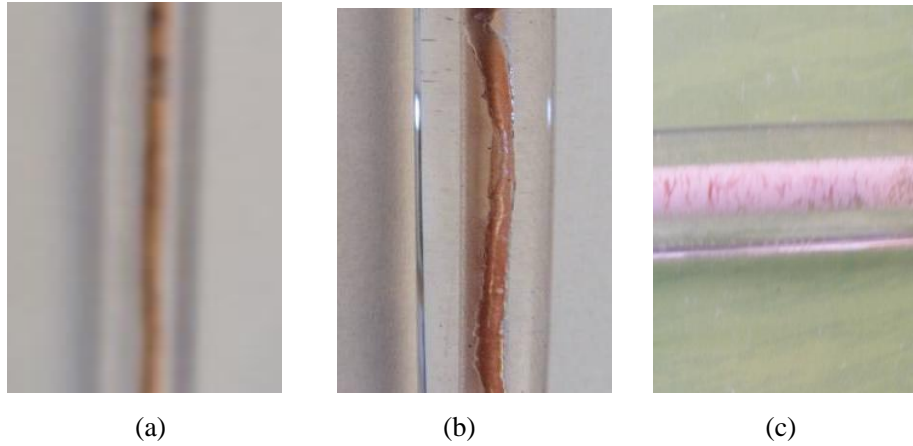
Figure 3.17: Photographs of silica tube filled with different copper powders after treatments. (a)Produced from Small and regular copper grains. (b) Produced from big and coarser copper grains. (c) the results for copper rod(b) put in furnace for 5 minutes.

The compaction of the copper powder during the preparation of the preform

It is quite evident that using fine and regular powder grains leads to better powder compaction compared to bigger and coarser grains. That is why it is better to use the powder from ALFA AESAR for our tests.

(a) (b) (c)

Figure 3.18: Effect of compaction ratio on the preform quality. The preform obtained from (a) copper powder which has no enough compaction (b) copper powder which has correct compaction (c) copper powder which is packed too much.

93

Figure 3.18(a) is a photograph of preform obtained after treatment for which the powder compaction was not enough. The bulk copper does not occupy all the volume of the inner space of the silica tube. This leads to the formation of air holes into the preform core and/or free circulation of water and oxygen molecules which can oxidize the copper surface.

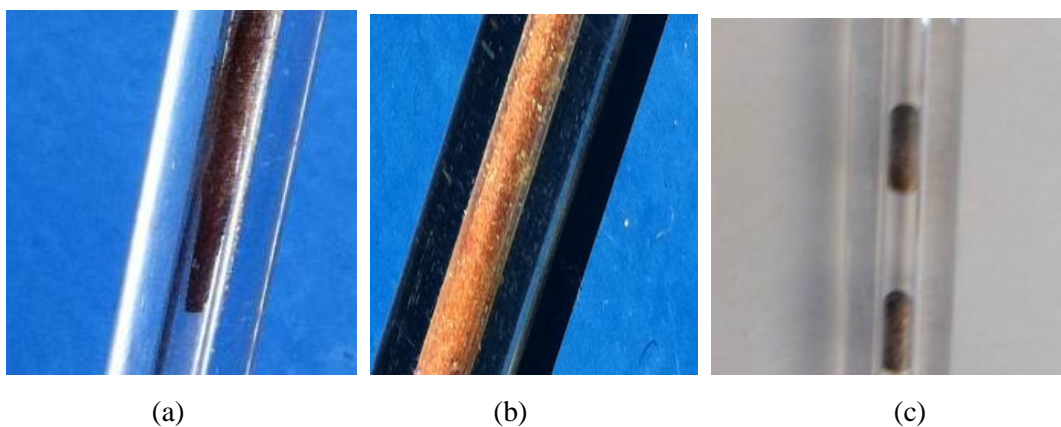The opposite case, i.e. the powder has been packed too much is illustrated in figure 3.18(c). Copper packets are formed after heat treatments leading to air holes. Such preforms can not been drawn because such air holes can involve swelling and finally a break of the preform in the furnace.

A Photograph of a correct sample with correct compaction of the powder is shown in figure 3.18(b).

The duration of the heat treatment

The duration of the heating treatment depends on the feed speed of the perform into the furnace.A low speed involves long heating treatment duration and leads most of the time to the formation of copper packets and air holes into the silica tube. This is the result of region accumulation effect. On the opposite, a high speed involves short heat treatment duration and in many cases, the copper had no time to melt sufficiently. We have obtained powder or granular and very porous rod after this heating treatment. A compromise has been found with a preform speed between 6 to 10 mm/min.

The temperature of the heating treatment

The temperature of the heating treatment has a strong impact on the nature of the copper rod obtained. The results of this impact are shown in figure 3.19. Note that from left to right, there is only a temperature difference of 10 $^{\circ}$C between each sample presented here.

In the case where the temperature is too low, the aspect of the bulk copper after the heat treatment is still granular. One can think that only the grain surface has melt and powder grains have been then glued together. The bulk copper is very porous and it can be broken very easily, as shown in figure 3.19 (a).

In the case where the temperature is too high, some copper packets are formed into the inner hole of the silica tube (shown in figure 3.19(C)). This is the result of region accumulation effect.

(a) (b) (c)
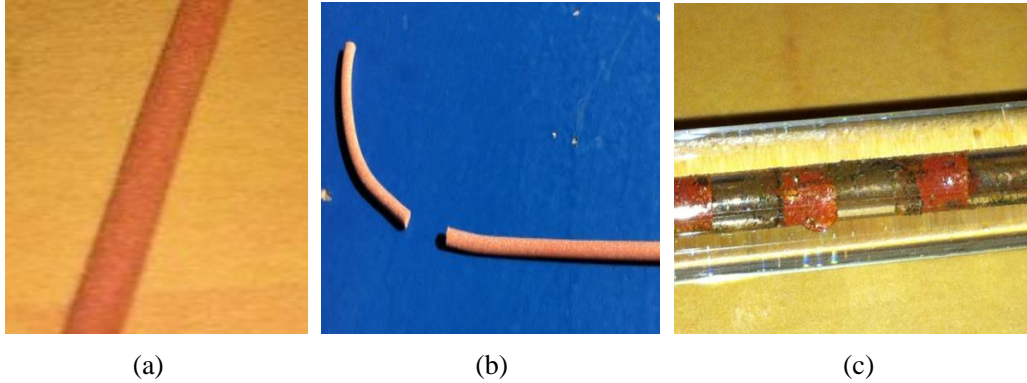
Figure 3.19 Photographs of copper rods obtained with this developed process showing the impact of the temperature on the copper rod. The temperature of the heating treatment (a) which is too low (b) which is good enough (c) which is too high.

When temperature is good enough, we obtain a continuous, non porous (this term is defined by the robustness of the copper rod and by the measured density of this one) and brilliant copper rod. The bulk copper can be bent without breaking it. After applying the bending stress, the rod remains curved. But it can break for a small bend radius. This is the case of the sample in figure 3.19(b). In this photograph, the copper rod seems granular, but after polishing by hand on the surface of the bulk, the brilliant aspect of copper is revealed as seen on the photographs below:

(a) (b)

Figure 3.20: Oxidation behavior of the copper rod (a) before the copper rod is polished (b) after the copper rod is polished

By adjusting these four main parameters, we succeeded in the realization on

samples as long as 90 cm. These ones have been heat treated in the resistive furnace at 1130 $^\circ$C, in a 4/8 mm inner/outer diameter silica tube filled with compacted fine and regular copper powder, with a feed of 10 mm/min.
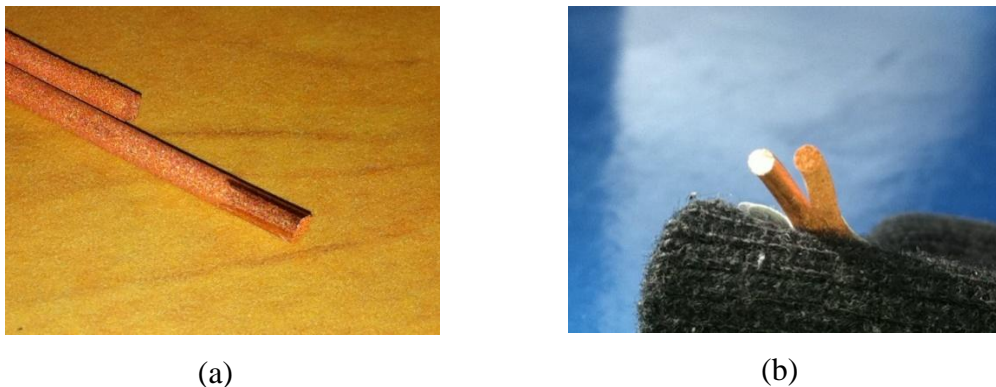
All these experimental results have been used to define and design a new equipment - called 'vitrification unit' - in strong collaboration with Silitec Fibre SA. This Switzerland company has used the powder way technique to realize the cladding of MCVD preform and patented this process in 2005 [58].

This set-up was implemented in the laboratory in June 2012. Some first experiments have been done recently and are the best results to date in our group. Some results will be presented in the next paragraph.

III.1.4.4. Third stage – Preform fabrication using a vitrification unit

The system is shown in figure 3.21. It is composed of several function / equipments:

- An home-made inductive furnace, with a very good temperature stability, temperature range from 400 $^\circ$C to 2000 $^\circ$C

- Two mechanical systems to maintain the preform, it is possible to use rotation of the preform during the process.

- Vacuum system during the process is to remove air captured between the copper grains. Grain treatment is done before the process (to remove impurity).

We have realised a fabrication test of copper rod in a silica glass tube with this vitrification unit. The main results are the following (Cf. figure 3.22):

- All the powder is transformed in a solid rod.

- The rod is basically continuous. Only the small gap occurs. this will be solved in the future.

- It is a solid rod, no porosity, the weight / volume of copper is good.

- The interface gap between the copper and the silica tube seems very thin, namely due to the vacuum applied during the process
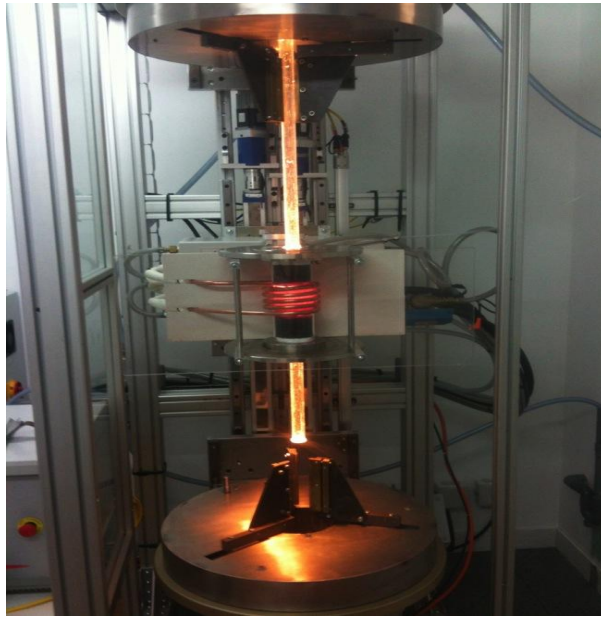
Figure 3.21 Photograph of the vitrification unit built at XLIM

Figure 3.22: Photograph of the first realization of a copper preform using the vitrification unit

At this time we can conclude and confirm that we have a very smart equipment to obtain preform including metallic parts inside. The above part was dedicated to a basic preform – a metallic rod in a silica cladding; the following part will deal with two other more interesting fabrications that are a PCF including copper wires and a study and attempts to realize a microsize coaxial cable.

III.1.4.5. Photonic crystal fiber with two copper wires

Thanks to the first experiments described previously, we combined powder- in-tube method and stack-and-draw method for fabricating photonic crystal fiber with copper wires. This fabrication was done at the beginning of my thesis and unfortunately the vitrification unit was not in the laboratory at that time. It means that results should be improved in the future with the vitrification unit.

(a)   (b)
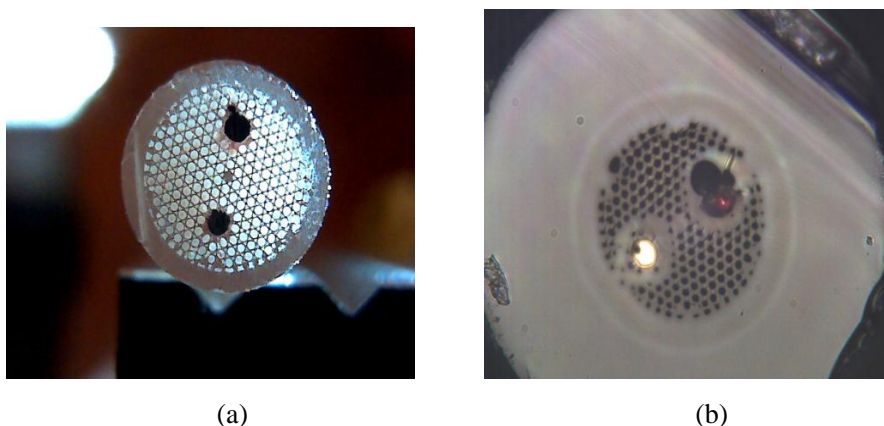
Figure 3.23: (a) and (b) are respectively preform picture and cross section picture
of photonic crystal fiber with two copper wires.

We have obtained a very long length of optical fiber (some hundred of meters), but unfortunately, the copper wires are not continuous along all the fiber length. Some meters of this fiber have been characterized.

The fundamental mode field profile of this kind of optical fiber and the transmission spectrum are shown in figure 3.24. From this figure, we can see that the propagated light is well confined in the core of the fiber, and there is no resonant peak in the whole transmission spectrum. These results mean that surface plasmon resonant phenomenon with metal does not occur in this fiber, according to our expectation.

(a)   (b)
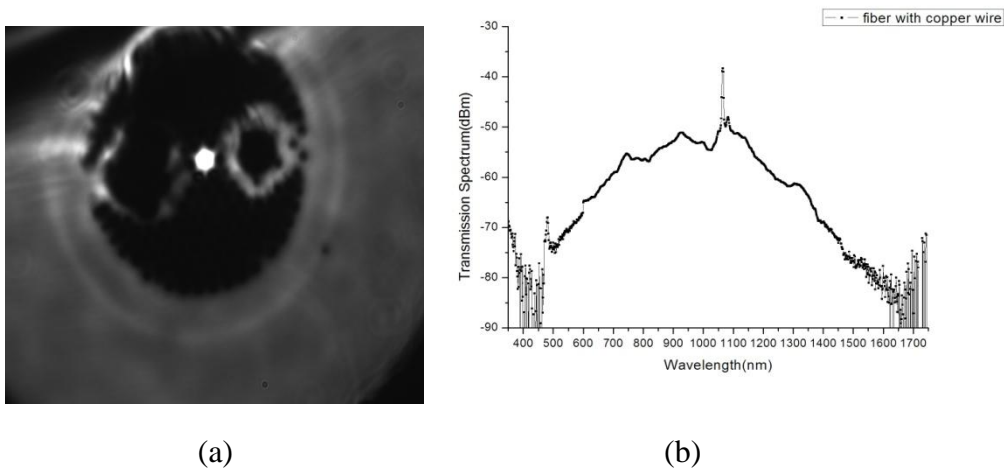
Figure 3.24: (a) Photograph of the fiber output when light is launched and propagated into the core. The related transmission spectrum recorded with an optical spectrum analyzer.

This first realization was useful to demonstrate the possibility to mix two processes to obtain a novel design of optical fibers. The potential of such fibers is important and has to be improved in terms of fabrication to realize long length fiber and demonstrate original behavior. In the future, this demonstration could be the foundation for developing applications on the interaction between light and 'electricity' along the fiber such as polling or on plasmonic components.

III.2 Application of metal fiber: microsize coaxial cable fabrication.

III.2.1 Introduction of coaxial cable

Coaxial cable is a kind of transmission line for radio frequency signals. It has two coaxial conductors. Inner conductors and the outer shield share the same geometric axis. Coaxial cable was invented by english engineer and mathematician Oliver Heaviside in 1880. The structure of coaxial cable is shown in figure 3.25

Figure 3.25: Schematic representation of a coaxial cable structure.

The applications of coaxial cable include feedlines connecting radio transmitters and receivers with their antennas, computer network (Internet) connections, and distributing cable television signals.
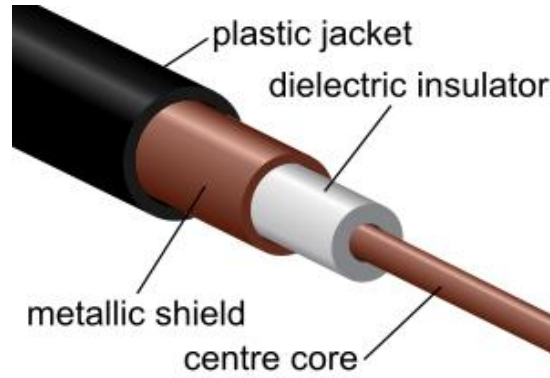
The current guided by coaxial cable is Alternating Current (AC). If the high frequency alternating current is guided by general electrical wire, the electrical wire will be equal to an antenna, it will radiate power outward. The effect will increase the loss of signal. Coaxial cable is designed to solve this problem. The power radiated by inner electrical wire will be insulated by outer conductor.

With the increase of the distance from the conductor surface, the Alternating Current (AC) density J in conductor decrease exponentially from its value at the surface J_S, as follows:

$$J = J_s e^{-d/\delta} \tag{3-4}$$

where δ is the skin depth. It is defined as the depth below the surface of the conductor when the current density has fallen to 1/e (about 0.37) of J_S. In normal cases, the skin depth is well approximated by:

$$\delta = \sqrt{\frac{2\rho}{\omega\mu}} \tag{3-5}$$

With ρ the resistivity of the conductor, ω the angular frequency of the propagated current, and μ the absolute magnetic permeability of the conductor,

So the high frequency AC signal is transmitted on the surface of the conductor. From equation (3-5), when the resistivity of the conductor (ρ) is small, the skin depth is thin.

Copper has a relative lower resistivity ($\rho_{copper} = 1.68 \times 10^{-8}$ Ω/m) than other metals, that is why it is often used as the inner and outer conductors of coaxial cable.

The theory of the propagation of an electromagnetic wave in a coaxial cable have deeply been studied and reported in numerous basic text books. Therefore, I am not going to develop it here, I will just develop the main relations we used.

Single mode propagation condition

In the coaxial cable, the dominant mode (the mode with the lowest cutoff frequency) is the TEM mode which has a cutoff frequency of zero. The mode with next lowest cutoff frequency is the TE_{11} mode. The limitation of the single mode regime stops therefore at the cutoff frequency of the TE_{11} mode, which is expressed by the following relation:

$$f_c \approx \frac{1}{\pi(a+b)\sqrt{\mu\varepsilon}}$$

(3-6)

With a and b the diameter of inner conductor and the inside diameter of the shield, respectively (as shown in figure 3.26). The permittivity and the permeability of the insulator are noted ε and μ, respectively. Hence the coaxial cable is single-mode until this frequency, and might in practice be used up to 90% [21] of this frequency.
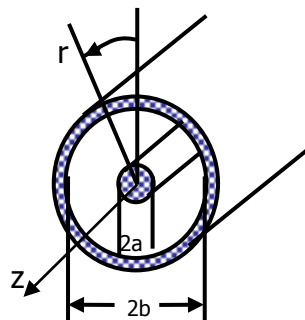

Figure 3.26: scheme of a coaxial cable.

From this equation it is possible to determine the cutoff frequency of a coaxial depending on its topology, i.e. the couple of parameter a and b. This evolution is

plotted in figure 3.27. From this curve, to conceive a coaxial cable operating up to 100 GHz, we need to decrease its size (a+b) down to 500 μm.
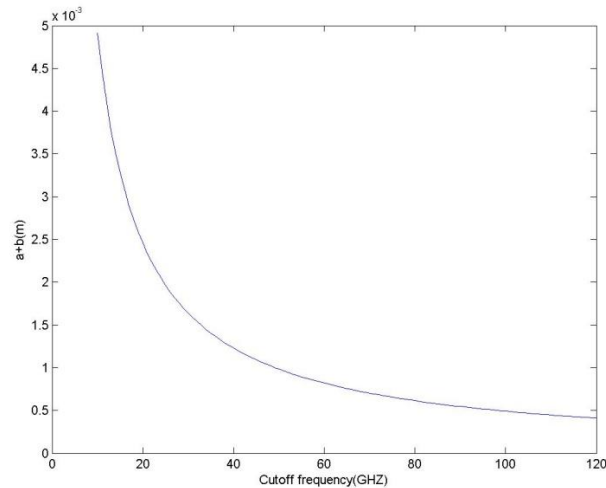
Figure 3.27: Coaxial cable size vs cutoff frequency for single mode propagation

Attenuation coefficient of the propagated wave in a coaxial cable

The attenuation coefficient of the propagated wave is the summation of the losses induced by the conductor and the losses from the dielectric material.

Conductor loss constant:

Most of overall loss of transmission lines is dominated by the metal losses in the region of microwave frequency. Metal losses vary predominantly with the operating frequency. The equation of conductor loss constant is expressed as [1]:

$$\alpha_c = \sqrt{\frac{\omega \varepsilon_r \varepsilon_0}{2\sigma}} \frac{(\frac{1}{a} + \frac{1}{b})}{2\ln\frac{b}{a}} \tag{3-7}$$

Where σ is electric conductivity of the conductor.

Dielectric loss constant

Losses due to the dielectric can be very important in the region of microwave frequencies. This term is proportional to frequency, so at the higher frequency, the

more likely it will dominate overall losses (metal loss is only proportional to the operating frequency). The equation of dielectric loss constant [21]

$$\alpha_d = \frac{\pi\sqrt{\varepsilon_r}}{\lambda} tg\delta \qquad (3\text{-}8)$$

Where $\varepsilon_r = \varepsilon_r^{'} - i\varepsilon_r^{''}$, $tg\delta = \frac{\varepsilon_r^{''}}{\varepsilon_r^{'}}$.

The attenuation coefficient could be minimized since the conductor loss constant depends on the topology (couple a and b) of the coaxial cable. If we consider the parameter b constant, from the equation (3-7), the conductor loss constant is minimized when it derivation over the parameter a is null, as expressed by the development below:

$$\frac{\partial \alpha_c}{\partial a} = 0$$
$$\Rightarrow \ln(b/a) - (1 + b/a) = 0 \qquad (3\text{-}9)$$
$$\Rightarrow b/a = 3.591$$

This development leads to an optimal ratio b/a of 3.591 for minimized conductor losses.

III.2.2 Microsize coaxial cable for extremely high frequency Transmission

Microsize coaxial cable means that the size of coaxial cable is micrometer scale. It can make the frequency of guided wave elevated to tens of GHz, even hundreds of GHz. The higher frequency band of waveguide can transmit more information in unit time. Micrometer size of coaxial cable also makes it easy to integrate to microelectronics devices. In the information times, a lot of electronic products require high transmission speed for high-resolution display and miniaturization (For example LCD panel of mobile phone). The invention of microsize coaxial cable satisfies these requirements.

When electromagnetic wave frequency reaches the visible and near UV region (light frequency: hundreds of THz, even thousands of THz), the plasmonic effect is well established by collective excitation of metal [22]. But in the region of hundreds of GHz, frequency is much lower than plasma frequency of metal (thousands of THz) [23], plasma mode is therefore not formed. So when micrometer size coaxial cable guides electromagnetic waves from tens of GHz to hundreds of GHz, the coaxial cable parameter equations developed above in microwave frequency are still applicable.

The technological process we have developed to fabricate glass fiber with copper wire is therefore very interesting and well adapted to the development of such microsize coaxial cables. More particularly, the very small size achievable with our process allows us to consider the conception and realization of microsize coaxial cable operating in the Extreme High Frequency (EHF) band at 100 GHz, frequency domain where there is not suitable coaxial cable. Indeed, at these frequencies, properties of metal and dielectric materials are degraded limiting the performances of the coaxial cable. In the following study, we will investigate a new topology based on the technology of photonic crystal fiber for reducing the attenuation coefficient of the propagated mode.

In this section we study an original (to the best of our knowledge) coaxial cable design for reducing the attenuation coefficient of the wave propagated in the EHF band or THz one. For reducing the losses induced by the dielectric material, that are dominant at frequencies, we propose to reduce to structure with an arrangement of air-hole the dielectric material in order to decrease the interaction between the electromagnetic field and the dielectric material and consequently to increase the portion of field in air, a low loss medium. To study this proposition, we have tried to optimize the topology of such structure for the operating frequency of 100 GHz. To realize this study, we have used the commercial software COMSOL multiphysics, based on the finite element method. For developing our study, in need to determine the complex permittivity of copper at 100 GHz and then use the complex permittivity of silica at 100 GHz from [24]: $\varepsilon_{SiO_2} = 3.8025 - i1.8 \times 10^{-3}$.

Determination of the copper permittivity at 100 GHz:

The permittivity of metal is well defined by the Drude model [5] with the following relation that depends on the plasma and damping frequencies of the metal:

$$\varepsilon(\omega) = \varepsilon_1(\omega) + i\varepsilon_2 = 1 - \frac{\omega_p^2}{\omega^2 + i\omega\omega_\tau} = 1 - \frac{\omega_p^2}{\omega^2 + \omega_\tau^2} + i\frac{\omega_\tau\omega_p^2}{\omega(\omega^2 + \omega_\tau^2)} \qquad (3\text{-}11)$$

For copper, the plasma and damping frequencies are determined experimentally and reported in the paper [25]:

$$f_p = 1.914\times10^{15} \text{ Hz} \qquad \omega_p = 12.026\times10^{15} \text{ rad/s}$$
$$f_\tau = 8.34\times10^{12} \text{ Hz} \qquad \omega_\tau = 52.401\times10^{12} \text{ rad/s}$$

From these parameters we can calculate the complex permittivity of copper at 100 GHz:

$$\varepsilon_{copper}(100 \text{ GHz}) = -6.618\times10^5 - i\ 1.4525\times10^7$$

In first, we have simulated a conventional structure coaxial cable composed of copper and silica. The topology of the cable is shown in figure 3.29(a), with a two-dimensional intensity map of the fundamental mode. The aim of this first part of the study is to get the optimized parameters of this worst case (silica material).
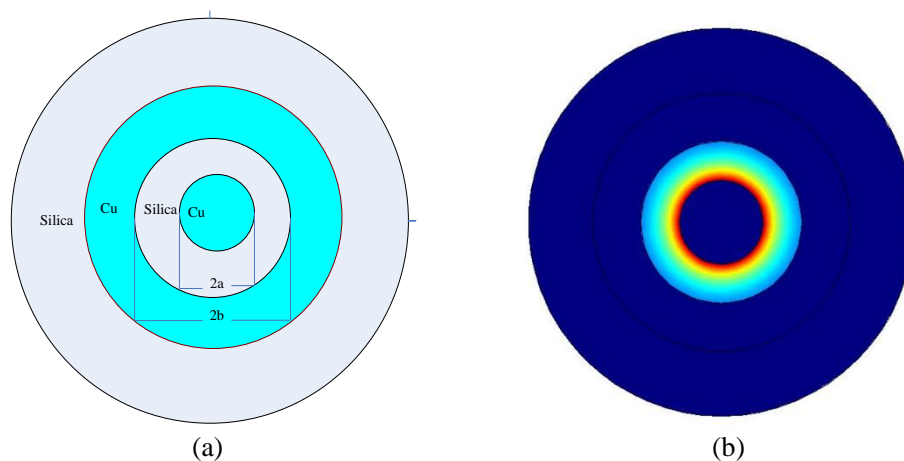

(a)   (b)

Figure 3.28: The structure (a) and fundamental mode field (b) of a conventional coaxial cable composed of silica and copper.

We need to keep the coaxial cable operating in the single mode regime at 100 GHz, leading to previous equation of the cutoff frequency:

$$a+b \leq \frac{1}{f_c \pi \sqrt{\mu \varepsilon}} = \frac{C}{f_c \pi \sqrt{\mu_{SiO_2} \varepsilon_{SiO_2}}} = \frac{3 \times 10^8}{10^{11} \times \sqrt{3.8025\pi}} = 489 \mu m,$$
$$2(a+b) \leq 978 \mu m.$$

In this calculation, 2a = inner copper layer diameter, 2b = inner silica layer diameter. In terms of the above calculation's results, we set outer conductor (copper) diameter = 980 µm, outer insulator silica layer diameter = 1000 µm.

Loss simulation is done for different value of 2a and 2b compounding (the values of 2a and 2b in every compounding satisfy the single mode transmission condition: equation). Our simulation results are shown in figure 3.29. For each calculated couple (2a,2b), the attenuation value is indicated by a color depending on a color scale spanning from -10 dB/m to -100 dB/m. Deeper red color means lower attenuation, while deeper blue means higher attenuation. It is important to notice that the attenuation values equal to -100 dB/m correspond to couple (2a,2b) outside the single mode regime, this value have not been calculated. These values have been set only for being able to plot this graph.

From the figure 3.29, we can get the optimal structure parameters for the lowest attenuation:

The diameter 2b of inner silica layer =700 µm, **b = 350 µm**
The diameter 2a of inner copper=250 µm, **a = 125 µm**
The minimum attenuation is **9.58 dB/m**

Figure 3.29: Attenuation coefficient of the fundamental mode of a coaxial cable (silica-copper) versus its structure parameter

Secondly, we study now the ideal case, air is used as dielectric material. Since, air is considered as free of losses, we study here the lowest attenuation achievable by a conventional coaxial structure composed of copper and air.
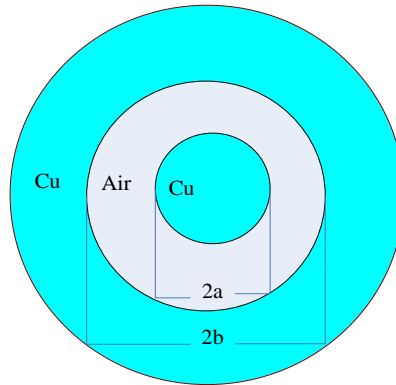
Figure 3.30: Coaxial cable structure graph when air is as the insulator layer

As previously, we calculate the overall size of the cable limiting the single mode regime at 100 GHz. From the equation of the cutoff frequency, we get:

$$a+b \leq \frac{1}{f_c \pi \sqrt{\mu \varepsilon}} = \frac{C}{f_c \pi \sqrt{\mu_{air} \varepsilon_{air}}} = \frac{3 \times 10^8}{10^{11} \times \sqrt{1}\pi} = 955 \mu m,$$

$$2(a+b) \leq 1910 \mu m.$$

As the previous study, we compute different couple (2a, 2b) to get a 2D map of the attenuation coefficient. These results are plotted in figure 3.31. Here, the color scale spans from 0 to -10 dB/m. The values with attenuation equal to -10 dB/m have not been calculated, but added only for plotting the graph.
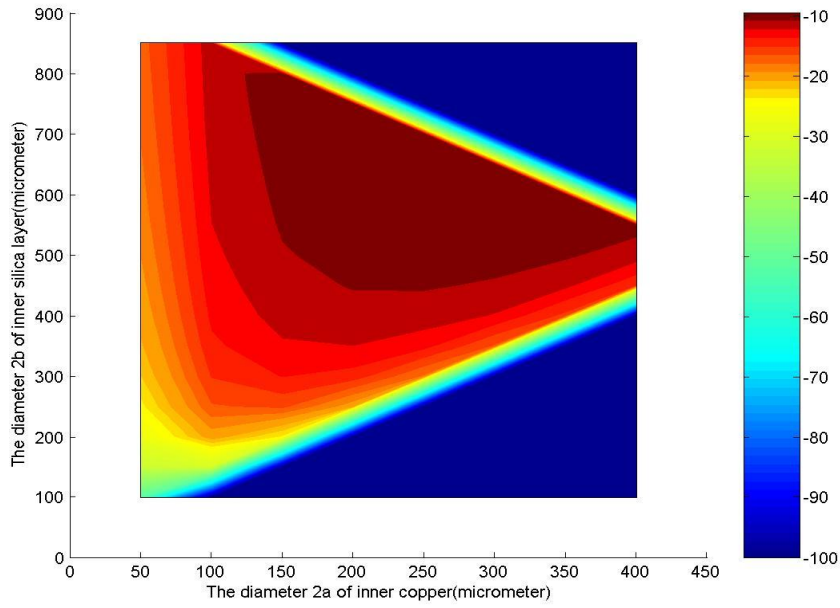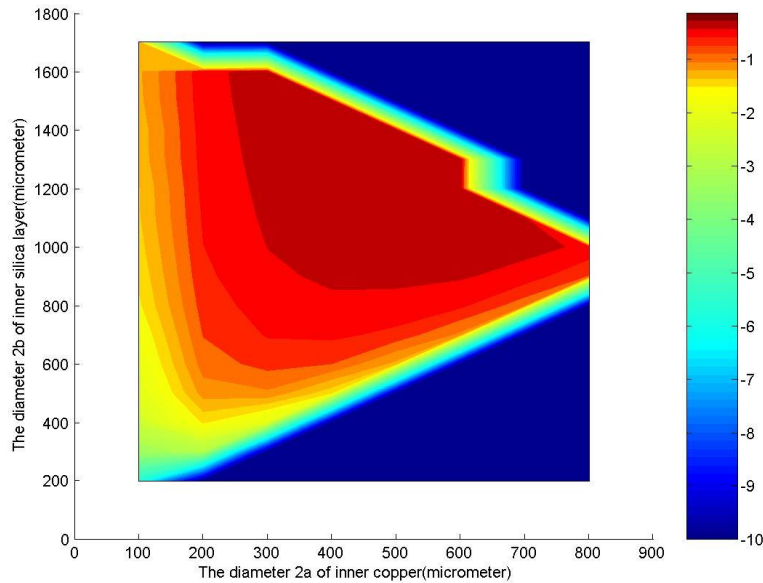

Figure 3.31: Attenuation coefficient of the fundamental mode of a coaxial cable (air-copper) versus its structure parameter

From these results, we can get the optimal structure parameter for the lowest attenuation (the deepest red point):

The diameter 2b of inner air layer =1300 µm, **b = 650 µm.**

The diameter 2a of inner copper=600 µm, **a = 300 µm**.

The minimum attenuation is around **0.14 dB/m**.

By simulation result, it is also seen that air layer can effectively reduce the attenuation of coaxial cable, but if we completely make air as insulator layer, this structure of coaxial cable is not able to be supported by itself. So we plan to design one air and silica hybrid structure for getting relative low loss coaxial cable and at the same time make that the structure can be supported by itself.

The results obtained in this first and second study give us the higher and lower attenuation limits, respectively. The lowest attenuation we can get depending on the ratio of interaction between the electromagnetic field and the silica, in the hybrid coaxial structure we are going to study.

The structure we propose is based on the photonic crystal fiber technology. It consists in realizing an arrangement of air-hole in the dielectric inner layer. Nevertheless, the proposed designs have been conceived in order to keep the study realistic and compatible with the fabrication process of photonic crystal fiber. An example of such topology is shown in figure 3.32. The silica layer around the air-hole should be removed in an idealistic case, but it is important for the fabrication process since it maintain the glass capillaries during the drawing.
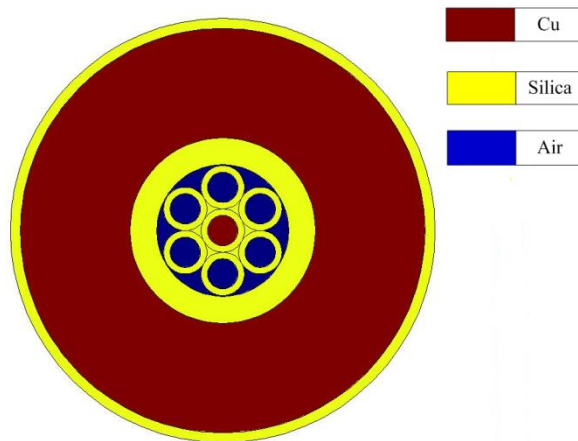
Figure 3.32: The designed air and silica hybrid structure coax cable. Red, yellow and blue region represent copper, silica and air region respectively.

We have simulated and calculated the attenuation coefficient of this kind structure of coaxial cable in the case of different number of air-holes in one ring. During the fabrication process, the ring of air-holes will be realized by stacking a ring of silica capillaries that are in contact each others. Therefore, the thickness of this layer will depend on the number of air-holes (capillaries). For a given number of capillaries and diameter 2a, a geometrical analyze gives only one solution of the

diameter (2b) of the capillaries, that could be normalized by the ratio a/b. We have therefore calculated the ratio a/b for each number of capillaries used for the inner layer. For each number of air-holes, we have kept the ratio a/b constant, changed the diameter 2a and by consequence 2b also. Here are listed the ratio a/b depending on the number of capillaries and the limit of single mode regime:

Air-hole number = 3, a/b = 1/28.42, single mode regime 2a < 70 μm.

Air-hole number = 4, a/b = 1/11.89, single mode regime 2a < 100 μm.

Air-hole number = 5, a/b = 1/7.86, single mode regime 2a < 150 μm.

Air-hole number = 6, a/b = 1/6.12, single mode regime 2a < 200 μm.

Air-hole number = 7, a/b = 1/5.16, single mode regime 2a < 200 μm.

Air-hole number = 8, a/b = 1/4.57, single mode regime 2a < 230 μm.

We have then simulated each topology versus the diameter 2a ranging from 50 μm to 200 μm. The attenuation coefficient of the fundamental mode is presented in figure 3.33. It is important to keep in mind the single mode regime limit for each topology. From this study,

From the figure 3.33, we can get the optimized structure parameters for attenuation:

Airhole number in one ring: 6 airholes

The diameter 2b of inner silica layer = **918 μm**,

The diameter 2a of inner copper layer =**150 μm**.

The minimum attenuation is about **5.45 dB/m**.

The result is about half of that of the optimized coaxial cable composed of copper and silica without airholes.
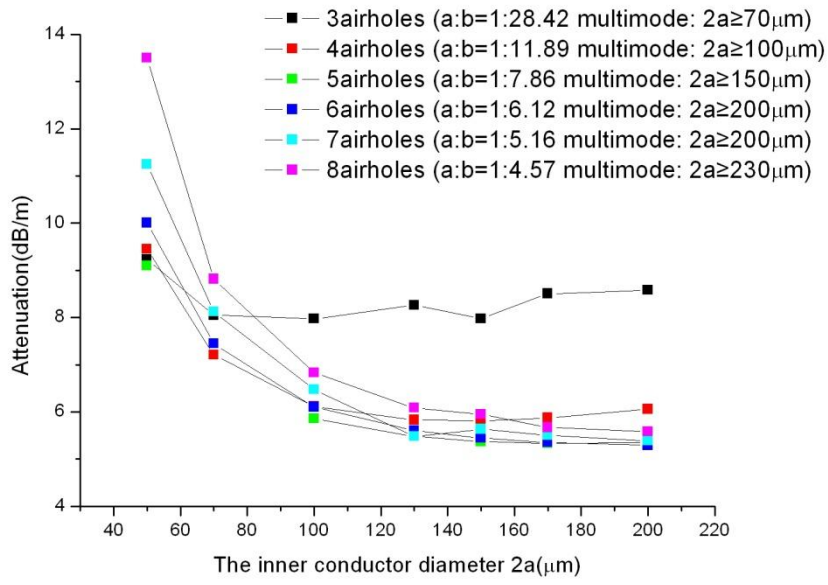
Figure 3.33: Attenuation simulation results of the designed air and silica hybrid structure coax cable

III.2.3 Fabrication of the designed air and silica hybrid structure coaxial cable

The first coaxial preform has been made in our lab, in respect with the following design:
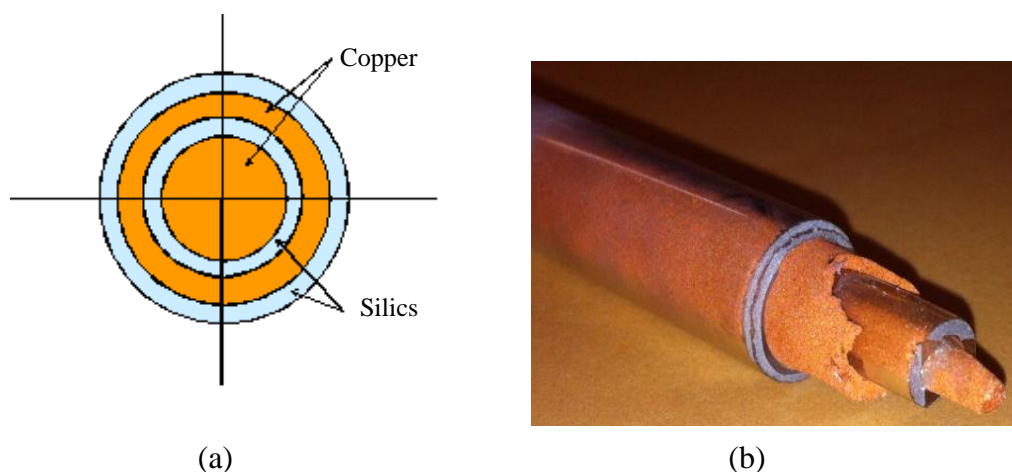
Figure 3.34: Design (a) and realisation (b) of a coaxial preform

The set-up consists to fill the gap between two concentric tubes, like shown in figure 3.34. The main difficulty of this set-up is to ensure the centring of the two tubes together. After a solidification stage (using the resistive furnace of the drawing tower), we obtain the preform shown in figure 3.34(b).

This sample has been realized using regular and fine grains copper powder with two pure silica tubes (whose dimensions were 4/6 and 9/11 mm). Once again, the heat treatment has been done with the resistive furnace at 1130 $^{\circ}$C with a feed of 10 mm/min. The sample presented has a length of 34.5 cm.

Respecting the realization of the improved structure of our designed coaxial cable, together with stack-and-draw method, another alternative way of fabrication could be the following (such solution's another interest is to adapt the thickness of the surrounding silica layer with design, easier than using tubes – thickness of tubes is

limited by the supplier offer):

(1)   Firstly, we fabricate one copper core silica glass tube (it is similar with figure 3.22). After drawing preform to fiber, the copper core rod part of this copper core silica glass tube will become inner conductor of our designed coaxial cable. We fill copper powder into one silica glass tube, then put the silica glass tube to high temperature furnace for melting copper powder to form copper rod. When selecting the size of silica glass tube, we need to consider the region accumulation effect during melting copper powder in glass tube (It has been analyzed in chapter 3). By the critical inner diameter calculation of tube for region accumulation effect in chapter 3, the critical inner diameter of tube is about 2.84-3.22 mm. So the minimum inner diameter of selected tube should be beyond 3.22 mm.

(2)   Then we stack this copper core glass tube and other six hollow core silica glass tubes in one large silica glass tube. After the stacked preform is drawn to fiber, the six hollow core silica glass tubes will be as air holes in the inner insulator layer of our designed microsize coaxial cable).

(3)   Next, we draw the stacked preform to fiber.

(4)   Finally, we will deposit copper layer (by deposition method) to outer surface of cladding of the drawn fiber (we can remove coating in the outside of fiber cladding by applying removing coating liquid) as outer conductor layer of coaxial cable.

In the future, we will realize this fabrication by this method.

III.3. Conclusion

In this chapter, we first analyzed theoretically the preform fabrication (by powder-in-tube method) of metal fiber, together with experiment results, Region accumulation effect of copper may occur during melting copper powder. To avoid the accumulation effect (because this effect will make the copper rod become separate some pieces), we calculated the critical inner diameter of glass tube used. Through analyzing drawing

process of metal fiber, we proposed two improved drawing methods to get better quality and longer continuous copper fiber. Then, we showed our experiment progress for fabricating continuous copper rod in glass tube by powder-in-tube method and also some metal fiber drawn. In these experiments, we designed and realized two original structures:

-(1)A coaxial preform
-(2)A PCF including copper wires

In the last part, we plan to apply the fabrication method of our metal fiber to fabricate the microsize coaxial cable. We design one improved structure microsize coaxial cable through inducing one ring of airholes to reduce its attenuation (to half). And in the future, we will fabricate this microsize coaxial cable with improved structure through combining our above fabrication method of metal fiber and stack-and-draw method.

A new setup for melting powder is now available at Xlim, should be very useful to produce very high quality preform including copper rod. By this way and with the background of the fibre drawing of such fibres, we will produce some tenths of meters fiber with metal inside. More applications become possible: Electrical poling in optical fiber, with a distributed repartition for some meters length; another interesting research field where these structures could be smart is Sensor Domain.

Reference:

[1] G. F.Taylor, "A method of drawing metallic filaments and a discussion of their properties and uses", Physics Review, 1924, Vol.23, p655-p660.

[2] I. W. Donald, Review, "Production, properties and applications of microwire and related products", Journal of Material Science, 1987, Vol.22, p2661- p2679.

[3] I. W. Donald and B. L. Metcalfe, "The preparation, properties and applications of some glass-coated metal filaments prepared by the Taylor-wire process", Journal of Material Science, 1996, Vol.31, p1139-p1149.

[4] M. Fokine, L.E.Nilsson et.al. "Integrated fiber Mach－Zehnder Interferometer for electro-optic switching", Optics Letters, 2002, Vol. 27, No.18, p1643-p1645.

[5] B. H. Kim, S. Moon, U. C. Paek, and W.-T. Han, "All fiber polarimetric modulation using an electro-optic fiber with internal Pb-Sn electrodes", Optics Express, 2006, Vol.14, No.23, p11234 - p1124.

[6] Zhangwei Yu, W. Margulis, O. Tarasenko, H. Knape, and P.-Y. Fonjallaz, "Nanosecond switching of fiber Bragg gratings", Optics Express, 2007, Vol.15, No.22, p14948-p14953.

[7] B. H. Kim, S. H. Lee, A. Lin, C.-L. Lee, J. Lee, and W.-T. Han, "Large temperature sensitivity of Sagnac loop interferometer based on the birefringent holey fiber filled with metal indium", Optics Express, 2009, Vol.17, No.12, p1789-p1794.

[8] M. A. Schmidt, L. N. Prill Sempere, H. K. Tyagi, C. G. Poulton, and P. S. J. Russell, "Waveguiding and plasmon resonances in two dimensional photonic lattices of gold and silver nanowires", Physics Review B, 2008, Vol.77, p033417.

[9] H. W. Lee, M. A. Schmidt, H. K. Tyagi, L. P. Sempere, and P. S. J. Russell, "Polarization-dependent coupling to plasmon modes on submicron gold wire in photonic crystal fiber", Applied Physics Letter, 2008, Vol.93, p111102.

[10] H. W. Lee, M. A. Schmidt, R. F. Russell, N. Y. Joly, H. K. Tyagi, P. Uebel, and P. St. J. Russell, "Pressure-assisted melt-filling and optical characterization of Au nano-wires in microstructured fibers", Optics Express, 2011, Vol.19, No.13, p12180-p12189.

[11] Tomoko Goto, Masamitsu Nagano and Keizo Tanaka, "Tensile Strength of copper and iron filaments produced by the method of glass-coated melt spinning", Transaction of Japan Institute of Metals, 1977, Vol.18, p209-p213.

[12] J. Hou, D. Bird, A. George, S. Maier, B. T. Kuhlmey, and J. C.Knight, "Metallic mode confinement in microstructured fibres", Optics Express, 2008, Vol.16, No.9, p5983-p5990.

[13] H. K. Tyagi, H. W. Lee, M. A. Schmidt, P. Uebel, N. Joly, M. Scharrer, and P. S. J. Russell, "Plasmon resonances on gold nanowires directly drawn in a step-index fiber", Optics Letters, 2010, Vol.35, No.15, p2573-p2575.

[14] Kaustubh S. Gadre and T. L. Alford, "Contact angle measurements for adhesion energy evaluation of silver and copper films on parylene- nand SiO_2 substrates", Journal of Applied Physics, 2003, Vol.93, No.2, p919-p923.

[15] Sharfrin, E.; Zisman, William A, "Constitutive relations in the wetting of low energy surfaces and the theory of the retraction method of preparing monolayers", The Journal of Physical Chemistry, 1960, Vol.64, No.5, p519–p524.

[16] Takaimchi lida and Roderick I.L Cuthrie, "The physical properties of liquid metals", Oxford University Press Inc, New York, 1988.

[17] Sun yong. Master thesis (2007) in Beijing university of Technology (in Chinese).

[18] T. ohnaka, T. fukusako, T. ohmichi, T. MASUMOTO, A. inouei and M. hagiwara, in Proceedings of 4th International Conference on Rapidly Quenched Metals, edited by T. Masumoto and K. Suzuki (Japan Institute of Metals, Sendai, 1982) p.31.

[19] Leonid N. Butvina, E. M. Dianov, N. V. Lichkova,V. N. Zavgorodnev, L. Kuepper, "Crystalline silver halide fibers with optical losses lower than 50 dB/km in broad IR region and their applications", Proceedings of SPIE, 2000,Vol. 4083, p238-p253.

[20]Akira Yoshikawa, Boris M.Epelbaum, Tsuguo Fukuda, Kenji Suzuki, Yoshiharu Waku, "Growth of Al_2O_3/$Y_3Al_5O_{12}$ Eutectic fiber by Micro-pulling-Down Method and Its High-Temperature strength and Thermal stability" Japanese Journal of Applied Physics. Vol.38, 1999, p5-p58.

[21] Kizer, George Maurice, "Microwave communication", Iowa State University Pressure, 1990, p312.

[22] J. B. pendry, A. Jholden et.al. " Extremely Low Frequency Plasmons in Metallic Microstructures", Physics Review Letter, 1996, Vol.76, No.25, p4773-p4776.

[23] C.G. Poulton, M.A Schmidt et.al. "Numerical study of guided modes in arrays of metallic nanowires", Optics Letter, 2007, Vol.32, No.12, p1647-p1649.

[24] D. Grischkowsky, S. Keiding, M. V. Exter, and C. Fattinger, "Far-infrared time-domain spectroscopy with terahertz beams of dielectrics and semiconductors," Journal of the Optical Society of America B, 1990, Vol. 7, No. 10, p2006-p2015.

[25] M. A. Ordal, Robert J. Bell, R. W. Alexander, Jr, L. L. Long, and M. R. Querry, "Optical properties of fourteen metals in the infrared and far infrared: Al, Co, Cu, Au, Fe, Pb, Mo, Ni, Pd, Pt, Ag, Ti, V, and W", Applied optics, 1985, Vol. 24, No. 24, p4493-p4499.

[26]http://www.totoku.com/products/electric_wires/wires/coaxial/microwave.shtml

[27] 3rd International Conference on Infrared, Millimeter and Terahertz Waves, 2008, p1.

[28]T.Jeon, D.grischkowsky, "Direct optoelectronic generation and detection of sub-ps-electrical pulses on sub-mm-coaxial transmission lines", Applied Physics Letters, 2004, Vol.85, p6092-p6094.

[29] Philip St. J. Russell, "Photonic-Crystal Fibers", Journal of light wave technology, 2006, Vol. 24, No. 12, p4729-p4749.

General conclusion

In this thesis, we hope to fabricate some kinds of multimaterials special optical fibers. The core and cladding of these fibers are made of the different kinds of materials. When the core of these optical fibers are made of soft glass materials (typically Tellurite and Chalcogenide) or highly doped heavy metal oxide silica glass materials, these optical fibers (silica glass is as cladding material) will have high refractive index difference (due to the indexes of these special materials are higher than that of pure silica glass.) and high nonlinear coefficient. When these materials are metal, metal and silica glass (or other kinds of glasses), they can compose optical and electronical hybrid devices. We can also make silica glass as the insulator layer of electronical device to fabricate microsize electronical devices through drawing optical fiber method.

In chapter 1 of this thesis, we first introduce all kinds of fabrication methods of doped fiber and compare the advantages and drawbacks of these fabrication methods; Finally we decide to select powder-in-tube method, to fabricate our multimaterials special optical fibers, for its potential of convenience and least contamination.

In chapter 2, we explore the applications of our fabricated highly doped heavy metal oxide silica glass fiber. Since highly doped heavy metal oxide silica glass fiber has the high refractive index difference and relative low attenuation, we explore the high refractive index difference all-solid core ARROW (antiresonant reflection optical waveguide) bandgap fiber based on highly doped heavy metal oxide silica glass fiber (The high index core of highly doped heavy metal oxide silica glass fiber is as high index rod of ARROW bandgap fiber). We theoretically analyze the properties (relative to the low refractive index difference all-solid core ARROW bandgap fiber) of high refractive index difference($\geq$0.1) all-solid core ARROW bandgap fiber.

We find that when the center position of the first bandgap is fixed to 1064nm, and ratio d/pitch is fixed 0.9/7, comparing with low index difference solid core ARROW bandgap fiber, the higher index difference solid core ARROW bandgap fiber has: (1) bandgap width and frequency width are invariable. (2) the larger index difference between the first order mode (Two degenerate HE_{11} modes) and the second order mode (TE_{01}, TM_{01} and Two degenerate HE_{21} modes), namely to be easier to keep single mode transmission since large index difference makes fundamental mode power difficult to couple to high order mode. (3) Smaller effective fundamental mode area (and this also means that the higher index contrast all-solid core ARROW fiber has higher nonlinear coefficient). (4) The higher confinement loss. (5) The smaller critical bend radius (this means that higher index contrast all-solid core ARROW fiber has lower sensitivity of fiber's bend loss). Among these properties, the larger index difference between the fundamental mode and high order mode, and lower sensitivity of fiber's bend loss are favorable for high power laser single mode transmission.

In experiments, we fabricated one kind of highly doped heavy metal oxide silica glass fiber (we call it SAL fiber: 70mol%SiO_2, 20mol%Al_2O_3, and 10mol% La_2O_3).This kind of SAL fiber's index difference can reach 0.1; and we have realized that its attenuation loss can be lowered up to 1 dB/m (the PhD thesis work of L.Stephanie in our lab). Farther, we designed and fabricated one low loss solid core Arrow bandgap fiber based on SAL fiber (SAL material is the material of high index rod in such solid core Arrow bandgap fiber). By the structure design of Arrow bandgap fiber, the center position of its first bandgap is fixed at 1064 nm. And we also theoretically calculated the critical bend radius (for bend loss) curve and the dispersion curve of fundamental mode of such Arrow bandgap fiber. Finally, we fabricated the preform of such solid core bandgap fiber through inserting SAL core fiber without coating into the cane of one photonic crystal fiber fabricated by stack-and-draw method, and drew it to solid core bandgap fiber.

In chapter 3, we extend the powder-in-tube fabrication method to the fabrication of metal fiber. We first analyze theoretically the preform fabrication (by powder in tube method) of copper fiber, also together with experiment results. Region accumulation effect of copper powder may occur during melting copper powder. To avoid the region accumulation effect (because this effect will make the copper rod become separate some pieces), we calculate to get the critical inner diameter of glass tube used.

About the drawing of metal fiber, because metal is crystal, and its viscosity changes suddenly during from solid to liquid, so its drawing theory is different from glass fiber (glass is noncrystal, its viscosity changes gradually during from solid to liquid). Through analyzing drawing process of metal fiber, we propose the two improved drawing method (adding pressure method and slow speed drawing method) to get better quality and longer continuous copper fiber(In fact, these two methods can also be applied to draw other kinds of mutimaterial special optical fibers which includes the mixture of crystal and glass). Then, we show our experiment progress for fabricating continuous copper rod in glass tube by powder-in-tube method and also some metal fiber drawn. Together with stack-and-draw method, we also realize one photonic crystal fiber with copper wires.

Finally, we hope that the fabrication technology of our metal fiber can be applied to the fabrication of microsize electronic device. In this thesis, we fabricate the microsize coaxial cable. The coaxial cable is good waveguide to guide microwave signal, in the case of microize coax cable, the frequency of guided signal can be elevated to tens of GHz, even hundreds of GHz. We designed one improved structure (adding one ring airholes in the inner insulator layer) coaxial cable to reduce its attenuation. The simulation results indicate that the attenuation can be reduced to the half of convention structure coaxial cable without adding airholes. Finally, together with stack-and-draw method, we will fabricate the improved structure microsize coaxial cable through drawing the metal fiber.

In the future, we can explore more kinds of mutimaterial special optical fiber. For example: extending the used material to semiconductor to fabricate microsize semiconductor devices. And we also can continue to explore more applications of these mutimaterial special optical fibers, for example, metal optical fiber for sensing applications, and multimaterial glass for infrared transmission.

Now, the development of the region of mutimaterial special optical fiber is initial stage. In future, this region will obtain large and rapid progress. More mutil-function multimaterial special optical fibers will be explored to improve the life of people!